System analysis of a 1 liter thermochemical heat battery for seasonal heat storage

Zwiep, E.J.G.

Award date:
2021

Technische Universiteit Eindhoven University of Technology

Department of Mechanical Engineering
Energy Technology Research Group

Master Thesis

System analysis of a 1 liter thermochemical heat battery for seasonal heat storage

Emiel Zwiep
Sustainable Energy Technology
Eindhoven University of Technology

Project coordinators:
dr. ir. A.J.H Frijns
ir. M.A.J.M Beving

Graduation Committee:
dr.ir. C.M. Rindt
dr.ir. A.J.H. Frijns
dr.ir. L. Pel

Eindhoven, February 1, 2021

Declaration concerning the TU/e Code of Scientific Conduct for the Master's thesis

I have read the TU/e Code of Scientific Conduct[i].

I hereby declare that my Master's thesis has been carried out in accordance with the rules of the TU/e Code of Scientific Conduct

Date 1/29/20

Name E.J.G. Zwiep

ID-number 0851408

Signature 

Insert this document in your Master Thesis report (2nd page) and submit it on Sharepoint

[i] See: http://www.tue.nl/en/university/about-the-university/integrity/scientific-integrity/
The Netherlands Code of Conduct for Academic Practice of the VSNU can be found here also.
More information about scientific integrity is published on the websites of TU/e and VSNU

Abstract

In order to reduce greenhouse gasses, more and more sustainable energy sources emerge. Sustainable energy sources have a discrepancy between energy supply and demand. This works on a daily basis (the sun does not shine at night), but also on a seasonal basis as solar radiation is higher in the summer. One method to bridge the gap between seasonal supply and demand is via usage of thermochemical materials (TCMs). TCMs work via a sorption process or chemical reaction and have some of the highest energy densities compared to sensible or latent heat storage.

The aim of this thesis was to find the performance of different TCMs using a single packed bed reactor. This is done by varying inlet conditions like humidity and mass flow. A 1 liter reactor setup for testing thermochemical materials is extensively used. Two different TCMs have been tested using this setup: Zeolite 13X and K_2CO_3.

A continuum model of both Zeolite and K_2CO_3 is made in COMSOL multiphysics 5.5. The kinetics of water adsorption by Zeolite have been modelled using the LDF-model. The model is validated against experiments. This model is used to find the influence of inlet temperature for 20 to 40 °C on the hydration time and storage capacity. The maximum amount of energy and total hydration time go down when the temperature goes up.

Experiments with Zeolite 13XBF (average particle size of 3 mm) are conducted to find the influence of the air flow and the inlet humidity on the temperature increase. It was found that an increase in air flow from 31 g/min up to 97 g/min (with equal humidity) causes the system to reach a threshold of 10 °C 8 times faster. The humidity seems to correlate directly to the temperature output for Zeolite. A maximum power output of 23 W is found in experiments using an air flow of 100 g/min and a water flow of 25 g/h. No clear correlation between inlet conditions and total energy extraction is found.

A total of nine cyclic experiments have been conducted for K_2CO_3 (average particle size before first experiment 1.2 mm) to improve the reaction rate. This has been done by hydrating for up to 230 hours using an air flow of 100 g/min and a water flow of 25 g/h. It was found that after each subsequent hydration, the reaction rate became a little bit faster, as long as the material hydration reached the amount of absorbed water of the previous cycle. Agglomeration is observed after every cycle, to an extent that individual beads are still recognizable. Before each hydration, the K_2CO_3 is taken out of the reactor. At refilling the reactor with the seperated particles, expansion is seen. After cycle 8, the volumetric expansion of the material is found to be 33%.

This thesis is concluded by comparing the results of power output and weight during hydration between a Zeolite experiment and a K_2CO_3 experiment. Both experiments have been conducted using an air flow of 100 g/min and a water flow of 25 g/h. The Zeolite adsorption process is found to be faster than absorption process of K_2CO_3. The time it takes to have an 8 °C increase in temperature between reactor inlet and outlet is 10 minutes for Zeolite 13X and 13 minutes for K_2CO_3. Using the same inlet conditions of 25 °C, 100 g/min air and 25 g/h water the maximum temperature at the outlet is 38 °C for K_2CO_3 and 41.5 °C for Zeolite 13X.

Contents

Nomenclature

Roman symbols

ΔE	Activation Energy	J/mol
ΔH	Enthalpy change	J/mol
$\dot{m}$	Mass flow rate	kg/s
$\dot{V}$	Volume vlow rate	m^3/s
A	Surface area	m^2
c	Concentration	mol/m^3
C_p	Specific heat at constant pressure	$J/(kg \cdot K)$
D	Inner diameter of reactor	m
D_{ax}	Axial dispersion coefficient	m^2/s
D_r	Radial dispersion coefficient	m^2/s
E	Energy	J
g	Gravitational constant	9.81 m^2/s
Gr	Grashof number	-
h	Convective heat transfer coefficient	$W/(m^2 \cdot K)$
k	Thermal conductivity	$W/(m \cdot K)$
L	Height of reactor	m
M	Molar mass	kg/mol
m	Mass	kg
P	Power	W
p	Pressure	Pa, bar
Pe	Peclet number	-
Pr	Prandtl number	-
q	Water loadin	mol/kg
q_r	Heat flux	W/m^2

R	Universal gas constant	8.314 $J/(kg \cdot K)$
r	Radius	m
T	Temperature	K

Greek symbols

α	Fractional conversion	-
β	Coefficient of thermal expansion	$1/K$
ϵ	porosity	
Λ	Heat dispersion coefficient	$W/(m \cdot K)$
μ	Dynamic viscosity	$Pa \cdot s$
ν	Kinematic viscosity	m^2/s
ρ	Material density	kg/m^3
ζ	Mixing ratio	kg/kg

Abbreviations

AP	Absolute Pressure sensor
CEM	Controlled evaporator mixer
FS	Full scale
GFC	Gas flow controller
HHV	Higher heating value
PV	Photo voltaic
RH	Relative humidity
RP	Relative Pressure sensor
TCM	Thermochemical material
TES	Thermal energy storage
THS	Thermochemical heat storage

subscripts

a	Air
amb	Ambient
b	Packed bed
eq	Equilibrium
ew	Exhaust wrap
h	Convective

i	Inner layer
ins	Insulation
k	Conductive
m	Lowest hydrate
n	Highest hydrate
o	Outer layer
r	Radial direction
sat	Saturation
tef	Teflon
tot	Total
v	Water vapor
w	Wall, water

1 | Introduction

Greenhouse gas emissions need to be reduced as much as possible in the next decades. Therefore green energy sources will become more and more common. Green energy can be produced anywhere, as long as there is a source of energy (solar, wind). As a result, production of energy is transitioning from a centralized to a decentralized system. With a decentralized energy grid, new challenges arise. One of the challenges lies in the intermittent behaviour of green energy, which causes energy supply and demand mismatch.

The energy supply and demand mismatch works on two levels: Daily and seasonal. Generally, energy generation from solar (PV or solar thermal systems) provides energy from the morning until the afternoon, when demand is low. During the early morning and in the evening demand is high, while solar systems do not provide energy. The seasonal mismatch is best seen for solar energy. Solar energy production peaks in the summer and is the lowest in the winter. In the Netherlands, winters are relatively cold and demand for thermal energy is therefore high. In the case of heat supply and demand, especially the seasonal mismatch is large, as can bee seen in Figure 1.1.

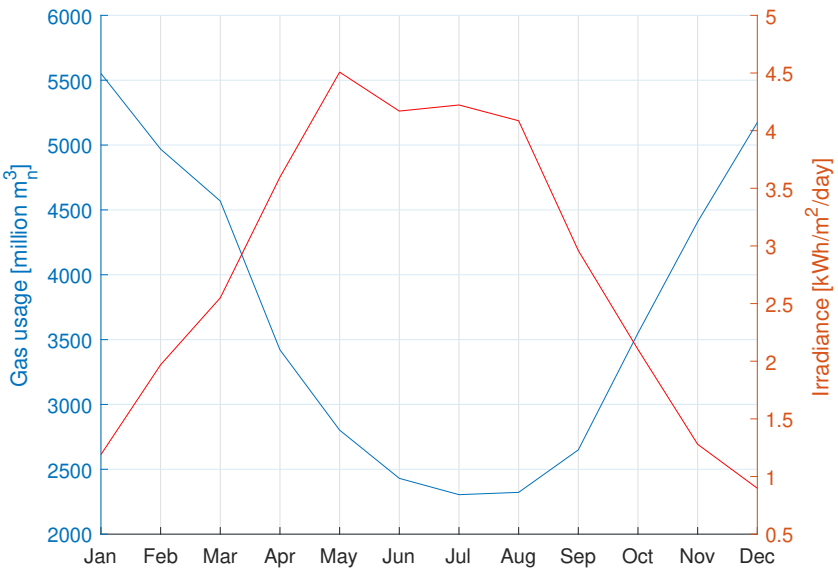

Figure 1.1: Seasonal mismatch between solar irradiance [1] in red and domestic gas usage [2] in blue. Gas usage is shown in million normal cubic meters, which is the standard of measuring gas usage in the Netherlands (normal conditions are 293.15 K and 1.0135 bar).

In order to get a proper comparison on the possible impact solar thermal systems can have, the solar irradiance is multiplied by the area of roofs in the Netherlands that is suitable for solar energy generation (around 872 km^2 according to Deloitte [3]). Using an average of 30.5 days per month, the comparison

looks as seen in Figure 1.2.

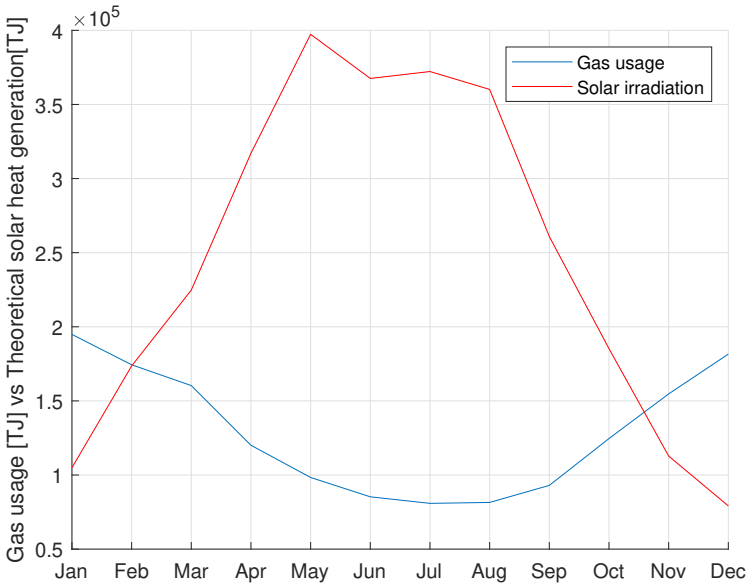

Figure 1.2: Solar irradiation on suitable roofs compared to the total gas usage in the Netherlands per month (Solar effeciency assumed at 90% [4], gas usage converted to energy by using the gross calorific value of Groningen-gas, which is 35.096 MJ/m^3) [5].

Figure 1.2 uses the assumption of 90% efficiency for solar thermal systems [4]. It should be noted that this is relatively high, but it does show the potential that solar generation has. Especially since one of the main contributors to greenhouse gases at this moment is domestic heating. In 2017, around 27% of the total energy usage in Europe came from households [6]. In the Netherlands 46% of the total household energy usage is used for space and water heating [7]. Solar energy production combined with Thermal Energy Storage (TES) can reduce the carbon footprint of housing and TES can reduce the supply and demand mismatch.

1.1 Thermal energy storage

In this section, different kinds of thermal energy storage methods are elaborated. This is done by first mentioning three different types of storage methods, that differ thermodynamically. Two different types of reactor systems are discussed, such as open or closed systems.

1.1.1 Thermodynamic storage principles

Thermal energy storage (TES) can mainly be divided into three different types of storage systems. Sensible heat storage, latent heat storage and thermochemical heat storage (THS). These types of storage are explained in this section.

Sensible heat storage
Sensible heat storage is heat storage in the form of temperature difference (hence, sensible) in a high heat capacity storage material.

$$E = mC_p\Delta T \tag{1.1}$$

Here, E is the total thermal energy stored in [J], m is the mass of the material in [kg], C_p is the specific heat of the storage material in $[\frac{\text{J}}{\text{kg K}}]$ and ΔT is the temperature difference between the initial and final temperature in [K]. This is a method of energy storage that is mostly used for short term heat storage. Due to the temperature difference between the storage material and the surroundings, energy leaks away relatively fast when proper isolation is lacking. The advantage of this technique is that it is relatively easy to implement. Often used material are rock, water and concrete, due to their low cost and high energy capacity [8]. The downsides of this type of storage is that for most materials, the energy density is low and energy leaks to the surroundings.

Latent heat storage

In latent heat storage, the phase change (solid-liquid or liquid-gas) of a material is used to capture the heat. Due to the fact that the energy is stored in the enthalpy difference of the phase change, these systems are mostly useful in a very specific temperature range, namely around the temperature at which the phase change occurs. Examples of phase change materials are paraffines, nitrates and sugar alcohols. Phase change materials are best operated around the temperature where the phase change occurs [9], which results in a very specific operating range. The total amount of thermal energy stored is given by:

$$E = mC_{p,(s)}\Delta T + ma_m\Delta H_m + mC_{p,(l)}\Delta T \tag{1.2}$$

Where the subscripts s and l define the solid or liquid state, a_m [-] is the melt fraction and ΔH_m is the enthalpy of the phase change in [J/kg]. This can also be seen in Figure 1.4.

Thermochemical heat storage

Thermochemical heat storage is a method where heat is stored by dehydrating an adsorbent, or thermochemical material (hereafter called TCM). The energy is released in an exothermic reaction when the adsorptive is adsorbed by the TCM, see Equation 1.4 and Figure 1.3. A big advantage of this type of storage is the fact that after the TCM is charged (dehydrated), the energy is stored as long as it is kept away from the adsorptive. This fact allows TCMs for use in seasonal heat storage. The total amount of heat stored is given by:

$$Q = m_{ads}(q_{sat} - q_0) * \Delta H_{mean} + mC_p\Delta T \tag{1.3}$$

Where m_{ads} is the total mass of adsorbents in [kg], q denotes the water loading of the adsorbent in [kg/kg], with the subscripts sat and 0 denoting the end (or saturated) loading and the begin loading respectively. ΔH_{mean} is the mean adsorption enthalpy in [J/mol]. The temperature range in which desorption takes place is broad for TCMs. As long as the thermal energy is high enough to break the bond between the adsorptive and TCM, desorption will take place.

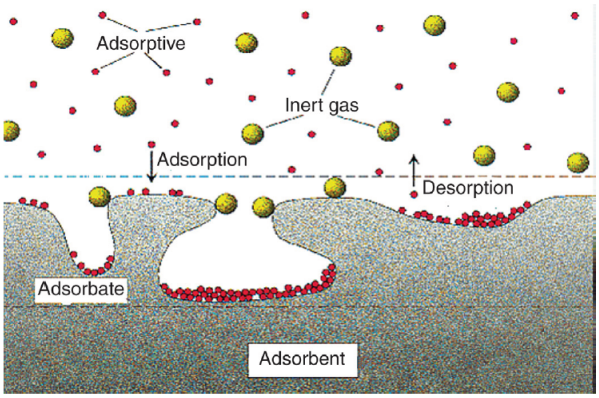

Figure 1.3: Schematic representation of adsorption and desorption [10].

Sorption works as follows: Heat (in the form of dry hot air) is blown through a solid state TCM, which is thereby being 'dried': The TCM releases adsorbed water, which is carried with the air through the outlet of the system. This is the charging step. The heat added to the TCM can stay there indefinitely as long as it does not come in contact with water vapor. This is the storage step. When heat is to be released, moist air is passed through the TCM. This can be done until the TCM is saturated, which would be the equivalent of an 'empty battery'. This is the discharge step. The system can be charged (left to right) and discharged (right to left) according to this principle, which is shown in the following equation:

$$TCM \cdot xH_2O_{(s)} + \text{thermal energy} \longleftrightarrow TCM_{(s)} + xH_2O_{(g)} \tag{1.4}$$

Where x represents amount of moles of water that is adsorbed or absorbed. The amount of water vapor adsorbed or absorbed depends on the type of material, while the type of sorption also depends on the material. Figure 1.3 shows a schematic representation of the adsorption process. However, not all TCMs work using an adsorption process. For example salt hydrates work via a chemical reaction (an absorption process). In an absorption process the absorptive permeates the absorbent, while in an adsorption process the adsorptive assimilates at the surface of the adsorbent (as seen in Figure 1.3). In this thesis, two TCMs are used, the first being Zeolite 13XBF, which is an adsorbent. The second TCM is potassium carbonate (K_2CO_3), which is an absorbent. Absorbents like salts are sensitive for deliquescence, causing a the material to dissolve in water. In order to be sure the water vapor concentration at the inlet is stable, the system stability is tested using Zeolite 13X, since that material is inert.

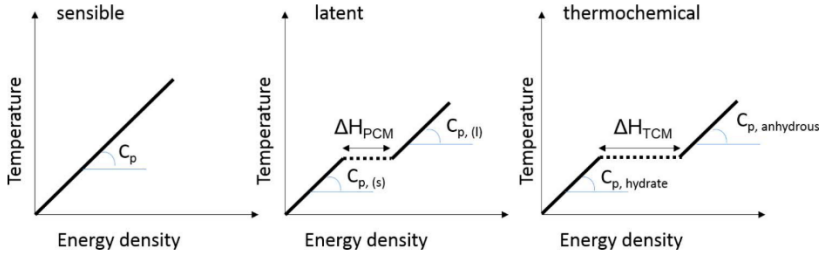

Figure 1.4: Schematic overview of the difference between energy density of sensible, latent and thermochemical heat storage vs temperature. [11].

Figure 1.4 shows the three main thermodynamic distinctions of heat storage in a schematic way. In conclusion, sensible heat storage is based on storing the heat in the form of a temperature difference in a (high) heat capacity material. Latent heat storage adds the phase change, which allows for storage in a smaller temperature range. Thermochemical heat storage, based on adsorption or absorption of a gas allows for the highest heat storage capacity. Of all these systems THS shows the most potential for seasonal storage, as it has a large operating range and a high energy densities compared to other types of TES [12].

1.1.2 Open vs closed systems

Besides the three different thermodynamic storage principles, a distinction can be made between open and closed systems. Michel et al. (2014) compared both systems using a reactor with a packed bed consisting of a salt hydrate: "In a closed thermochemical system, the salt reacts with pure water vapor at vacuum pressure, while in an open system, the reactive solid bed is crossed by a moist air flow at atmospheric pressure" [13]. Vacuum pressure is in this case around 1000 Pa. As a closed system only exchanges heat or cold, it needs an evaporator/condensor and a water storage resevoir (to store the water after charging). An open system uses air from either the surroundings or a compressor. This allows for a design that is simpler to operate than a closed system, as it does not need a condensor and water

storage resevoir. Abedin et al.(2012) performed an energy and exergy analysis on both an open and closed system In this research open systems had a cyclic energy and exergy efficiency of 69% and 23% respecively, compared to 50% and 9% for closed systems [14]. Given that an open system uses both a simpler design, as well as a slightly better energy and exergy performance, this thesis focuses on an open THS system.

1.2 Scope and Methodology

In the introduction, the current or future need for household thermal storage systems has been mentioned. As shown in the previous section, the best possible way to find an implementation for this goal is by looking at THS. This type of storage is versatile, thanks to the large range of temperatures that can be used for charging, as well as the high storage capacity. This makes such a system perfect for household use.

Research on the usability of different storage materials has already shown that there are several criteria that have to be met. Yu et al. (2013) selected the materials based on [15]:

1. High energy storage density
2. High uptake of sorbate
3. Heat and mass transfer properties that allow for reaching a certain design power
4. Non poisonous
5. Low cost
6. Thermal stability

One of the materials that meets most of the criteria is Zeolite 13XBF. This material has a relatively high energy storage density, as well as high uptake of water. As it is a porous material, it also has heat and mass transfer properties that allow for a controlled outlet power. Lastly, it is non poisonous and has a high thermal stability at low (below 200 °C) temperatures [16]. Several researchers have conducted research on Zeolite 13X on reactor scale [13, 17–19]. However, Zeolite 13X is a relatively costly material. Salt hydrates are another type of TCM that is interesting, as it is generally cheap. In the research of Donkers et al. (2017), an extensive review of 563 hydrate reactions are listed in a database . Twenty five salt hydrates are shortlisted according to several filters. They mention potassium carbonate as a promising candidate for heat storage, as it has a high energy density on material level (1.3 GJ/m^3), a possible hydration temperature above 50 °C, a minimum dehydration temperature below 120 °C and a melting point that is higher than the dehydration temperature [20].

Due to the relatively high cost of Zeolite 13X, it is interesting to look at other materials. In order to test sorption materials on reactor scale, a 1 liter reactor setup has been built. Different TCMs can be tested in this reactor to find the influence of several material parameters, like the grain size and enthalpy of reaction. This thesis will also go in depth on finding characteristics like the temperature increase that can be delivered using different inlet conditions and two different TCMs, Zeolite 13X and potassium carbonate.

The 1 liter prototype heat storage reactor system is extensively tested using Zeolite 13x as TCM. Zeolite is well-described in literature. In order to see the influence of different inlet conditions on temperature increase and mass transfer, multiple hydration experiments are conducted, using different air and water flow rates. The dependence between the power output and flow, power output and humidity are both investigated by means of experiments. Furthermore it is tested if the water vapor concentration within the setup is stable and accurate. Zeolite is a good testing candidate because it cannot go into deliquescence

at high water vapor concentrations. Should the water vapor concentration unexpectedly reach too high values, the Zeolite would remain intact. The results of these experiments are used to determine the power output and temperature increase of the system . Once the setup is properly characterized with zeolite and the applied water vapor concentrations turn out to be stable, the material is replaced with K2CO3. Comparable cyclic experiments are conducted while using potassium carbonate as TCM. The results of these experiments are compared to the results of Zeolite 13X.

A continuum model of the reactor is created in COMSOL multiphysics. Heat and mass transfer is modelled and validated with experiments. After validation the model is used to find the influence on temperature increase of different parameters, like the inlet temperature and the flow rate. Next, the numerical model is updated for potassium carbonate. The numerical model of potassium carbonate is compared to reactor experiments that are conducted using potassium carbonate.

The research question is defined as:
How does a 1 liter reactor filled with Zeolite or K_2CO_3 perform under different conditions during multi-cyclic charge and discharge experiments, and how can this be characterized?

This research question is subdivided into other research questions:

- What is the influence of the flow rate on the reactor performance? Which flow rate gives maximum power?
- What is the influence of the moist air inlet temperature on hydration performance? Does it influence hydration time, outlet temperature and efficiency?
- Combining these questions: Can an ideal set of inlet conditions be found (inlet humidity and temperature) for giving maximum power? Does this set of conditions also provide the highest temperature increase?
- How does potassium carbonate perform compared to Zeolite 13X in terms of output power, temperature increase and total energy stored?

1.3 Thesis outline

The thesis is divided into 7 main chapters. In Chapter 2, the experimental setup is described. In this chapter, the experiments that are conducted are explained, along with some theoretical background. In Chapter 3, the numerical model that is built in Comsol for Zeolite 13X is explained, along with the theoretical background that has been used to develop the model. In Chapter 4, the results of the experiments using Zeolite are compared to the numerical model. In Chapter 5, the theoretical background of using potassium carbonate as TCM is explained. In this chapter the theoretical background for the numerical model of potassium carbonate is explained. Chapter 6 contains the results of the experiments that have been conducted using potassium carbonate as TCM. These results are compared to the numerical model, and also to the performance of the same reactor using zeolite. Chapter 7 concludes this thesis with the main conclusions and recommendations.

2 | Experimental setup

In this chapter, the experimental setup is explained in detail. Firstly, the system as a whole is explained using a schematic, then the components in the system are explained in more detail. Next, some characteristics of the reactor are defined. Lastly the characteristics of Zeolite 13X are mentioned and an experimental plan is shown.

2.1 1 liter reactor system

As mentioned in the introduction, all experiments are conducted using an open reactor system. An experimental setup has been build in order to investigate the behaviour of different TCMs, where Zeolite 13X (bead size 2.5-3.5 mm, Köstrolith 13XBFK) is used as the first TCM for testing because of the thermal and physical stability of the material [16, 21]. As mentioned in the introduction, Zeolite can be used as a TCM where water vapor is used as a sorbent. Therefore, a system is created that can be used to both add water to the TCM in the form of water vapor (discharging), as well as drying the TCM by heating dry air, effectively charging the TCM. A schematic overview of the setup is seen in Figure 2.2.

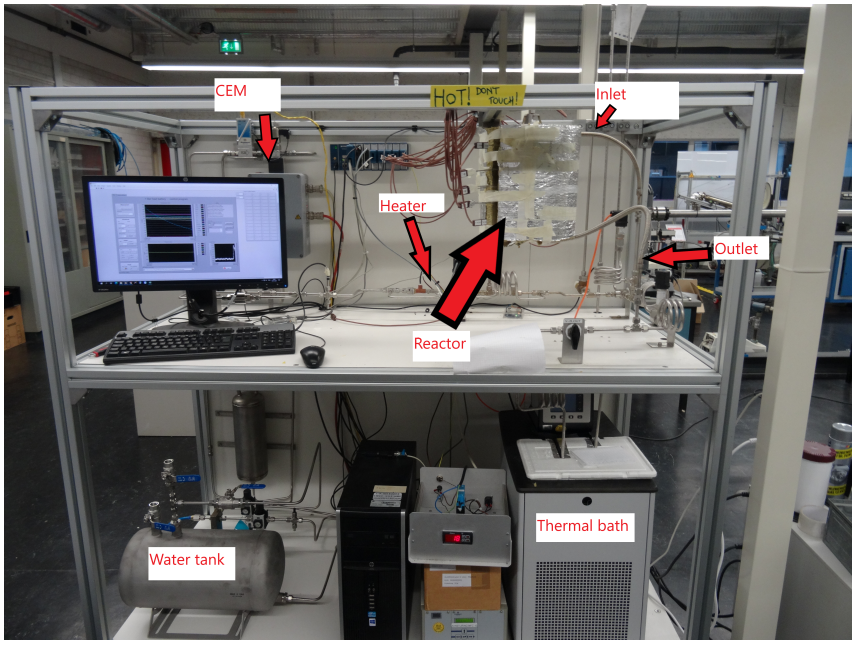

Figure 2.1: Reactor setup with the location of the CEM, heater, reactor inlet, outlet and thermal bath and water tank.

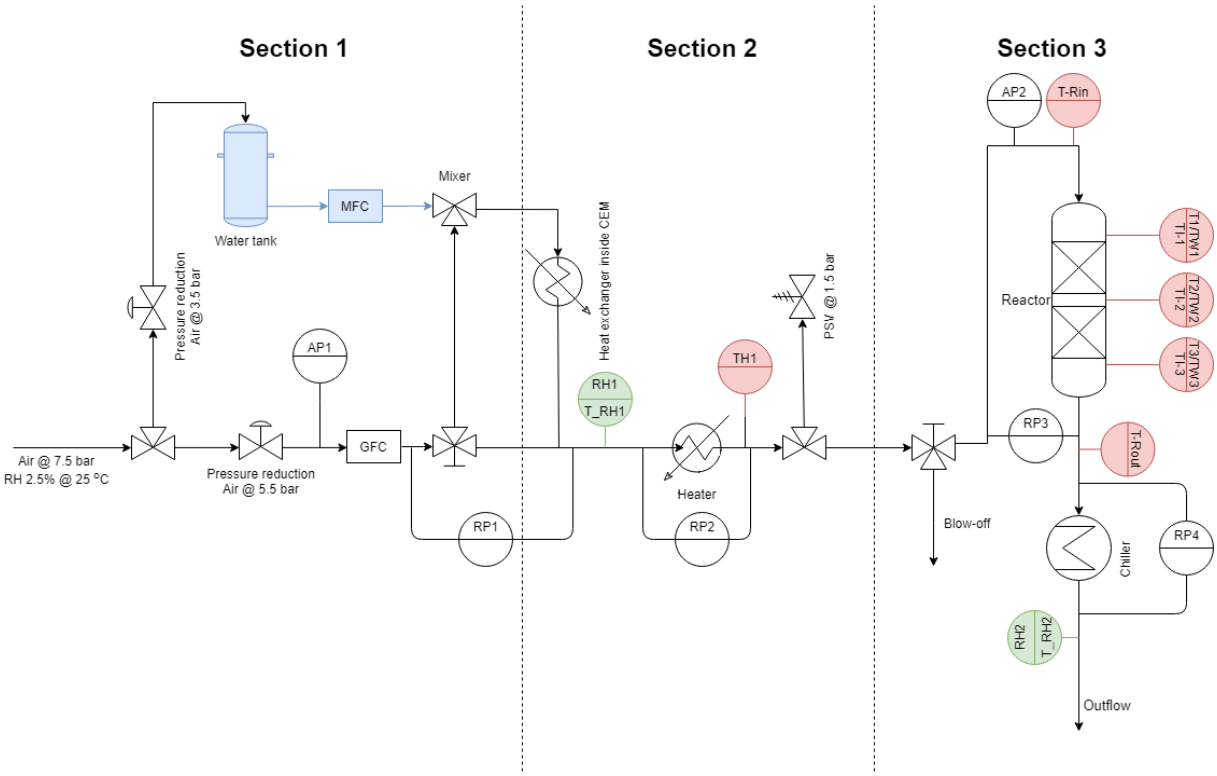

Figure 2.2: Schematic overview of the setup, including all sensors. Pressurized air (@7.5 bar) comes into the setup, where a three-way valve splits the flow towards two pressure reducers. One air flow operates as pressure for a water tank, while the other flows is used as the carrier gas. During dehydration, the water flow is set to 0 g/h. Therefore only dry air, controlled by the Gas Flow Controller (GFC), is sent through the heater (section 2), where it is heated up to high temperatures to dry the TCM. During hydration water is allowed to flow through, air and water are mixed in the Controlled Evaporator and Mixer (CEM), to create moist air that runs directly through the reactor (section 3). The abbreviations for the used sensors are: Relative Humidity (RH), temperature (T), absolute pressure (AP) and relative pressure (RP).

The first section in Figure 2.2 is used for creating moist air by evaporating water in dry air. This is done in the mixer. During dehydration dry air is surpassing the Controlled Evaporator and Mixer (CEM) and no water is flowing. Section 2 is the section where the flow is either heated to 25 °C in the CEM to prevent condensation (during hydration), or where the dry air flow is heated to 180 °C in the heater (during dehydration). In the third section, the flow is sent through the reactor, and a Relative Humidity (RH) sensor is used to check the temperature and relative humidity of the outflow. During dehydration, hot air comes out of the reactor. The RH sensor is rated for temperatures of 0 to 80 °C. To ensure staying within this region, a chiller is used for conditioning the temperature of the outflow.

The 1 liter reactor setup can be controlled in different ways. The following conditions can be set:

- CEM temperature [°C]
- Water flow [g/h]
- Air flow [g/min]
- Heater temperature [°C]

2.1.1 Reactor vessel

The inside of an assembled reactor can be seen in Figure 2.3. The reactor is a cylindrical structure. Cylindrical glass filters are used as a support for the packed bed at the bottom of the reactor and to promote a homogeneous flow at the inlet of the reactor. The inner shell of the reactor is made of Teflon, while the outer shell is made of stainless steel. The TCM is placed inside of the reactor, thereby creating a packed bed. A cross section of the reactor is shown in Figure 2.3.

Figure 2.3: The inside of an assembled reactor. Air flows in from the top, through the glass filter and the packed bed (not shown on this picture). The horizontal extractions are used for placing thermocouples at the inside of the reactor.

The inner dimensions of the reactor are: In order to reduce heat losses, the reactor is isolated. As seen

Table 2.1: Reactor dimensions

Height	144 mm
Diameter	94 mm

in Figure 2.3, on each side of the reactor, three extensions of the stainless steel layers are prominent. Therefore, exhaust wrap is used to create an even surface, around which Rockwool 810® is placed. This is shown in Appendix A.

Reactor, material and system characteristics like the pressure drops throughout the system, typical flow rates and temperature differences, as well as material characteristics like grain size [22] and porosity are taken into account. As mentioned before, the reactor is initially filled with Zeolite 13X. Later, described in Chapter 5, Zeolite 13X is replaced by K_2CO_3. Using this method of testing, the material parameters are isolated and K_2CO_3 can be reviewed on the material properties only.

2.1.2 Glass filter discs

The TCM is packed between two glass filters. The purpose of these glass filters is to both ensure the beads of the TCM stay in place, and to promote a well distributed inflow. Glass filter discs of porosity 2 from Heraeus Quarzglas GmbH & Co. KG have been used in the reactor. These glass filters are causing an increased pressure drop over the reactor, which is described in the manufacturers specification sheet by Figure 2.4.

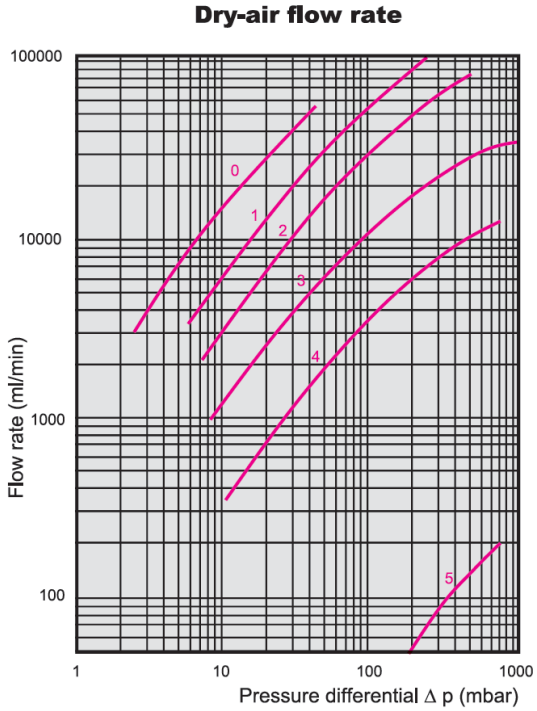

Figure 2.4: Pressure drop graph for glass filter disc with a diameter of 30 mm [23].

This figure shows the pressure drop as a function of flow rate for different filter porosity's using a disc that is 30 mm in diameter. The specific discs used in the reactor setup are 100 mm in diameter, while having only 94 mm available for actual inflow. In order to be able to read the pressure drop from Figure 2.4 a correction needs to be taken into account:

$$\dot{V}_{in}|_{30mm} = \frac{\dot{m}_{in}}{\rho_{air}} * (\frac{30}{94})^2 * 10^6 \tag{2.1}$$

Where $\dot{V}_{in}|_{30mm}$ is the reference flow rate for a 30 mm disc in [mL/min], $\dot{m}_{in}$ is the air inflow in [kg/min], ρ_{air} is the density of air for the specific pressure and temperature of the conducted experiment in [kg/m^3]. The second fraction accounts for the ration of the reference area divided by the actual area. The last term is used for conversion from m^3/min to mL/min.

2.2 Measurement equipment

In this section, the measurement equipment that is used is described. Besides the load cell, all equipment is shown in Figure 2.2. These are the Gas Flow Controller (GFC), Liquid Flow Controller (LFC), the Controlled Evaporator and Mixer (CEM), pressure sensors, the temperature sensors and the relative humidity sensors.

2.2.1 Gas and Liquid Flow controllers

Firstly, pressurized (7.5 bar) dry air (2.5% RH at 25 °C) is flowing through a three way valve, one flow is used to pressurize the water tank. The other flow is used as the carrier gas that is run through the system. The air flow is controlled by a Gas Flow Controller (GFC), made by Bronkhorst. The maximum flow rate is 100 l$_n$/min, and the working pressure is around 6 bar. The GFC is a F-202AV from Bronkhorst, which has an accuracy of $\pm$ 0.5% RD (percentage of reading) $\pm$ 0.1% FS. The GFC works as a valve. A small actuated pin acts as a flow reducer, by allowing a set amount of air to flow through. This is controlled by the GFC itself, by means of a bypass which uses two heaters to measure a part of the air flow. A laminar flow element in the main channel allows for a perfect flow split, and therefore accurate measurement of the flow. The Liquid Flow Controller (LFC) is a modified Bronkhorst L23 that is calibrated for a water flow range of 0-100 g/h with a maximum deviation of $\pm$ 0.2% FS.

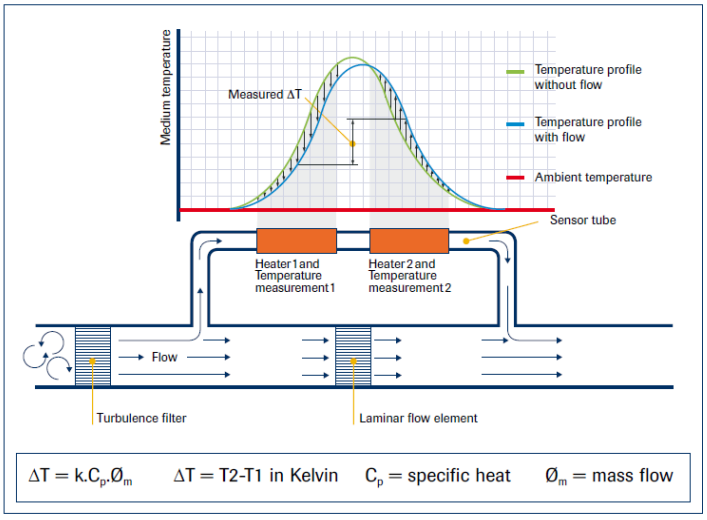

Figure 2.5: The methodology of the measurement system in the Bronkhorst Gas Flow Controller. The temperature difference in the laminar flow in the upper tube, combined with a known specific heat of dry air, is used to calculate the air flow [24].

A controlled evaporator and mixer (CEM) is used for mixing. As the name suggests, the CEM mixes the water and gas flow, to create controlled humid air. The used CEM is a Bronkhorst W-303A, which is

rated for a maximum air flow of 100 l_n/min and a maximum water flow of 100 g/h. The mixing process can also be seen in Figure 2.6

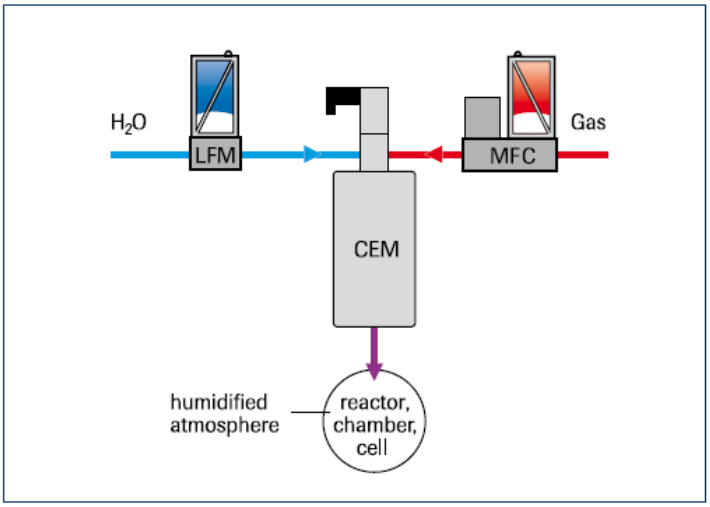

Figure 2.6: Schematic overview of the working of the CEM. Water and Gas are mixed and going through the CEM. Inside the CEM, a heating element is installed, enabling temperature control as well. Thereby a controlled humidified flow is ensured. When dry air is needed, the water flow is set to zero, and only air is flowing through the CEM into the reactor [25].

2.2.2 Pressure sensors

A variety of pressure sensors is installed throughout the setup. After the GFC, the absolute pressure is measured by means of a Keller PAA-23SY. These absolute pressure (AP) sensors have an accuracy of $\pm$ 0.25% FS. Since the full scale is 5 bar, the accuracy of the AP sensors is $\pm$ 0.0125 bar or $\pm$ 1250 Pa. Over the CEM, the relative pressure drop is measured. All relative pressure (RP) sensors are of the type Keller PD-23. Over the CEM, a sensor with a maximum pressure difference of 5 bar is used, while the other relative pressure sensors measure up to 0.2 bar of pressure difference. They all have an accuracy of 0.2% and a maximum hysteresis of 0.5% of the full scale [26]. The absolute pressure sensor 1 (AP1), combined with relative pressure sensor 1(RP1), allow for determining the pressure at the first relative humidity sensor, which in turn is used to check the set humidity. The absolute pressure is also measured right before the inlet of the reactor (AP2). Furthermore, the pressure drop over the heater (RP2), the pressure drop over the reactor (RP3) and the pressure drop over the thermal bath (RP4) are measured.

2.2.3 Temperature and humidity sensors

The temperature is monitored throughout the system using a variety of temperature sensors. After the CEM, the temperature is measured using a Sensirion SHT85 sensor (T_RH1), which also measures the relative humidity. This temperature and humidity sensor has a typical accuracy of $\pm$ 0.1 °C in the operating range of 0 to 80 °C. This type of sensor is also used to measure the temperature at the outlet of the total system (T_RH2 in green on Figure 2.2). After the first sensor (T_RH1 in green), air is flowing through the heater, after which the temperature is measured using an OMEGA TC-J-1/4NPT-U-72-DUAL. In the reactor itself, the temperature is monitored using a total of 11 thermocouples of the Type T (405-385) which are rated up to 400 °C. They have an accuracy of 1.0 °C or 0.75% [27]. The schematic overview of the locations of the thermocouples can be seen in Figure 2.7.

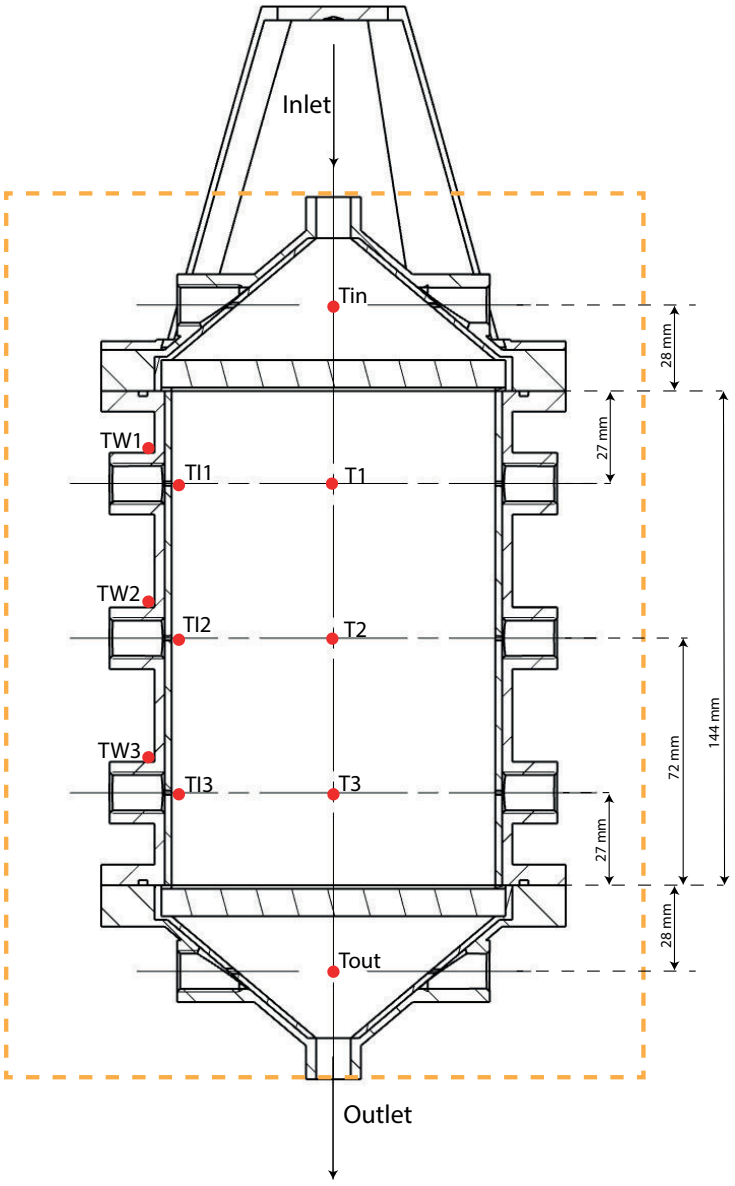

Figure 2.7: Schematic overview of the reactor, including the total of 11 thermocouples. Five thermocouples monitor the center of the reactor, from the inlet (T_{in}), to T_1 to T_3 in the packed bed, then after the glass filter near the outlet of the reactor (T_{out}). The thermocouples T_{I1} to T_{I3} monitor the temperature just on the inside of the wall, while T_{W1} to T_{W3} monitor the temperature on the outside surface of the stainless steel. The orange dashed line represents the outer layer of insulation.

The thermocouples in the inside of the reactor (so excluding the reactor in and outlet), are located at three different heights (27 mm, 72 mm and 117 mm), at three different radii from the center (0 mm, 47 mm and 65 mm).

Before entering the heater and the reactor, the relative humidity is measured as a control measurement of the in-going flow (RH1). After the reactor the relative humidity is measured again (RH2). During dehydration, the outflow of the reactor can be above 80 °C. In order to stay within operating range of the humidity sensors, the flow is cooled using a thermal bath. During hydration, both sensors are used to see whether the TCM is saturated. If the material is saturated, the amount of water vapor at the inlet and outlet of the reactor should be equal. At equal temperatures this results in an equal RH measured at RH1 and RH2. During dehydration, RH2 can be used to calculate the amount of water that is released from the TCM. The RH sensors are Sensirion SHT85, with a typical accuracy of $\pm$ 1.5% RH [28]. As mentioned in the previous subsection, these sensors also measure temperature, with a typical accuracy of $\pm$ 0.1 °C.

2.2.4 Load cell

In order to better characterize the water uptake inside the reactor during operation, the weight of the total reactor is measured using a load cell. The load cell measures the weight from the top part of the load cell. In order to minimize the influence of stress exerted by the tubing, flexible tubing is used between the reactor and the inlet and outlet tubing.

The total amount of water that can be adsorbed or absorbed can be theoretically determined, and can be checked using this load cell. With the maximum weight of water known, the state of charge can be determined throughout the hydration or dehydration process. During operation the reactor weight deterimined by the load cell can be compared to the water that is exhausted, measured using RH2. This gives two ways to determine the state of charge at each point in time of the hydration/dehydration process.

For the experiments with Zeolite, this load cell is a Zemic L6D-C5 with a maximum capacity of 8 kg, which has a maximum error of $\pm$ 0.0230% FS. This comes down to an accuracy of $\pm$ 1.84 g. During the experiments conducted with potassium carbonate as TCM, this load cell is replaced by a Zemic L6D-C5 with a maximum capactiy of 15 kg, again with an acuracy of $\pm$ 0.0230% FS, meaning an accuracy of $\pm$ 3.45 g. The difference between saturated and completely hydrated weight is 158 g for 650 g of Zeolite 13XBF, and 196 g for 1 kg of potassium carbonate. Therefore these sensors are are sensitive enough to measure the weight difference during the hydration and dehydration process.

2.3 Reactor properties

In this section, reactor characteristics such as the heat resistance of the walls and the pressure drop over the packed bed are discussed.

2.3.1 Heat resistance

The heat conductivity of the reactor walls can be described using the well known resistor analogy. From datasheets, a couple of necessary parameters are already known. However, the exhaust wrap has an unknown conductivity, therefore this is measured using experiments.

The total heat transfer can be described as a combination of the Fourier rate equation for steady-state conduction for conduction through every layer (Eq 2.2) and the Newton rate equation for convection at the outside surface of the insulation (Eq 2.3) [29].

$$q_r = \frac{2\pi kL}{ln(r_o/r_i)}(T_i - T_o) \tag{2.2}$$

For each layer of the reactor wall (teflon, stainless steel, exhaust wrap, insulation) this equation is the same, but their properties differ. q_r is the heat flux in [W], k is the thermal conductivity of every separate layer in [W/(m · K)] and r_i and r_o are the inner and outer radius of each layer respectively in [m], whereas T_i and T_o are the inner and outer temperature respectively in [K]. L is the height of the reactor in [m], which is equal to 144 mm. The Newton rate equation for convection is given below:

$$q_r = hA\Delta T = h2\pi r_w L \cdot (T_w - T_{amb}) \tag{2.3}$$

Here, h is the convective heat transfer coefficient in [W/(m^2· K)] and A is the surface area of the outer layer of the reactor, the insulation layer in [m^2]. r_w is the radius of the insulation in [m], T_w and T_{amb} are the wall and ambient temperatures in [K] respectively. These are measured using the thermocouples at the inner wall, as well as a thermocouple that measures the ambient temperature. When looking at the reactor setup, the schematic overview can be seen in the figure below.

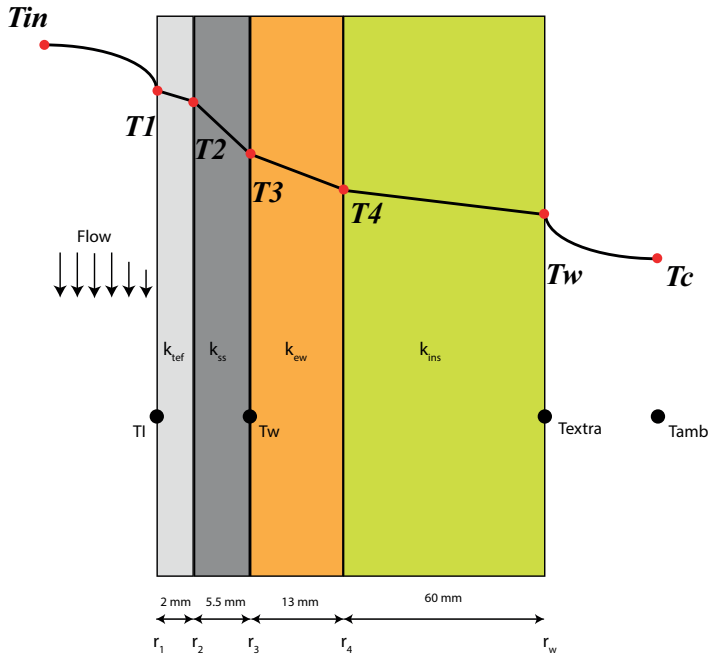

Figure 2.8: Schematic overview of the reactor including wall temperatures. From left to right, the layers are Teflon (light grey), stainless steel (dark grey), exhaust wrap (orange), and insulation (yellow). The black dots represent the available thermocouples, while the red dots represent the locations at the walls that are used for calculating the heat resistance.

During steady state, the heat flux is equal throughout every layer of the reactor, meaning that Equation 2.2 and/or Equation 2.3 can be added up by using the resistor analogy:

$$q = \frac{\Delta T}{\sum R_{thermal}} \tag{2.4}$$

Where q is the heat flux, and ΔT is the total temperature difference between the inside and outside. Each instance of $R_{thermal}$ follows from a conductive layer (subscript k) or a convective layer (subscript h) given by the following formulas:

$$R_k = \frac{ln(r_o/r_i)}{2\pi kL}; R_h = \frac{1}{h2\pi rL} \tag{2.5}$$

Again, by using steady state temperatures in the reactor, the following equation can be obtained by adding the resistances for every layer.

$$q_r = \frac{T_1 - T_{amb}}{R_{tef} + R_{ss} + R_{ew} + R_{ins} + R_h} \tag{2.6}$$

Here R_{tef}, R_{ss},R_{ew} and R_{ins} are the heat resistances in [K/W] for the conductive layers (Equation 2.5) , while R_h is the heat resistance of the outside wall in [K/W].

Table 2.2: Thermal conductivities, heat resistances and radii. All the radii are taken from the center of the reactor (center packed bed) to the given parameter.

Conductivity Teflon	k_{tef}	0.25 W/(m· K)
Conductivity stainless steel	k_{ss}	16 W/(m· K)
Conductivity exhaust wrap	k_{ew}	0.17 W/(m· K)
Conductivity Rockwool insulation	k_{iso}	0.036 W/(m· K)
Inner radius reactor	r_1	0.047 m
Radius to outside Teflon	r_2	0.049 m
Radius to outside stainless steel	r_3	0.0545 m
Radius to outside exhaust wrap	r_4	0.0675 m
Radius to outside Rockwool insulation	r_w	0.1275 m
Heat resistance Teflon	R_{tef}	0.18 K/W
Heat resistance stainless steel	R_{ss}	0.00735 K/W
Heat resistance exhaust wrap	R_{ew}	1.39 K/W
Heat resistance insulation	R_{iso}	17.57 K/W

For the third layer of the reactor, the exhaust wrap (orange layer between T_3 and T_4 in Figure 2.8), the conductivity was not known beforehand. Therefore it has been experimentally determined based on the principle of equal heat flux at steady state. As can be seen in Figure 2.8, the temperature can be measured at T_1, T_3, T_w and T_{amb}. At the outside of the insulation, an extra thermocouple is used to measure the temperature of the outside of the insulation. An experiment is conducted, where air flow was set to 100 g/min and the air temperature to 180 °C. After around 8 hours, steady state in the reactor is reached.
The heat transfer coefficient of the exhaust wrap is determined as follows. First the radial heat flux is determined:

$$q_r = \frac{T_I - T_w}{R_{tef} + R_{ss}} \tag{2.7}$$

Then the total conductive resistance is equal to:

$$R_{cond,tot} = \frac{T_I - T_{extra}}{q_r} = R_{tef} + R_{ss} + R_{iso} + R_{ew} \tag{2.8}$$

In this last equation, only one unknown remains, which is R_{ew}. Using Equation R_k 2.5 the thermal conductivity of the exhaust wrap can be determined, which is equal to 0.20 W/(m· K). Data is shown in Table B.1 in Appendix B.

All the conductive parameters are known, while also the convection parameters have to be determined. This is done by using the assumption that a vertical cylinder can be seen as a vertical plate if the following holds [29]:

$$\frac{D}{L} \geq \frac{35}{Gr^{1/4}} \tag{2.9}$$

This represents that the thickness of the boundary layer is small relative to the reactor diameter. Here, D is the outer diameter, which is equal to 0.255 m, L is the height of the reactor and equal to 0.144 m. Gr is the dimensionless Grashof number, which is equal to:

$$Gr = \frac{\beta g L^3 \Delta T}{\nu^2} = \frac{g L^3 \Delta T}{T_f \nu^2} \tag{2.10}$$

Here β is the coefficient of thermal expansion, which is approximately $1/T_f$ for ideal gases, where T_f is the film temperature. The film temperature is the average of the wall temperature and ambient temperature. g is the gravitational acceleration (9.81 m/s^2), L is the height of the reactor (0.144 m), and ν is the kinematic viscosity of air (16.14E-6 m^2/s). For this reactor setup, this statement holds (see Appendix G). According to Welty, for a vertical plate, the mean heat transfer coefficient is equal to [29]:

$$h_c = \frac{4}{3}\frac{k}{L} f(Pr)[\frac{Gr}{4}]^{1/4} \tag{2.11}$$

Here, k is the conductivity of the outside material, in this case the Rockwool insulation layer, in [W/(m· K)], L is the height of the reactor in [m]. $f(Pr)$ is a factor dependent on the Prandtl number, which is equal to 0.536 and taken from Welty [29]. Using these formulas, a natural convection coefficient of 5.12 W/(m^2 · K) is found, see Appendix G for the full calculation.

Another important parameter to account for is the heat loss to the outside air from the tubing before the reactor inlet. The CEM and the heater give the ability to heat the air up to 180 °C before it enters the reactor. However, the exact temperature needs to be known at the reactor inlet in order to control humidity. Therefore good understanding of the heat losses that occur during the experiment is required. Experiments have been conducted to determine the temperature losses in the piping. Following the following equation

$$T_{reactor,in} = T_{heater} - \Delta T \tag{2.12}$$

Where $T_{reactor,in}$ is the inlet temperature of the reactor in °C, T_{heater} is the temperature that is set via software for the heater in °C, and ΔT is the temperature drop between the heater and reactor inlet. The experimentally determined values can be seen in Appendix C.

2.3.2 Pressure drops and relative humidity

In order to prevent deliquescence when using potassium carbonate knowing the conditions (p,T,RH) at the inlet of the reactor is important. Knowing the exact inlet conditions also allows for better modelling of the reactor. The relative humidity is set by choosing a water flow and air flow. These are mixed in the CEM. However, relative humidity at the inlet needs to be known. Therefore the pressure drops need to be known. The general definition of relative humidity is:

$$RH = \frac{p_v}{p_{sat}} \tag{2.13}$$

With the water vapor pressure (p_v) in [Pa] and p_{sat} as the saturation pressure of water in air [Pa]. When the water vapor pressure becomes higher than the saturation pressure, water will condense. The saturation pressure is only dependent of temperature and is determined using a formula from Sonntag [30]:

$$ln(p_{sat}) = -6096.9385 * T^{-1} + 21.2409642 - 2.71193 * 10^{-2} T + 1.673952 * 10^{-5} * T^2 + 2.433502 * ln(T) \tag{2.14}$$

The water vapor pressure is the pressure that is exerted by the water particles in the air. It is part of the total air pressure (p_{tot}). When creating moist air using the CEM, the first parameter that is determined is the mixing ratio, which is defined as:

$$\zeta = \frac{\dot{m}_w}{\dot{m}_a} \tag{2.15}$$

Here $\dot{m}_w$ is the water flow in [kg/s], and $\dot{m}_a$ is the air flow in [kg/s]. Using this dimensionless number, the water vapor pressure can be calculated using the ideal gas law [31].

$$p_v = \frac{\zeta * p_{tot}}{\frac{M_w}{M_a} + \zeta} \tag{2.16}$$

Here, ζ is again the mixing ratio [-], M_w and M_a are the molar mass of water (18.01528 kg/mol) and air (28.9647 kg/mol) respectively. p_{tot} is the total air pressure, this is the sum of the pressure exerted by dry air and the pressure exerted by water particles.

The concentration can then be calculated as:

$$c = p_v RT \tag{2.17}$$

Where R is the universal gas constant and T is the temperature in [K]. This gives a total of two ways of calculating the inlet concentration. By using the measured RH and temperature via Equation 2.13 and Equation 2.14. Or when using the pressure sensors and the mixing ratio via Equations 2.15 and 2.16. As the water vapor pressure is a function of the total pressure, the total pressure needs to be accurately determined at the reactor inlet. The absolute pressure is measured right before the reactor, see AP2 in Figure A.1. As seen in Figure 2.4, the glass filters have a pressure drop that depends on the flow rate, therefore the absolute pressure at the inlet of the reactor depends on the flow rate as well. Measurements of these pressures are shown in the table below. The pressure drop over the reactor is shown as well (RP2).

Table 2.3: Pressure measured at the inlet of the reactor for different flows, along with the pressure drop over the reactor (RP2). Measurement using Zeolite as TCM.

Air flow	Absolute Pressure at inlet (AP2)	Pressure drop over reactor (RP3)
100 g/min	1.3277 bar	77.9 mbar
75 g/min	1.2388 bar	54.7 mbar
50 g/min	1.1325 bar	33.3 mbar
30 g/min	1.0643 bar	15.5 mbar

As is seen in Table 2.3, the pressure drop over the reactor follows an almost linear trend. The pressure at the inlet lies around 1.33 bar at most, which means that the air density can not be considered constant. The relative pressure drop is mostly caused by the glass filters. This can be seen in the following Figure:

As can be seen in Figure 2.9, the pressure drop over the reactor likely independent of the packed bed, as an experiment using an empty reactor shows a higher pressure drop. This might be caused by the fact that the reactor inlet temperature was 6 °C higher during the empty reactor experiment (23.6 °C versus 17.6 °C), therefore causing a higher volume flow. Following from Figure 2.4, a higher volume flow causes a larger pressure drop over the glass filters.

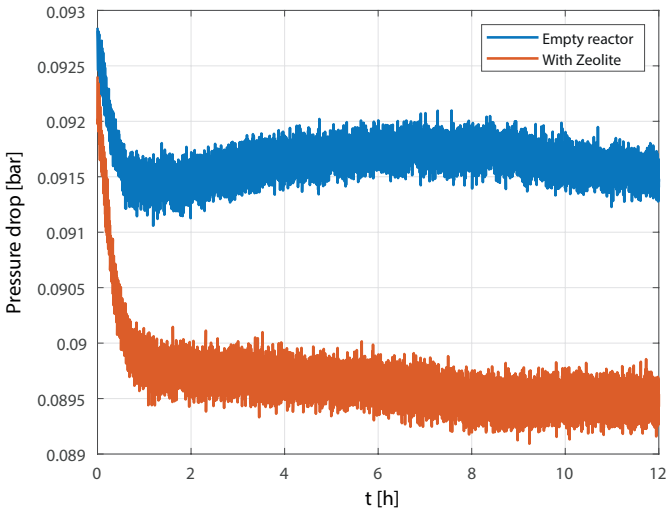

Figure 2.9: Pressure drop over the reactor for two different experiments, the blue line is from an experiment without TCM, the orange line is taken from an experiment with Zeolite 13X. Both are measured using RP3.

2.4 Zeolite 13X

In this section, the characteristics of Zeolite 13X as a TCM are discussed. The used TCM is Köstrolith Zeolite 13XBFK from CWK Bad Köstritz , of which the specifications are listed below.

Table 2.4: Specifications of dry Zeolite 13X provided by the manufacturer.

Average bead size	2.5-3.5 mm
Bulk density (not compacted)	650 g/l

2.4.1 Water uptake

The water uptake of Zeolite can be described using several different adsorption isotherms. Best known are Langmuir, Langmuir-Freundlich and Dubinin-Astakhov.The Langmuir adsorption isotherm is based on a detailed molecular model , which makes it possible to obtain numerical values of the adsorption equilibrium [32]. The Dubinin-Astakhov isotherm is based on the micro-filling theory of Polanyi, which is a more theoretical approach towards solid-gas adsorption.

Gaeini found that the Langmuir-Freundlich adsorption isotherm gave a good representation of the actual adsorption of water [33]. The equilibrium loading (the water loading of the Zeolite at which it is saturated) is determined as follows:

$$q_{eq} = \frac{q_{max}(bp_v)^{1/n}}{1 + (bp_v)^{1/n}} \tag{2.18}$$

Where q_{max} is the maximum water loading at high water vapor pressure in [mol/kg], p_v is the water vapor pressure in [Pa] and b and n are temperature dependent parameters, that are defined as [34]:

$$b = b_0 exp\left(\frac{\Delta E}{RT_0}(\frac{T_0}{T} - 1)\right) \tag{2.19}$$

With the activation energy ΔE in [J/mol], R the universal gas constant and

$$\frac{1}{n} = \frac{1}{n_0} + \alpha(1 - \frac{T_0}{T}) \tag{2.20}$$

Here, T_0 is the reference temperature (273.15 K), b_0 is the adsorption affinity constant and n_0 is the exponant constant, both at reference temperature, while α is a fitting parameter. Gaeini fitted the Langmuir-Freundlich adsorption isotherms to experimental information, provided by the manufacturer. The parameters he found are shown in the table below:

Table 2.5: Parameters used for fitting the Langmuir-Freundlich model to experimental data from manufacturer [17].

Parameter	Langmuir-Freundlich value
q_{max}	19 [mol/kg]
b_0	4.002 [Pa^{-1}]
n_0	2.976 [-]
ΔE	65.572 [J/mol]
α	0.377[-]
T_0	273.15 [K]
R	8.314 [J/(K· mol]

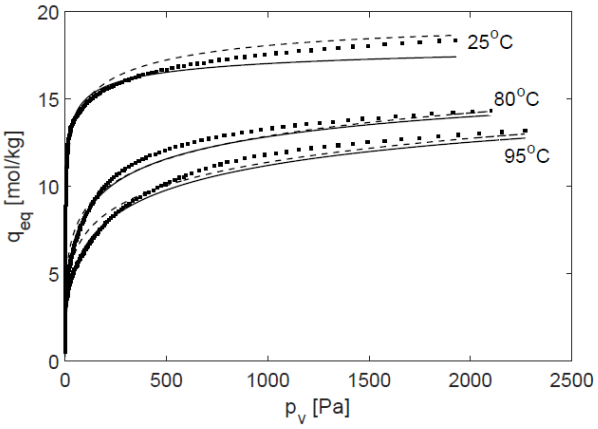

Figure 2.10: Zeolite 13X isotherms of various models, namely Langmuir-Freundlich (solid lines), Dubinin-Astakhov (dashed lines) compared to experimental data (dots) [17].

When the water loading is lower than the equilibrium loading, water is adsorped by the TCM, and when the water loading is higher than the equilbrium loading, water is released by the TCM. Several isotherms have been plotted in Figure 2.10.

One can immediately see that increase of temperature causes a decrease in equilibrium loading. Therefore dehydration is performed using hot, dry air (2.5% RH 25 °C, which converts to 79 Pa of water vapor pressure). The higher the temperature, the lower the equilibrium loading. Therefore, ideally one would want to hydrate the Zeolite at temperatures as high as possible.

2.4.2 Theoretical pressure drop packed bed

As mentioned before, the pressure drop over the reactor is measured. However, the pressure drop over the packed bed alone is not measured. Therefore, the pressure drop over the packed bed is described using the Ergun equation:

$$-\frac{\partial p}{\partial z} = \alpha \frac{(1-\epsilon)^2}{\epsilon^3} \frac{\mu}{{d_p}^2} u_s + \beta \frac{(1-\epsilon)}{\epsilon^3} \frac{\rho}{d_p} u_s^2 \tag{2.21}$$

with p as the pressure in [Pa], z the axial coordinate in [m], ϵ the bed void fraction or porosity [-], μ the dynamic viscosity of air in [Pa ·s], d_p the particle diameter in [m], ρ the density in [kg/m^3] and u the superficial velocity in [m/s]. The superficial velocity is the velocity as if there was only void (equivalent to an empty reactor) and is calculated as follows:

$$u_s = \frac{\dot{m}_v}{\rho_v A_r} + \frac{\dot{m}_a}{\rho_a A_r} \tag{2.22}$$

Where A_r is the reactor area (2.776E-2 m^2), $\dot{m}$ is the mass flow of air and water vapor, depending on the subscript [kg/s]. ρ is the density of water or air [kg/m^3].

2.4.3 Theoretical output power

An important parameter for defining the performance of the materials is the output power. It is defined as:

$$P = \dot{m}_{g,out} C_{p,g,out} T_{out} - \dot{m}_{g,in} C_{p,g,out} T_{in} \tag{2.23}$$

Where the subscripts in and out, mean at the inlet of outlet of the reactor respectively. $\dot{m}_g$ is the mass flow of the gas phase in [kg/s], and $C_{p,g}$ is the specific heat of the gas phase in [J/(kg·K)]. They are defined as:

$$\dot{m}_g = \dot{m}_a + \dot{m}_v \tag{2.24}$$

and

$$C_{p,g} = C_{p,a} \cdot \frac{\dot{m}_a}{\dot{m}_g} + C_{p,v} \cdot \frac{\dot{m}_v}{\dot{m}_g} \tag{2.25}$$

Where $C_{p,a}$ is the specific heat of air (1007 J/(kg·K), and $C_{p,v}$ is the specific heat of water vapor, equal to 1895 J/(kg·K).

2.5 Experimental plan

In this section, the experimental plan is discussed into further detail. The reactor is filled with Zeolite 13X, and experiments are conducted to answer the research questions. First, experiments are conducted to find the influence of the mass flow on the temperature jump and the output power. During these experiments, the ratio between the set air flow and water flow is kept constant. The total set of conditions is found in Table 2.6.

Next, the influence of the humidity on the output power and temperature jump is investigated. This is done by experiments where the air flow is kept constant, and the water flow is varied. The set conditions for the CEM temperature, air flow and water flow of these experiments are found in Table 2.7.

All the experiments have been conducted using a cycle of hydration and dehydration. Dehydration is performed for 8 hours using an air flow of 100 g/min at 180 °C heater temperature in order to conduct

Table 2.6: Inlet conditions used for the experiments to find the influence of flowspeed on temperature increase and output power.

Experiment number	CEM temperature [°C]	Air flow [g/min]	Water flow[g/h]
1	25	97	23
2	25	75	17
3	25	53	13
4	25	31	8

Table 2.7: Inlet conditions used for the experiments to find the influence of humidity on temperature jump and power output.

Experiment number	CEM temperature [°C]	Air flow [g/min]	Water flow [g/h]
5	25	100	26
6	25	100	33
7	No setpoint	97	25
8	No setpoint	75	11
9	No setpoint	75	17
10	No setpoint	75	20
11	No setpoint	75	23

reproducable experiments. After dehydration, the GFC and MFC are set to no flow, and the reactor is cooled by means of natural convection. A schematic overview this cycle is displayed in Figure 2.11.

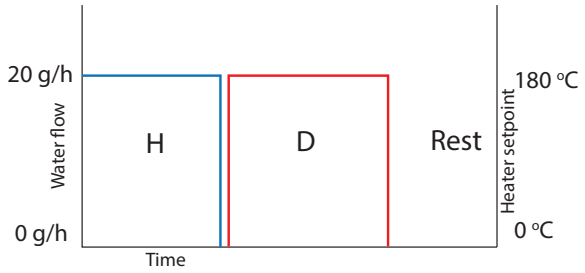

Figure 2.11: A normal hydration to dehydration cycle over time. The blue line represents the water flow over time, while the red line represents the heater temperature. In the area marked with H, hydration takes place. Afterwards, dehydration is almost immediately started (D). After the material is dried, the reactor is left at rest in order to cool down to ambient temperature over time. No flow is active during the resting period, and the reactor is closed using valves. This prevents water vapor from the surroundings to enter the setup.

A typical temperature profile of such a cycle can be seen in the Figure 2.12.

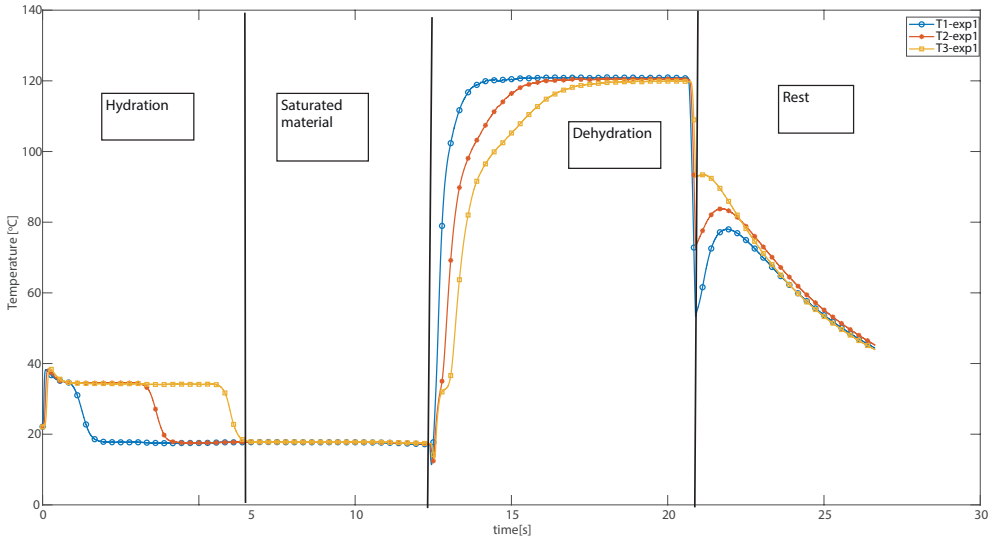

Figure 2.12: Temperature profile in the center of the packed bed during a hydration-dehydration-rest cycle.

During hydration, water vapor and air with a temperature around 17.5 °C enter the reactor. The water vapor and is adsorbed by the Zeolite, thereby releasing heat. As seen in Figure 2.12, this heat causes a temperature increase in the carrier gas to about 35 °C (from 17.5 °C). After the material is fully saturated, no heat is released any more. During dehydration, dry air enters the reactor at 120 °C. It takes time to heat the material, while also energy is needed to evaporate water. Before the 8 hours are passed, the complete center of the packed bed has a temperature of 120 °C. After dehydration, the reactor is left to cool down using natural convection.

The dips in temperature shortly after dehydration are due to cooling of the heater. In order to safely cool it down, for 15 minutes the temperature of the heater is dropped down from a setpoint of 180 °C to 0 °C. This causes the material to cool down as well. After this period, no flow is going through the reactor.

During experiments 1 to 6, the CEM heater is set to 25 °C in order to be sure that the water vapor pressure does not exceed the saturation pressure during experiments. Thereby preventing liquid to be formed in the setup. During the experiments, the CEM heater could not be precisely controlled. The temperature of the CEM resulted in significant overshoot as soon as the temperature of the air stream dropped below the CEM temperature setpoint. A second experiment is performed with the CEM heater switched off. In this way it can be determined whether the CEM heater is required, or if one can do experiments without. It turned out that the heater was not necessary as the relative humidity stayed below 70% at all times during experiments, and therefore no liquid was formed before or in the reactor.

3 | Numerical model Zeolite

In order to be able to find the best possible working conditions for the reactor setup, a continuum model is made in COMSOL Multiphysics. First, the development of a velocity profile throughout the packed bed is created. Then, the correlation between the TCM particles and the carrier gas is explained. Next the mass and energy balances are setup, including different methods to determine the diffusion parameters. The results of the numerical model are later compared to experiments in Chapter 4.

3.1 Velocity profile

A packed bed reactor is a very popular type of reactor, due to the simplicity of such a system. Lots of research is therefore conducted on the description of the phenomena inside a packed bed. Due to the difficulty of describing the inside of a packed bed, a relatively simple approach is preferred. When the porosity of a packed bed is less than approximately 0.7, and this porosity and the flow are considered uniform, an analogy with flow in pipes is valid [35]. Equation 2.21 can be used to calculate the pressure drop over the packed bed. However, the high porosity near the walls (Figure 3.1 cause a higher velocity in the near wall region. This phenomenon is called wall channeling, and can be described in several ways.

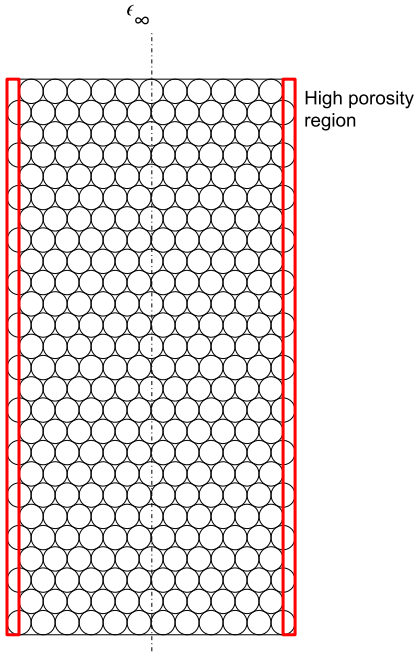

Figure 3.1: High porosity regions near the walls of the reactor.

Including a radial porosity profile instead of the average porosity gives a starting point for including wall channeling. Near the walls, the porosity is higher due to the fact that particles have to accustom to the wall. This can be seen in Figure 3.1. A porosity profile that includes the near wall effect in a relatively good way is proposed by Johnson and Kapner (1990) [36]:

$$\epsilon(r) = \epsilon_\infty \left[1 + N_1 e^{-E_1 B^k} cos(N_2 G^{E_2})\right] \tag{3.1}$$

With N_1, N_2, E_1 and E_2 as fitting parameters, and ϵ_∞ as the porosity in the center of the packed bed, and B as

$$G = \frac{r_1 - r}{\bar{d}_p} \tag{3.2}$$

Where r_1 is the outer radius of the reactor bed, r is the radial coordinate within the range of 0 to r_1 and $\bar{d}_p$ is the average particle diameter, which is 3 mm. This equation is very accurate, however it is based on fitting. As the porosity or velocity are difficult to determine, another method is needed. A porosity profile introduced by Giese (1998) also gives a relatively good representation of the actual porosity profile [37] [38].

$$\epsilon(r) = \epsilon_\infty (1 + 1.36 e^{-5G}) \tag{3.3}$$

This porosity profile of Giese does not give the same accuracy as the fit with the Johnson and Kapner. Near the wall, the porosity is found to oscillate between high and low values based on experimental data. However, the Giese profile and the profile from Johnson and Kapner do not show significant differences when it comes to heat and mass transfer [38]. Therefore, Equation 3.3 is used to determine the porosity profile in this thesis.

At the near wall region, the higher local porosity causes for a decrease of friction forces by the packed bed, while simultaneously the wall itself has a viscous boundary layer, causing an increase in flow resistance. Vortmeyer and Schuster (1983) have incroporated the Brinkman term in the Ergun equation to quantify the wall effect [39]. This leads to the following pressure drop equation:

$$-\frac{\partial p}{\partial z} = \alpha \frac{(1-\epsilon(r))^2}{\epsilon(r)^3} \frac{\mu}{{d_p}^2} u(r) + \beta \frac{(1-\epsilon(r)}{\epsilon(r)^3} \frac{\rho}{d_p} u(r)^2 - \frac{\mu_{eff}}{r} \frac{\partial}{\partial r} \left(r \frac{\partial u(r)}{\partial r} \right) \tag{3.4}$$

Equation 3.4 is used for calculating the radial velocity proifle. In Equation 3.4, μ_{eff} is the effective viscosity. Bey and Eisenberger (1997) found a correlation for a dimensionless effective viscosity for spheres [40]:

$$\frac{\mu_{eff}}{\mu_a} = 1 + \left(7 * 10^{-6} \frac{D}{d_p} + 2 * 10^{-5} \right) {Re_p}^2 \tag{3.5}$$

Here, D is the reactor diameter (94 mm), and μ_a is the dynamic viscosity of the air in [Pa·s]. The Reynolds number inside a packed bed is defined as:

$$Re_p = \frac{\rho_a u_s d_p}{\mu_a} \tag{3.6}$$

Where u_s is the superficial velocity from Equation 2.22, and ρ_a is the density of air in [kg/m^3] Equation 2.21 is used to determine the theoretical pressure drop over the packed bed. The pressure drop over the packed bed does not change significantly by incorporating wall channeling. The pressure drop over the packed bed is inserted in Equation 3.4 to give a radial velocity profile using the following boundary conditions:

$$r = 0 \longrightarrow \frac{\partial u}{\partial r} = 0 \tag{3.7}$$

$$r = r_1 \longrightarrow u = 0 \tag{3.8}$$

3.2 Governing equations for heat and mass transfer

With the given velocity profile throughout the reactor, the governing equations for heat and mass transfer are derived. After defining the assumptions, the mass balance, heat balance and water loading partial differential equations (PDEs) are defined.

3.2.1 Assumptions

In order to build a model that is both relatively fast to compute, while being physically accurate, the following assumptions are made:

- The carrier gas and water vapor are both seen as ideal gases [13];
- The gas and solid phase are in local thermal equilibrium;
- The beads are identical in shape and properties;
- Besides the porosity profile, the properties of the bed are considered uniform.

3.2.2 Mass balance

The mass balance can be expressed as a water vapor concentration differential equation, as the only mass exchange happening inside the reactor is that of water vapor. Therefore the mass balance for concentration can be written as:

$$\epsilon(r)\frac{\partial c}{\partial t} + u(r)\frac{\partial c}{\partial z} - \frac{1}{r}\frac{\partial}{\partial r}\left[rD_r(r)\frac{\partial c}{\partial r}\right] - D_z(r)\frac{\partial^2 c}{\partial z^2} + (1-\epsilon(r))\,\rho_p\frac{dq_v}{dt} = 0 \tag{3.9}$$

Here the terms from left to right are as accordingly: Accumulation, convection, two diffusion terms, one in the radial direction and one in the axial direction, and lastly a source term in the form of water loading in the solid phase. D_r and D_z are the mass dispersion coefficients in the radial and axial direction respecitvely in [m^2/s], while ρ_p is the particle density in [kg/m^3], and $\frac{dq_v}{dt}$ is the time derivative of the water loading in the solid phase [mol/(kg·s)]. $\epsilon(r)$ is the radial porosity profile from Equation 3.3.

3.2.3 Heat balance

Using the assumption of local thermal equilibrium between the gas and solid phase, the heat balance inside the reactor is described as follows:

$$\rho\bar{C}_p\frac{\partial T}{\partial t} + \rho_g C_{p,g}u(r)\frac{\partial T}{\partial z} - \frac{1}{r}\frac{\partial}{\partial r}\left[r\Lambda_r(r)\frac{\partial T}{\partial r}\right] - \Lambda_z(r)\frac{\partial^2 T}{\partial z^2} - (1-\epsilon(r))\rho_p\frac{dq_v}{dt}\Delta H = 0 \tag{3.10}$$

Here, Λ is the heat dispersion coefficient in the radial (subscript r) and axial (subscript z) direction. ΔH is the reaction enthalpy and $\rho\bar{C}_p$ is the overall volumetric heat capacity. This heat capacity consists of the heat capacity of the air in the voids, the heat capacity of the air in the pores, the heat capacity of the particles, and the heat capacity of adsorbed water. It can be estimated using:

$$\rho\bar{C}_p = \epsilon(r)\rho_g C_{p,g} + (1-\epsilon(r))\epsilon_p\rho_p C_{p,g} + (1-\epsilon(r))\rho_p C_{p,s} + (1-\epsilon(r))\rho_p\bar{q_v}C_{p,v}M_v \tag{3.11}$$

Where the subscripts g, s and v stand for gas(air), solid (Zeolite) and vapor (water vapor) respectively. ρ_p is the particle density, and ϵ_p is the particle porosity.

The differential equation used to describe the conductive heat transfer in each layer of the wall is:

$$\rho_w C_{P,w} \frac{\partial T_w}{\partial t} - \frac{1}{r}\frac{\partial}{\partial r}\left[r k_w \frac{\partial T_w}{\partial r}\right] - k_w \frac{\partial^2 T_w}{\partial z^2} = 0 \tag{3.12}$$

Where for each layer the material properties ρ_w, $C_{P,w}$ and k_w differ. The heat flux from the packed bed to the inside wall, and the outside wall to ambient are both defined as a convective heat flux:

$$\dot{Q} = hA(\Delta T) \tag{3.13}$$

For the external surface of the reactor, the heat transfer coefficient h is defined in Equation 2.11. The heat transfer coefficient from the air inside the reactor to the teflon is defined as:

$$h_i = \frac{Nu_w k_f}{d_p} \tag{3.14}$$

The heat transfer coefficient is often defined as the sum of a flow-dependent heat transfer, and a flow-independent heat transfer [41]. This is seen back in the Nusselt number that is used in Equation 3.14. The Nusselt number is based on research from Martin and Nilles (1993) [42].

$$Nu_w = Nu_{wo} + 0.19 Re^{0.75} Pr^{-0.42} \tag{3.15}$$

Where the second term is flow dependent. Re is the Reynolds number as defined in Equation 3.6 and Pr is the Prandtl number, which is

$$Pr = \frac{\mu_a C_{p,a}}{k_a} \tag{3.16}$$

With μ_a the dynamic viscosity of air in [Pa·s], $C_{p,a}$ the heat capacity of air in [J/(kg·K)] and k_a the thermal conductivity of air in [W/(m·K)].

Nu_{wo} in Equation 3.15 is independent of the flow. Nu_{wo} is defined as

$$Nu_{wo} = \left(1.3 + 5\frac{d_p}{D}\right)\frac{k_b}{k_a} \tag{3.17}$$

Where k_b is the effective thermal conductivity of the packed bed. This is a combination of the conductivity of the fluid/gas and the solid, and can be estimated using the model from Zehner and Schlunder (1970) [43] [44]:

$$\frac{k_b}{k_a} = 1 - \sqrt{1-\epsilon_b} + \frac{2\sqrt{1-\epsilon_b}}{1-B/\beta}\left(\frac{(1-1/\beta)B}{(1-B/\beta)^2} ln(\frac{\beta}{B}) - \frac{B+1}{2} - \frac{B-1}{1-B/\beta}\right) \tag{3.18}$$

Where β is equal to the conductivity ratio of the particles and the gas, $\beta = k_p/k_a$ and B is

$$B = C\left(\frac{1-\epsilon_b}{\epsilon_b}^{10/9}\right) \tag{3.19}$$

Here, C is the shape factor, which is suggested to be 1.25 for spheres. This model works well compared to experimental data for a porosity of 0.4 and $\beta^{-1} < 10^3$, which is the case when using Zeolite and (moist) air [44].

3.2.4 Source term

The heat source in the system is the released heat inside the packed bed during adsorption. The concentration dependent isosteric heat of adsorption is defined as follows [34]:

$$\Delta H = \Delta E - (\alpha R T_0) n^2 ln \left(\frac{q}{q_{max} - q} \right) \tag{3.20}$$

Where the meaning of ΔE is the isosteric heat of adsorption at half loading [17]. R is the gas constant and T_0 is the reference temperature. The numerical values of all modelling parameters (including n and α) are shown in Table 2.5.

Equation 3.20 shows that the adsorption enthalpy is a function of the water loading q only. This can be seen in Figure 3.2.

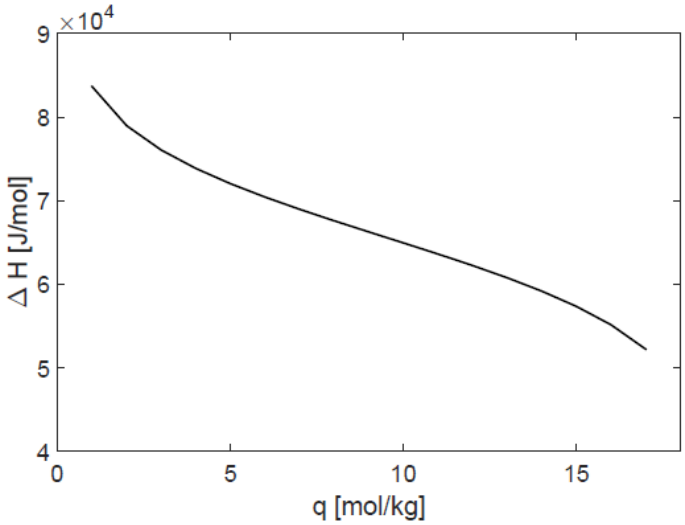

Figure 3.2: Adsorption enthalpy of Zeolite 13XBF as a funciton of water loading [17].

3.3 Diffusion

In the previous subsections, the mass dispersion and heat diffusion coefficient have been briefly mentioned. In this section, they will be described in detail, as well as how they are described in the 2D model.

Dispersion in general is defined as the spreading of mass from high concentration areas to low concentration areas. Dispersion is highly dependent of the gas flow. For low flow rates, molecular diffusion is the main cause of dispersion, while for high flow rates convective dispersion is dominant. The dispersion coefficients are described for both mass and heat transfer, and are seperated into the axial and radial direction.

3.3.1 Axial dispersion

The dispersion model used is that of Winterberg (2000) [45]. It is found to have great overall performance against experimental data. Both the axial mass and thermal dispersion coefficients are calculated using the VDI-Wärmteatlas from the chapter of Tsotsas (1997) [46], with the mass dispersion coefficient as:

$$D_{ax} = D_b + \frac{Pe_m}{K_{ax}} D_m \tag{3.21}$$

In Equation 3.21, D_b is the effective diffusion coefficient without flow. The value used for K_{ax} is 2. It theoretically estimated from the equivalence of the dispersion model to a CSTR-cascade [45,47]. Zehner and Schlünder provide a correlation between the effective diffusion and the porosity of the packed bed in the form of [43]:

$$D_b = D_m \left(1 - \sqrt{1 - \epsilon(r)}\right) \tag{3.22}$$

Where D_m is the molecular diffusion coefficient of water and air (the gas phase). This has been estimated using Chapman-Enskog theory for air and water [48]:

$$D_m = -2.775E^{-6} + 4.479E^{-8}T + 1.656E^{-10}T^2 \tag{3.23}$$

The molecular Péclet number for mass transfer in Equation 3.21 is defined as

$$Pe_m = \frac{\bar{u_s} d_p}{D_m} \tag{3.24}$$

With again, u_s as the superficial velocity and d_p the particle diameter.

The axial thermal dispersion coefficient is defined as

$$\Lambda_{ax} = k_b + \frac{Pe_h}{K_{ax}} k_f \tag{3.25}$$

The effective thermal conductivity of the packed bed k_b can be estimated using Equation 3.18. Pe_h is the molecular Péclet number for heat transfer, which is defined as

$$Pe_h = \frac{\bar{u_s} d_p \rho_a C_{p,a}}{k_a} \tag{3.26}$$

Where u_s is the superficial velocity, ρ_a is the density of air, C_p is the heat capacity of the air and k_a is the conductivity of air. d_p is the particle diameter, which is 3 mm for Zeolite 13X.

3.3.2 Radial dispersion

For radial dispersion, several relations are proposed in literature. The proposals in the work of Cheng and Vortmeyer (1988) [49] have been used as radially variable thermal conductivities. The radially variable thermal conductivity uses the velocity at the center of the bed: u_c [45]. This gives the following equation for the thermal dispersion coefficient:

$$\Lambda_r(r) = k_b + K_{1,h} Pe_h \frac{u_c}{\bar{u_s}} f_h(r_1 - r) k_a \tag{3.27}$$

Where k_b is the effective conductivity of the packed bed, following from Equation 3.18. $K_{1,h}$ is a fitting parameter, the Peclet number Pe_h follows from Equation 3.26. $\bar{u_s}$ is the mean value of the velocity inside the packed bed in [m/s], r_1 is the inside radius of the reactor (0.047m, see Table 2.2) and r is the radius within the reactor ($r_1 > r > 0$). k_a is the conductivity of the air in [W/(m·K)]. f_h is defined as:

$$f_h(r_1 - r) = \begin{cases} \left(\frac{r_1 - r}{K_{2,h} d_p}\right)^{n_h} & \text{if } 0 < r_1 - r \leq K_{2,h} d_p \\ 1 & \text{if } K_{2,h} d_p < r_1 - r \leq r_1 \end{cases} \tag{3.28}$$

The parameters $K_{1,h}$, $K_{2,h}$ and n are fitting parameters based on experimental data. Their values are shown in Table 3.1.

Similar to the radial heat dispersion coefficient, the radial mass transfer coefficient is defined as follows:

$$D_r(r) = D_b + K_{1,m} Pe_m \frac{u_c}{\bar{u_s}} f_m(r_1 - r) D_m \tag{3.29}$$

With D_b the effective dispersion coefficient of the packed bed, defined in Equation 3.22. Pe_m is the Peclet number for mass transfer (Equation 3.24, and D_m is the molecular diffusion coefficient from Equation 3.23. f_m is defined as:

$$f_m(r_1 - r) = \begin{cases} \left(\frac{r_1 - r}{K_{2,m} d_p}\right)^{n_m} & \text{if } 0 < r_1 - r \leq K_{2,m} d_p \\ 1 & \text{if } K_{2,m} d_p < r_1 - r \leq r_1 \end{cases} \tag{3.30}$$

Where the values of $K_{1,m}$, $K_{2,m}$ and n are based on fitting. Winterberg determined these parameters to be equal to the values shown in Table 3.1 [45]:

Table 3.1: Parameters for heat and mass dispersion modeling [45]

Parameter	Mass dispersion	Thermal dispersion
n	2	2
K_1	$8\left(1 + \frac{3}{Pe_{m,c}^{0.5}}\right)$	8
K_2	0.44	$0.44 + 4exp(-\frac{Re_p}{70})$

$Pe_{m,c}$ is the molecular Péclet number seen in Equation 3.24, using the center velocity u_c instead of the mean superficial velocity. The center velocity is determined by solving Equation 3.4. This gives a radial velocity profile, where $u(r = 0) = u_c$.

3.3.3 Kinetics

Adsorption kinetics are of great interest of (chemical) engineers all around the world. Packed beds can be modelled using computational intensive models, such as Chemical Potential Driving Force (CPDF) or Fickian Diffusion (FD) model. However, the Linear Driving Force (LDF) model, with a lumped mass transfer coefficient is very useful for practical analysis. It is simple, analytical and physically consistent [50]. Therefore, this model is used to describe the kinetics.

The water loading in the solid phase is briefly discussed in Subsection 2.4.1. The water loading derivative is described as:

$$\frac{dq}{dt} = k^*_{LDF}(q_{eq} - q) \tag{3.31}$$

Where q is the loading in [mol/kg], and q_{eq} is the equilibrium loading in [mol/kg]. q_{eq} is determined using Equation 2.18. k^*_{LDF} is the corrected coefficient which includes the concentration dependency [51]. It is defined as:

$$k^*_{LDF} = k_{LDF}\left(\frac{\rho_p RT}{\epsilon_p}\frac{\partial q_{eq}}{\partial p_v}\right) \tag{3.32}$$

The partial derivative from the equilibrium loading (q_{eq}) to the water vapor pressure (p_v) is determined via Equation 2.18.The first term on the right hand side, k_{LDF} is the lumped parameter that consists of terms that describe the macropore resistance, the micropore resistance and the external film resistance. It is defined as:

$$k_{LDF} = \left(\frac{d_p}{6k_f} + \frac{d_p^2}{60\epsilon_b D_p}\right)^{-1} \tag{3.33}$$

Where d_p is the particle diameter (3 mm), and D_p the macropore diffusivity [m^2/s]. In Equation 3.33, $\frac{d_p}{k_f}$ is the representation of the external film resitance. k_f is the mass transfer coefficient of the external film, and can be obtained using the Sherwood number in the following correlation [52]:

$$Sh = \frac{k_f d_p}{D_m} = 2 + 1.1Sc^{1/3}Re_p^{0.6} \tag{3.34}$$

Where the Reynolds number (Re_p) is defined using Equation 3.6 and the Schmidt number Sc number is defined as:

$$Sc = \frac{\mu_a}{\rho_a D_m} \tag{3.35}$$

Where μ_a is the dynamic viscosity of air, ρ_a the density of air and D_m the molecular diffusivity (Equation 3.23). Lastly, D_p in Equation 3.33 is the description of the macropore diffusivity, which is described using the theory of Crittenden and Thomas (1998) [53]:

$$D_p = \frac{1}{\tau}\left(\frac{1}{D_m} + \frac{1}{D_k}\right)^{-1} \tag{3.36}$$

Where τ is the tortuosity, which is estimated to be $\tau = 1 - 0.41ln(\bar{\epsilon_b})$ [54], D_m is the aforementioned molecular diffusivity, and D_k is the Knudsen diffusivity. Knudsen diffusivity is a type of diffusion which occurs when the mean free path of molecules involved is comparable to or larger than the length scale of the system [55]. It is calculated using [53]:

$$D_k = \frac{1}{3}d_p\left(\frac{8RT}{\pi M_w}\right)^{1/2} \tag{3.37}$$

Where R is the universal gas constant and M_w is the molecular mass of water vapor [g/mol].

3.4 Boundary conditions and software

Using the described equations, a set of boundary conditions is set in order to be able to calculate the differential equations. The software used to create the model is COMSOL Multiphysics 5.5. A time-dependent Backwards Differentiation Formula (BDF) solver with a maximum order of 5, and a minimum order of 1 has been used to find a solution. The initial time step has been set to 0.001 s, and time stepping has been set to strict, with a maximum time step of 20 s, chosen manually. This prevents the model from making large errors at the beginning of the simulation.

3.4.1 Boundary and initial conditions

A 1D velocity model is used to determine the radial velocity profile. This is described in Subsection 3.1. This velocity profile is used as input for the 2D-model, which uses the PDE's described in this chapter. They are solved using the following initial and boundary conditions:

$$t = 0 \longrightarrow T_b = T_w = T_{amb}, c = 0, q = q_0 \tag{3.38}$$

$$z = L \longrightarrow T_b = T_{in}, \frac{\partial T_w}{\partial z} = 0, c = c_{in}, \frac{\partial q}{\partial z} = 0 \tag{3.39}$$

$$z = 0 \longrightarrow \frac{\partial T_b}{\partial z} = 0, \frac{\partial T_w}{\partial z} = 0, \frac{\partial c}{\partial z} = 0, \frac{\partial q}{\partial z} = 0 \tag{3.40}$$

$$r = 0 \longrightarrow \frac{\partial T_b}{\partial r} = 0, \frac{\partial c}{\partial r} = 0, \frac{\partial q}{\partial r} = 0 \tag{3.41}$$

$$r = r_1 \longrightarrow \frac{\partial c}{\partial r} = 0, \frac{\partial q}{\partial r} = 0 \tag{3.42}$$

The location of these boundary conditions are also shown in Figure 3.3. This figure is directly taken from the COMSOL Multiphysics interface.

Discretization is done by using Lagrange linear shape functions. The complete model is meshed using a maximum element size of 0.0016 m. This results in a mesh with a total of 20450 elements. The results of a mesh convergence study are shown in Appendix E.

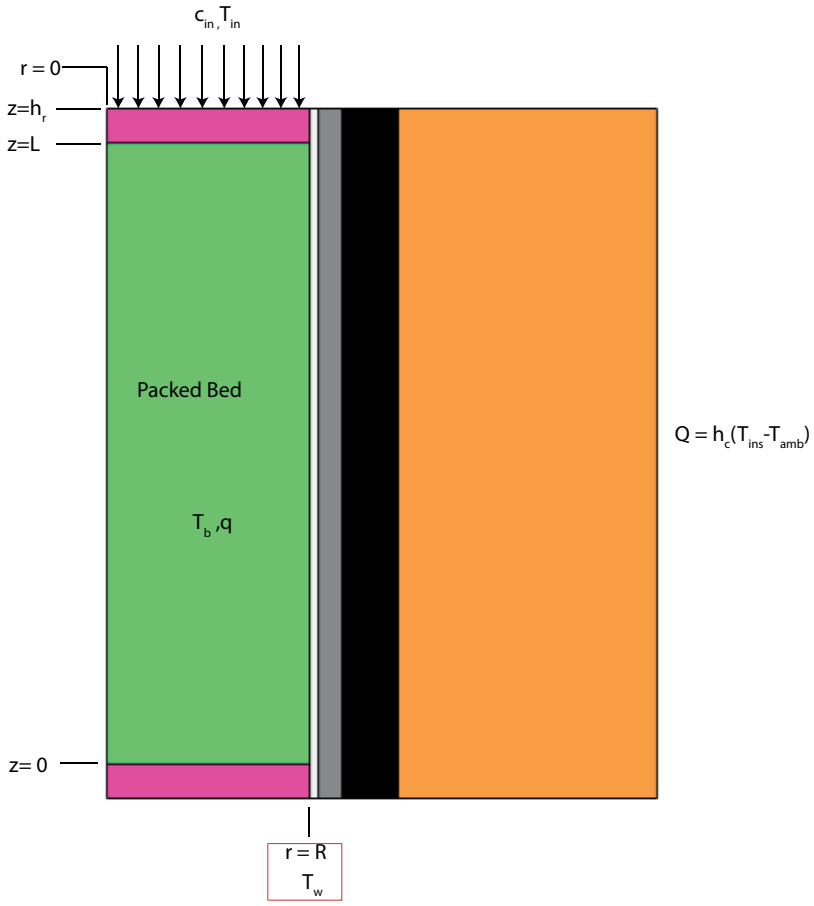

Figure 3.3: Graphical overview of the geometry that is modelled in Comsol, with the glass filters in pink, the packed bed in green. From left to right, the walls are made up of Teflon (white), stainless steel (grey), exhaust wrap (black) and Rockwool (orange).

4 | Results Zeolite

The performance of the reactor and Zeolite as TCM is shown in this chapter. First, the experimental results are shown. The influence of mass flux (or flow rate) through the system, the influence of the set humidity, and the influence of inlet temperature are shown using temperature graphs over time. Then, they are compared to the numerical model, and any discrepancies are explained. Lastly, the maximum power and total power output of different experiments are evaluated.

4.1 Relative humidity throughout system

In the system explained in Chapter 2, water vapor is created in the CEM to have adsorped by different TCMs. In this chapter, water adsorption of Zeolite 13X is investigated. To ensure proper conclusions are drawn, the inlet conditions need to be known. The humidity is calculated beforehand and compared to measurements from RH1.

To investigate if the humidity can be calculated properly, the calculations are done on the location of RH1. This means that pressure data is by subtracting $RP1$ from $AP1$. Due to deviations in the temperature at this location, choosing a value beforhand would cause large deviations as well. These deviations are caused by the aforementioned issues with the CEM (see Section 2.5). Therefore temperature data is taken from $T - RH1$.

This temperature data is used in Equation 2.14 to get a saturation pressure. The mixing ratio is calculated by using Equation 2.15, which is set by using the gas flow from the GFC and the liquid flow from the LFC. Then the water vapor pressure is calculated using Equation 2.16, where p_{tot} is calculated by substracting $RP1$ from $AP1$. Using the calculated water vapor pressure and saturation pressure, the RH is calculated using Equation 2.13. The results are compared to data that is measured using RH1.

In Figure 4.1, the data at RH1 in blue, is compared against the calculated value using the ideal gas law. The mean difference between the two graphs is 2.84% RH, which is more than the 1.5% RH error of the sensors.

During other experiments it was found that the relative humidity sensor in almost every experiment showed a value that was too high compared to the numerical values calculated using the ideal gas law. This might be caused by the fact that the RH sensors are only measuring the amount of water particles and the temperature. Therefore, when pressure is about 1.5 bar (see Table 2.3), moist will be compressed when assuming it behaves as an ideal gas. This might cause the difference between the two lines. However, this is likely a small deviation, due to the fact that the calculated RH already includes the increased total pressure (p_{tot}, causing an increase in water vapor pressure and therefore an increase in RH, see equation 2.16).

The most likely reason for the higher measured RH, compared to the calculated RH, is caused by the assumption that the air at inlet is dry. This is shown in experiments where there is no water flow. In this experiment, the LFC was zet to 0 so only air directly from the pressure grid could flow through the setup.

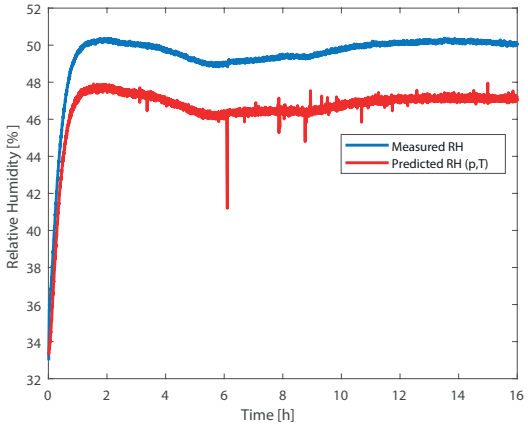

Figure 4.1: Relative humidity as it is calculated using the ideal gas law (red line, calculated using Equation 2.16 and Equation 2.14 using T_RH1 as temperature and $AP1$-$RP1$ as pressure) , and as it is measured using the RH-sensor (blue line). Measurement taken from hydration experiment 9 (air flow of 75 g/min; water flow of 17 g/h). CEM has no setpoint.

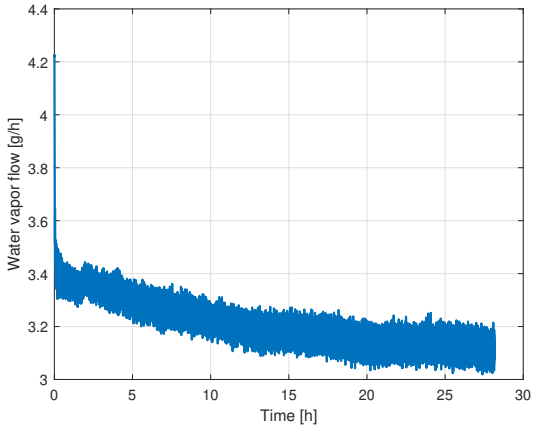

Figure 4.2: Water content converted to water flow in gram per hour of the dry air. The water flow at the LFC is set to 0 g/h and the air flow from the GFC is set to 100 g/min. The water flow is calculated using humidity measured at RH1.

In Figure 4.2, it can be seen that the water content in a dry flow is between 3.5 an 4 gram/hour, which is equal to a mixing ratio of 0.0004 [kg/kg], or 2% RH (at 25 °C and atmospheric pressure). This is definitely significant, and when taking this water content into account the RH can be predicted relatively well. For experiments 3, 4, 8 and 9 the results of RH1 are compared to the RH value calculated with the ideal gas law. The average error was 0.31% RH with the highest error being 0.51% RH. An example is seen in the figure below.

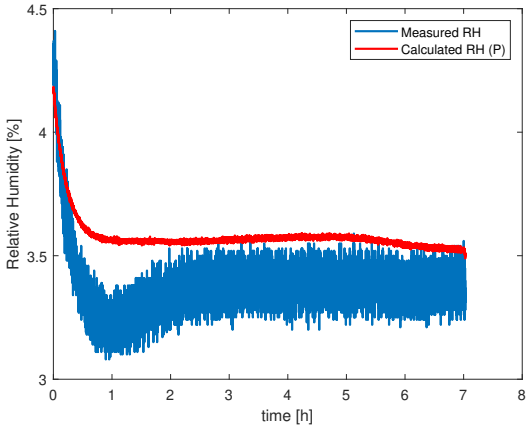

Figure 4.3: Comparison between calculated RH using a water content of 0.0004 [kg/kg] and measured values of RH1 for experiment 9. The LFC is set to 0 g/h, and the GFC is set to 100 g/min. The CEM is set to no setpoint. The mean error between the calculated and measured value is 0.19% RH.

Assuming a water content in dry air equal to 2.0% RH (at 25 °C and 1 bar) gives results that are within margin of error of the RH sensors for all experiments. Therefore this value is taken into account in the determination of the inlet concentration.

In order to get to the inlet concentration, the equation for the mixing ratio has to be altered. The water content in dry air will be described as ζ_a (0.0004 kg/kg).

$$\zeta = \frac{\dot{m}_w}{\dot{m}_a} \cdot (\zeta_a + 1) + \dot{m}_a \cdot \zeta_a \tag{4.1}$$

Where $\dot{m}_w$ is the set water flow in the LFC [kg/s] and $\dot{m}_a$ is the set air flow in the GFC [kg/s]. The newly determined mixing ratio from Equation 4.1 is used in Equation 2.16 to determine the water vapor pressure at the inlet for modelling.

The mixing ratio is a useful parameter when calculating vapor pressures at different locations. Due to the equal density scaling of water vapor and air it is not depending on pressure or temperature. With the mixing ratio known, the water vapor pressure can be calculated at every location in the system using Equation 2.16.

4.2 Temperature during hydration

In this section the results for the hydration of zeolite are shown. First, the reactor is filled with 650 g of Zeolite 13X. Then the material is dehydrated at a temperature of 180 °C for 8 hours to ensure that the zeolite is dry. After dehydration the material is cooled down for 15 minutes with a flow that goes from 180 °C to ambient with steps of 12 °C/min. Then the material cools inside the reactor without flow (natural cooling), see Figure 2.11. Then the measurement is started by creating moist flow with conditions seen in Tables 2.6 and 2.7. Temperatures inside the reactor are measured via the thermocouples seen in Figure 2.7. A typical hydration profile using the thermocouples at the inlet, outlet and center of the packed bed (T_{in}, T_{out}, T_1, T_2 and T_3 respectively) is shown in Figure 4.4.

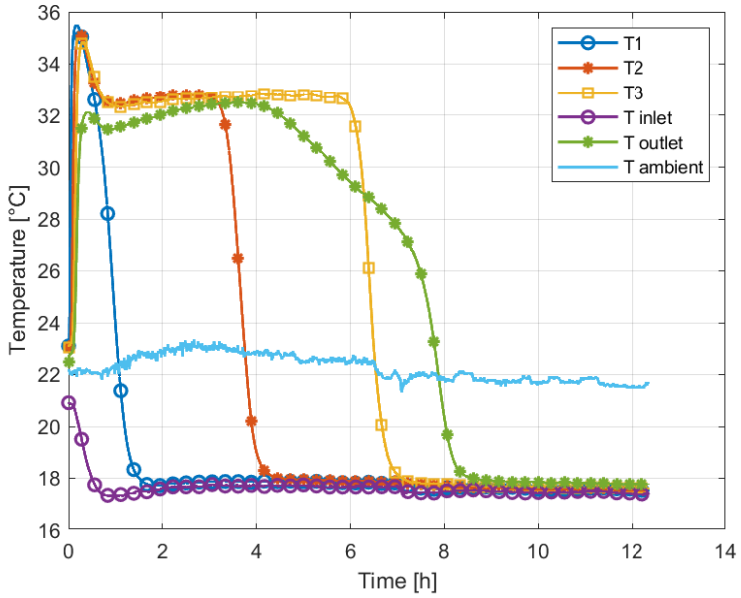

Figure 4.4: Temperature profile for the thermocouples inside the reactor for experiment 2 (97 g/min air and 22 g/h water).

As soon as hydration starts, the inlet temperature drops. This is caused by the water evaporation taking place in the mixer. This takes energy therefore causes a temperature drop. At the beginning of hydration the packed bed temperature rises to a peak of 35 °C. After all material above T1 is saturated, it stops adsorping water, and also stops releasing heat. Then the temperature at the highest thermocouple (T1) drops to inlet temperature. Then the material in center saturates and the temperatrue at T2 drops. After approximately 6.5 hours all material above T3 is saturated and the temperature at T3 drops to inlet temperature as well.

4.2.1 Influence of the flow rate on thermal response

Thermal response is defined as the time it takes before the outlet of the reactor reaches a certain temperature jump. For this thesis the thermal response is arbitrarily determined as the time it takes to reach an outlet temperature that is 10 °C higher than inlet temperature. In order to see the influence of the flow rate on the thermal response of the system, the experiments mentioned in Table 2.6 have been conducted. This set of experiments has the same mixing ratio between air and water, meaning that an increase in air flow is going along with the same relative increase in water flow. Results are shown by subtracting the measured inlet temperature from the outlet temperature, T_{in} and T_{out} as seen in Figure 2.7.

What can be observed from Figure 4.5 is that a higher mass flow rate, and therefore a higher velocity

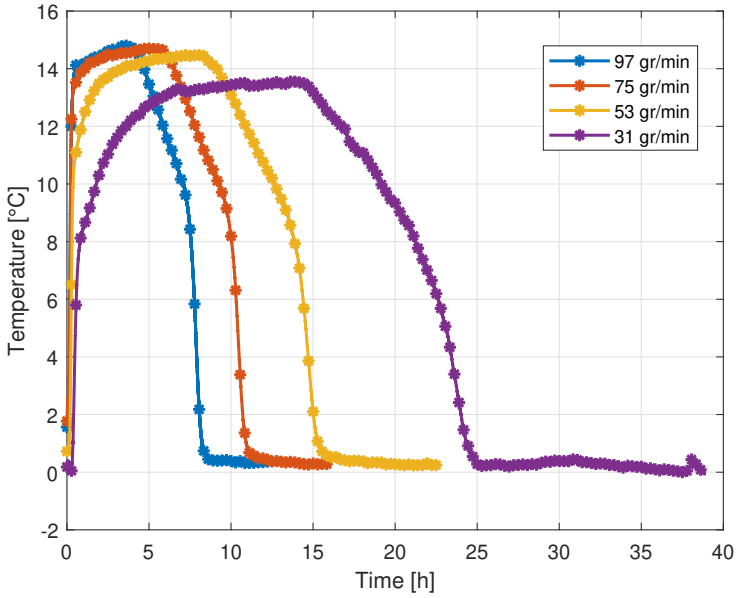

Figure 4.5: The effective temperature increase caused by the Zeolite. This is calculated by taking the temperature difference between the outlet and inlet of the reactor from the continuous data. All experiments are conducted with the same mixing ratio of 0.0038 kg/kg.

through the packed bed, cause the Zeolite to discharge in a shorter time. As the air flow gets higher, also the water flow gets higher, causing the zeolite to discharge faster. The temperature increase stays the same, and all water is adsorped during the period of maximum temperature increase. Following from Equation 2.23, that means that the maximum power output scales with the total flow. From Figure 4.5 it is concluded that a two times higher flow, with equal humidity, ensures a power output that is twice as high in this reactor. Similarly, increasing the flow rate with a factor two, keeping the same humidity, correlates with a total adsorption time that is twice as short.

When looking at the thermal response of the system, the most important parameter is the time it takes for the outlet flow to get to a certain threshold. This threshold is arbitrary and chosen to be a temperature increase of 10 °C.

In Figure 4.6, it is observed that the difference between the inlet and outlet temperature is not zero at the beginning of hydration for three out of four experiments. This is caused by the ambient temperature being higher than the reactor inlet temperature. Due to the CEM heat exchanger being set to zero for these experiments, water evaporation energy causes a temperature drop over time until thermal equilibrium between the moist air, pipes and ambient is reached. This observation can also be seen in Figure 4.4.

The quantified thermal response is shown in the Table 4.1.

Table 4.1: Table containing the first moment a delta T of 10 °C is seen for different experiments.

Air flow [g/min]	Time
31	6435 s (107.3 min)
53	1345 s (22.4 min)
75	818 s (13.6 min)
97	788 s (13.1 min)

For these experiments, after an air flow of 75 g/min, the influence on thermal response is small. An air flow of 31 g/min takes the longest to reach the setpoint, while it is able to maintain the temperature increas over a longer period of time, see Figure 4.5.

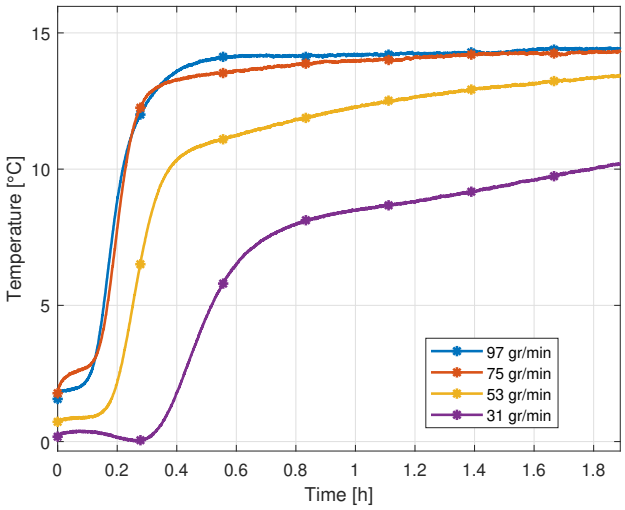

Figure 4.6: Zoom to the first 1.8 hours of different hydration experiments that use the same mixing ratio of 0.00038 kg/kg.

4.2.2 Influence of humidity on the thermal response

In order to see the influence of the humidity, several experiments are conducted using the same flowrate, but using different mixing ratio's. The flowrate was set to 75 g/min, and the CEM and heater are turned off during hydration. The set of inlet conditions is found in Table 2.7.

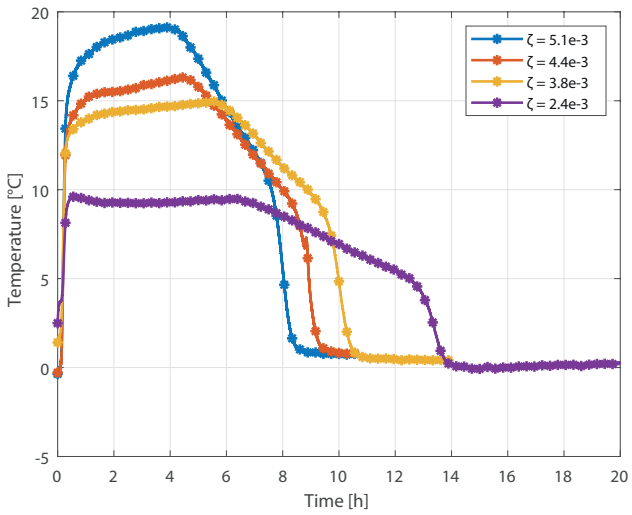

Figure 4.7: Temperature increase for different mixing ratios during hydration experiments. CEM and heater temperature are set to no setpoint, GFC is set to 75 g/min. A higher value of the mixing ratio ζ is equal to a higher humidity.

The experiments are all conducted with the CEM and heater turned off, and the air flow was equal to 75 g/min for all experiments. The difference is seen in the mixing ratio, where a higher value for the mixing ratio is equal to a higher humidity. As seen in Figure 4.7, an increase in humidity causes an increase in temperature jump. At higher humidity, there is a larger driving force because of a larger gradient in vapor pressure between a particle and its surrounding air. This causes the Zeolite to become saturated faster, which leads to shorter hydration times.

To see the influence of humidity on the thermal response a zoom of Figure 4.7 is created.

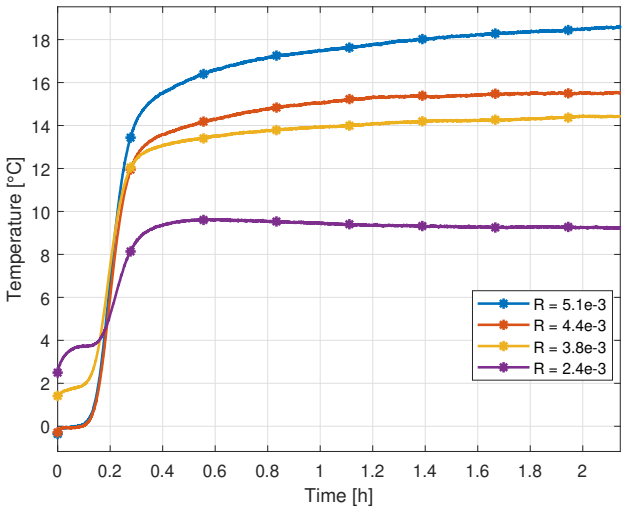

Figure 4.8: Zoom into the first two hours for the same experiments seen in Figure 4.7.

As seen in Figure 4.8, for some experiments the ambient temperature at the start of the experiment was higher than the inlet temperature of the carrier gas. However, after 5 minutes, the complete packed bed is hotter than ambient temperature, and only during the first 5 minutes discrepancies are seen. The effect on total power output is insignificant. When disregarding the lowest mixing ratio, all three sets of follow a similar trend towards their peak temperature. The ramp-up is almost identical for the experiments with different mixing ratios but equal flows. This can also be seen when comparing the time it takes to reach the threshold of 10 °C, see Table 4.2.

Table 4.2: Table containing the first moment a delta T of 10 °C is measured for experiments where only the water flow rate is changed and the air flow is set to 75 g/min.

Water flow [g/h]	Time
11 (ζ=2.4E-3)	Did not reach 10 °C
17 (ζ=3.8E-3)	834 s (13.7 min)
20 (ζ=4.4E-3)	872 s (14.5 min)
23 (ζ=5.1E-3)	822 s (13.9 min)

As the lowest water flow did not reach the threshold of 10 °C, it is not taken into account in the table. There appears to be no direct correlation between humidity and thermal response. However, an increase in humidity leads to an increased temperature jump.

4.2.3 Ideal conditions for maximum power

Ideal conditions are dependent on the use case. When maximum temperature increase is needed, a high vapor pressure is preferable, which is seen in Figure 4.7. Following from Equation 2.14, warm air can hold more water than cold air. When needing a temperature jump larger then 20 °C, pre-heating the inflow might be necessary to prevent condensation. Experiment 11 (GFC set to 75 g/min, LFC set to 23 g/h, no CEM heating) is used as the reference for maximum temperature output.

Another use case could be maximum power. Then, the flowspeed needs to be as high as possible. As the power output has a linear relationship with air flow (Equation 2.23), an experiment has been conducted that delivers the maximum output power of the reactor. Due to instability of the temperature control, this experiment is conducted without use of the CEM. This is experiment 6 in Table 2.7, meaning an air flow of 97 g/min is used, along a water flow of 25 g/h. Experiment 6 (maximum power) and 11 (maximum temperature increase) are compared in Figures 4.9 and 4.10.

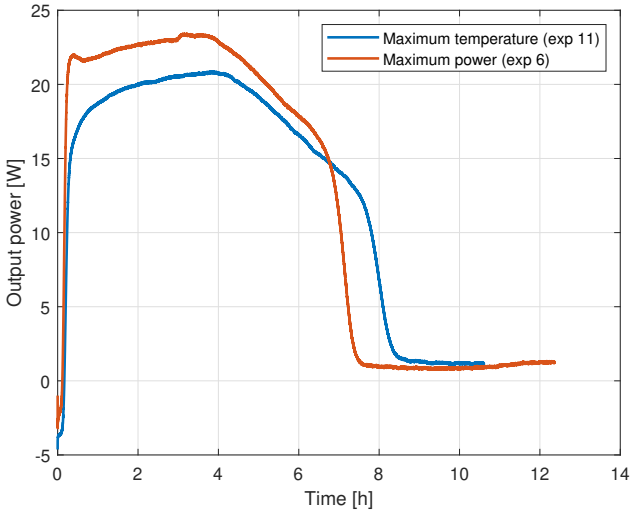

Figure 4.9: Output power of experiment 11 (air flow is 75 g/min, water flow is 23 g/h), compared to the output power of experiment 6 (air flow is 97 g/min, water flow is 25 g/h). Power output for both experiments is calculated using Equation 2.23.

As seen in Figure 4.9, the maximum output power is seen in the experiment where it was expected. This output power is equal to 23.5 W. The mass flow of experiment 6 (orange line) is 25% higher, while the maximum output power is 12% higher. This is caused by the higher humidity of experiment 11 (blue line), which is also seen when comparing the maximum temperature reached. As seen in Figure 4.10, this does not mean that the temperature increase is also higher. As seen in Equation 3.20, the adsorption enthalpy is only slightly dependent on temperature (q_{eq} depends on the temperature). Therefore, a longer residence time in the reactor is expected to lead to a higher temperature. However, this relation is not seen in Figure 4.5.

4.3 Total energy storage capacity

The total energy storage capacity is calculated by integrating the power output over time (Equation 2.23) by using the $trapz$ function in MATLAB. This means that only the power of the flow is of interest for the total amount of stored energy. Heat losses through the wall are not determined due to the temperature difference between the thermocouples TW and TI is too small. However, indirectly they are taken into account as the output power becomes lower when heat losses get higher.

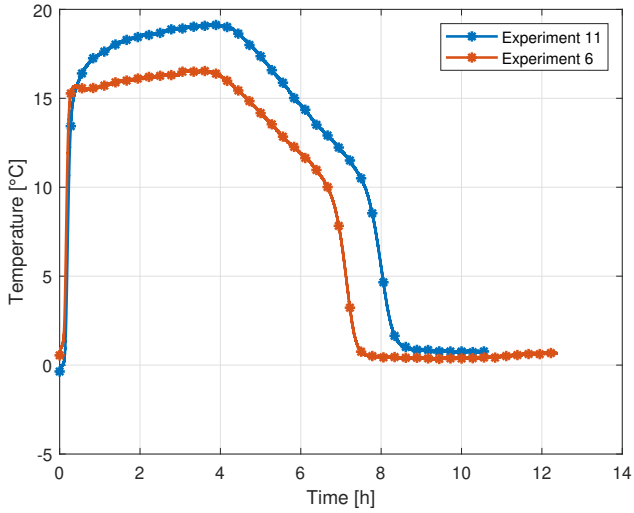

Figure 4.10: Temperature increase in the reactor, showed for experiment 6 and 11

The amount of stored energy is determined by integration of the output power for all conducted experiments. It is expected that all stored energy is approximately the same, as the heat during hydration relatively low (below 40 °C), and the reactor is really well insulated. When looking at experiments 8 to 11 (same air flow set at GFC, different humidities by increasing the water flow rate, see Table 2.7) the following result is seen:

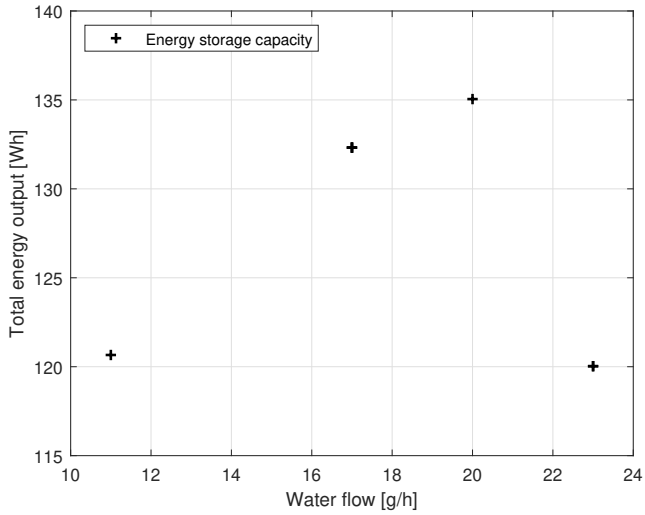

Figure 4.11: Experimentally determined energy storage capacities for experiments 8 through 11 (different humidities by increasing the water flow rate). The air flow for all experiments is equal to 75 g/min.

The results do show a larger spread than expected. The increase in total energy from low to high water flow can be explained by the fact that these experiments last shorter. This means that heat loss is less prominent when humidity gets higher. However, the results of the highest humidity (23 g/h in Figure 4.11) does not stroke with this result.

The theoretical energy storage capacity of the 650 g of zeolite is:

$$E_{zeolite} = \Delta H_{mean} \cdot (q_{sat} - q_0) \cdot m_{s,dry} = 65000 \cdot (17 - 3.5) \cdot 0.65 = 570.4kJ = 158.4Wh \quad (4.2)$$

Where ΔH_{mean} is the mean enthalpy from Figure 3.2, and taken as 65 kJ/mol. $m_{s,dry}$ is the dry mass

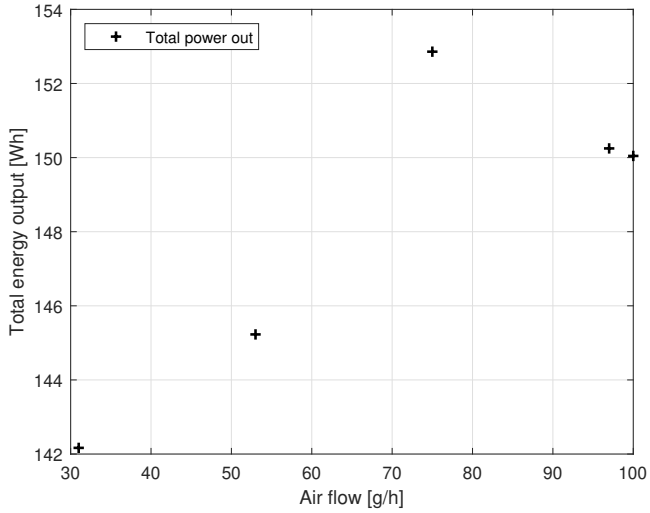

Figure 4.12: Difference in energy storage capacity for different flowrates, but constant humidity.

of the Zeolite, which is equal to 650 g. All results shown in Figure 4.11 are well below the theoretical energy, which can be accounted for by heat losses through the wall.

The energy capacity is also compared against different flowspeeds, this is shown in Figure 4.12. For these experiments, the flow rate is changed, but the humidity is kept the same, see Table 2.6.

The spread is still noticed but the deviations are not as large when comparing to Figure 4.11. A possible cause might be that Figure 4.11 contains data from experiments where during rest a flow was sent through the reactor. The results displayed in Figure 4.12, however, were obtained by letting the reactor cool down naturally and closing the valves to close the reactor in and outlet. The results still show a spread and therefore an influence of flow rate or humidity on the total energy output is not found.

4.4 Model results for Zeolite as TCM

In this section, the results of the COMSOL model are shown. First the results of the velocity profile are discussed, after which the influence of the initial loading is shown. Next a dehydration experiment is compared to the numerical model, after which a hydration experiment is compared to the model. Lastly, the influence of inlet temperature is shown.

4.4.1 Velocity profile

Using the described method in Section 3.1, a velocity profile for the radial direction is calculated by creating a 1D model in COMSOL. The mesh element size is set to 3.5 E-5 m and discretization is done using a linear Lagrange shape function. Equation 3.4 is solved using a stationary solver (MUMPS). By solving this PDE, a radial velocity profile that takes into account wall channeling is created. Figure 4.13 shows the velocity profile for the model with an air flow of 100 g/min and a water flow of 17 g/h (Experiment 9 in Table 2.7. The near wall effect of the porosity function (Equation 3.3) is clearly seen in the velocity profile in Figure . The lower porosity causes a higher velocity, while at the wall itself, the no-slip boundary condition is seen. In Figure 4.13, the velocity profile in the near wall region is shown

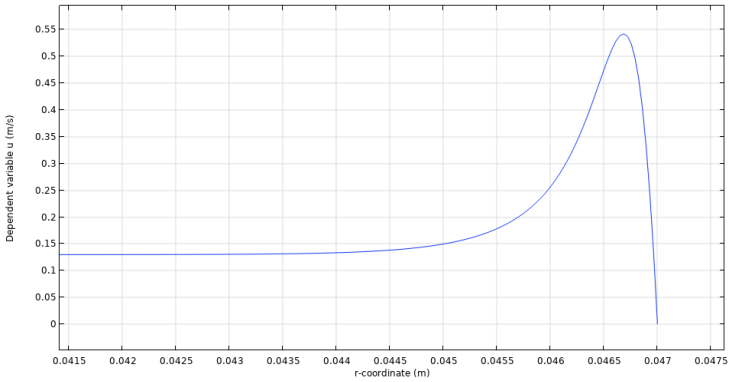

Figure 4.13: Modelled velocity profile in the near wall region.

(wall is at r = 0.047 m). Not shown in this figure is the velocity profile in the center of the packed bed (r = 0 m). However, this is equal to the velocity at r= 0.0415 in Figure 4.13, which is 0.13 m/s. This velocity profile is used for any further modelling with Zeolite.

4.4.2 Dehydration

Before every experiment, the Zeolite is dried for 8 hours with an air flow of 100 g/min, and a heater temperature of 180 °C. This results in a temperature of 120 °C at the reactor inlet. This dehydration cycle is kept consistent to allow for an equal initial loading (kg of water per kg of Zeolite) for every hydration experiment.

The equilibrium loading can be determined when the water vapor pressure is known using Equation 2.18. Expected is that after the Zeolite is saturated, all the Zeolite inside the reactor is at this equilibrium loading. By implementing this water vapor pressure in Equation 2.18, the saturation loading is determined.

First, the relative humidity and temperature data from RH1 is taken and by using Equation 2.13 and 2.14, the water vapor pressure at RH1 is determined:

$$p_v@RH1 = \frac{RH1 \cdot T(@RH1)}{100} \tag{4.3}$$

The water vapor pressure at the inlet of the reactor is determined by using the assumption that the mixing ratio ζ is equal throughout the inlet tubing. At fully saturated material the mixing ratio is equal throughout the entire system. The water vapor pressure at the reactor inlet is calculated as follows:

$$p_v@Reactor_{in} = p_v@RH1 \cdot \frac{AP2}{AP1 - RP1} \tag{4.4}$$

Where $AP2$ is the pressure at the inlet of the reactor, and $AP1$-$RP1$ is the pressure at RH1, both in [bar]. During hydration of Experiment 9, this water vapor pressure is found to be 801 Pa with an maximum uncertainty of 33 Pa. Using this water vapor pressure, the equilibrium loading is calculated to be using 2.18 and is equal to 16.95 mol/kg.

The value of initial loading can be found using load cell data of dehydration experiments, by converting the measured weight loss to loading. This is done as follows:

$$\Delta q = \frac{\Delta m(LC)}{m_z \cdot M_w} \tag{4.5}$$

Here $\Delta m(LC)$ is the measured weight difference using the load cell (154 g for Experiment 9), M_w is the molar mass of water and m_z is the amount of Zeolite inside the reactor (650 g). This gives a Δq of 13 mol/kg. In a similar manner, the difference loading can be calculated by determining the equilibrium loading at dehydration conditions. Inlet conditions are shown in Table 4.3. q_{eq} at dehydration conditions is equal to 3.65 [mol/kg]. This is the theoretical value of q_0 for hydration modelling.

Hydration/Dehydration	Water vapor pressure	average inlet temperature (@ t = 6 hours)
Hydration (cycle 9)	801 Pa	21 °C
Dehydration (cycle 9)	85 Pa	123 °C

Table 4.3: Water vapor pressure at the reactor inlet and inlet temperature compared for the hydration and dehydration of cycle 9.

The loading difference is measured using the load cell, and calculated using Equation 4.5. The load cell is extremely sensitive to environmental influences, (e.g. movement, bumping the table etc.). Besides measuring the weight difference using the load cell, the weight difference can also be estimated using the RH sensors. To make sure the inlet loading is correct, data from four other experiments is used as well.

For dehydration of experiments 2, 3, 4 and 11 (see Table 2.6 and 2.7 for the set conditions), Equation 4.4 is used to calculate the water vapor pressure at the inlet of the reactor. Using this water vapor pressure,

the mixing ratio can be found by rewriting Equation 2.16. By multiplying the mixing ratio with the carrier gas flow, the inlet water flow is known. In a similar way, the water vapor pressure at the outlet is calculated using the temperature and RH data from RH2 following Equation 4.3. Again by rewriting water vapor pressure to mixing ratio and multiplying that value with the carrier gas flow (known from the GFC), the water flow at the outlet is determined. By subtracting the water inflow from the outflow, and by using a cumulative integration function ($cumtrapz$) in MATLAB, the total mass difference is found for four different experiments. The results are compared to the mass difference measured with the load cell in Table 4.4.

Table 4.4: Weight difference during dehydration using load cell and RH sensors for determination.

Experiment (air flow [g/min]/water flow[g/h])	Load cell [g]	RH sensors [g]
2 (75/17)	250	161
3 (53/12)	206	158
4 (31/7)	105	157
11 (75/20)	143	154

As dehydration is performed in the same way after saturated hydration, the results of the weight loss should approximately be the same. As can be seen in Table 4.4, the load cell measures a high variety in weight losses, while the RH sensors show a more consistent result. The results of the load cell are not consistent at all. This is likely caused by the fact that the pressure drop over the glass filters depends on the volume flow rate, see Figure 2.4, and as the inlet air heats up, the air volume flow rate changes significantly.

As the RH sensors show a more consistent result, the amount of desorbed water that is used is set to 157 gram. This results in an average loading of 3.5 mol/kg after dehydration, which is in line with the theoretical value that was expected. As this average loading is determined using the RH sensors before the inlet, and after the outlet, the actual loading gradient in the reactor is unknown, and therefore set to zero. This implies an initial loading of 3.5 mol/kg at every node in the packed bed model.

The modelling of dehydration can be used to see if the material parameters that make up the heat resistance are determined correctly. The results of the center temperature (T), near wall temperature at the inside (TI) and the wall temperature between the isolation and stainless steel (TW) are shown in Figures 4.15 4.14, 4.16 and respectively.

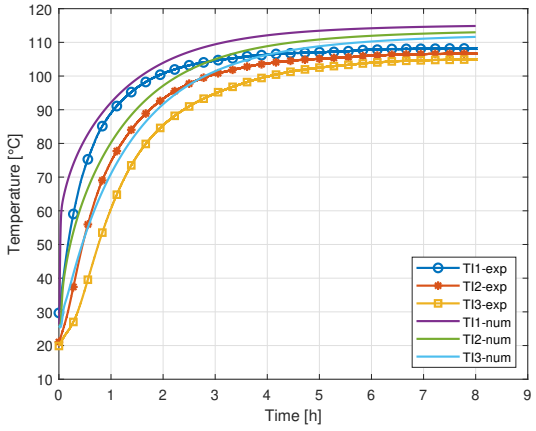

Figure 4.14: Temperature profile over time during dehydration at the inside of the wall

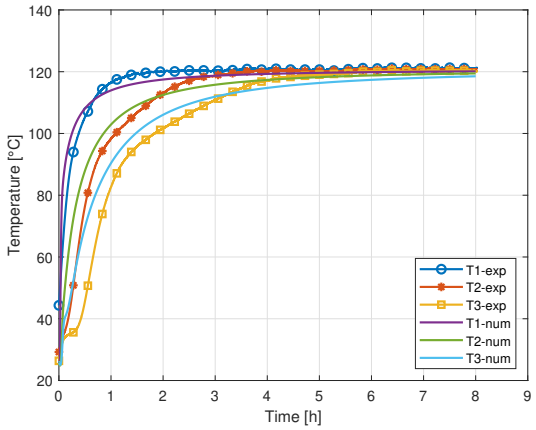

Figure 4.15: Temperature profile over time during dehydration in the center of the packed bed.

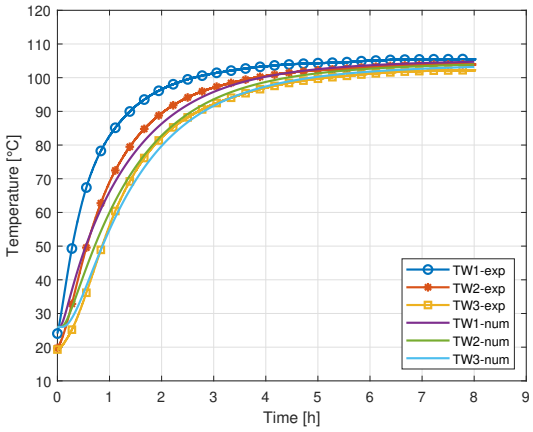

Figure 4.16: Temperature profile over time during dehydration at the outside of the wall

Figure 4.15 shows the temperature during dehydration in the center of the packed bed. For T1 (thermocouple 1), the model seems to be determining the temperature really well. For T2 and T3, the model overestimates the steepness of the increase in temperature for the first hour, while the model underestimates all three thermocouples by a margin of 1.5 °C on average near the end of the simulation. This can be seen in Figure 4.18. Figure 4.14 shows the temperatures just inside the reactor at three different heights ($TI1$, $TI2$, $TI3$ in Figure 2.7). Here, for all three thermocouples, the model overestimates the temperature for the entire duration of the simulation. This might be due to an overestimation of the near wall porosity. That causes the velocity near the wall to be higher than in the center of the packed bed, see Figure 4.13. However, it might also be due to flow uniformity being imperfect during the experiments. For the model, the flow is assumed to be uniform.

Figure 4.16 shows the comparison between experiment and simulation for temperature profiles of $TW1$, $TW2$ and $TW3$ (For locations see Figure 2.7). Here the model underestimates the steepness of the increase in temperature for the first 3 hours, after which the model has an error of just within the 1°C range of the thermocouples.

Zooms of the last hour of the dehydration have been made to show a more quantifiable result. Figure 4.17 shows the temperature near the inside wall of the reactor is over estimated by about 5 °C by the model, while the error for the outside wall lies around 1 to 3 °C. Figure 4.18 shows the temperature profile in the center of the packed bed for the last hour. Here the error is between 1 and 2.5 °C, depending on the thermocouple position. A possible reason for the large deviation in the last hour when looking at the inside wall temperatures (Figure 4.17), might be the velocity profile that is modelled. As mentioned before, uniformity of the flow is assumed, while the actual velocity profile is likely not uniform. This needs further investigation to be certain. All the mean differences between the model and experiment are shown in Table 4.5.

Table 4.5: Mean difference between the model and thermocouples during hydration experiment. Negative value means the model overestimates the temperature, positive value means the model underestimates the temperature.

Thermocouple	Mean difference [°C] total	Mean difference last hour
TW1	5.59	1.22
TW2	2.76	0.44
TW3	-0.13	-0.64
TI1	-5.98	-6.42
TI2	-5.96	-5.98
TI3	-7.35	-6.33
T1	0.98	1.22
T2	0.03	1.77
T3	-1.40	2.44

As seen in Table 4.5, the mean error for a lot of thermocouples is just outside of the measurement error range of the thermocouples (1 °C). As mentioned before, this might be caused by the unknown flow distribution inside the packed bed. Another aspect that is worth noting, is that the conductivity of the exhaust wrap is calculated using experiments in Section 2.3. This allows for room for error, as the exact value of the conductivity is not known. However, the heat resistance of the exhaust wrap counts for approximately 5 % of the total heat resistance, as most heat resistance is caused by the insulation.

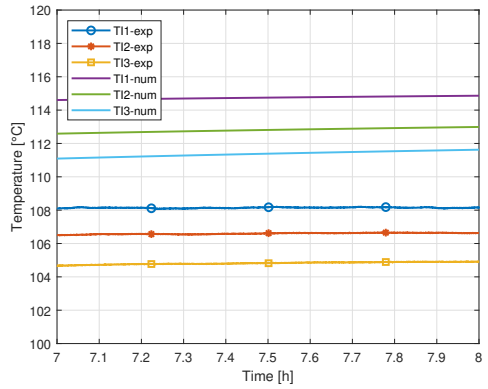

Figure 4.17: Temperature profile of last hour during dehydration at the inside of the wall.

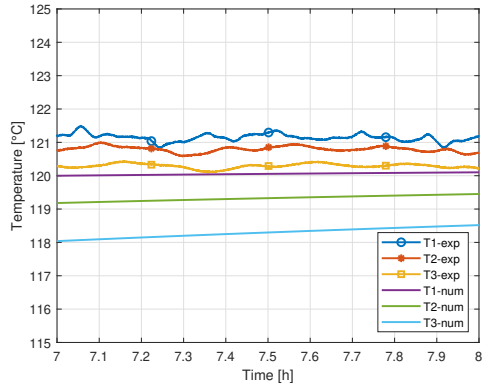

Figure 4.18: Temperature profile of last hour during dehydration in the center of the packed bed.

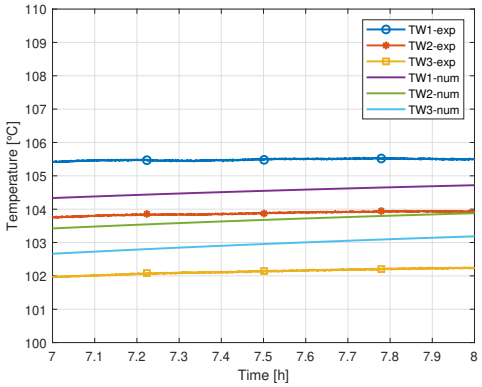

Figure 4.19: Temperature profile of last hour during dehydration at the outside of the wall.

4.4.3 Hydration

In this subsection, the model that uses Zeolite as TCM is used for modeling hydration. The model is validated by comparing it to Experiment 2. A comparison between the model and measurements is made by using the thermocouples inside the packed bed. Then the modelled outlet concentration is compared to the concentration determined in the experiment. The full set of modelling conditions can be seen in Table 4.6. Experimental data for the ambient temperature and inlet temperature is loaded into the model to reduce distortion between the model and measurements caused by environmental changes.

Table 4.6: Input parameters for Zeolite model for hydration.

Property	Value [unit]
Bed porosity (ϵ_b)	0.4[-]
particle density (ρ_p)	1150 [kg/m^3]
particle heat capacity ($C_{p,s}$)	880 [J/kg·K)]
particle thermal conductivity (λ_s)	0.4 [W/m K]
Mass flow rate ($\dot{m}$)	75 [g/min]
Air flow rate (ϕ)	8.6 E-4 [m^3/s]
Inlet concentration (c_{in})	0.326 [mol/m^3]
Initial loading (q_0)	3.5 [mol/kg]

When visualizing the model, three different parameters are interesting to look at. The temperature of the air flow (T), the concentration of the air flow (c), and the water loading of the Zeolite (q). Figure 4.20 shows an example of such a visualization at t=4 hours. What can be seen is that as the concentration has a real sharp front, which is similar to the water loading. This means that only a small band of Zeolite is adsorping water (the light red to light blue area). This reaction front moves downwards (air comes in from the top). As soon as the Zeolite is saturated, the front moves further down. Above the reaction front no energy is released, as particles are saturated. This results in the temperature behind the reaction front being the same as the temperature at the humid inlet. The reaction front can be visually seen in the model (Figure 4.20), while being visible at the experiments by making use of the three different heights of the thermocouples (Figure 4.21). The temperatures that are measured at the different thermocouple

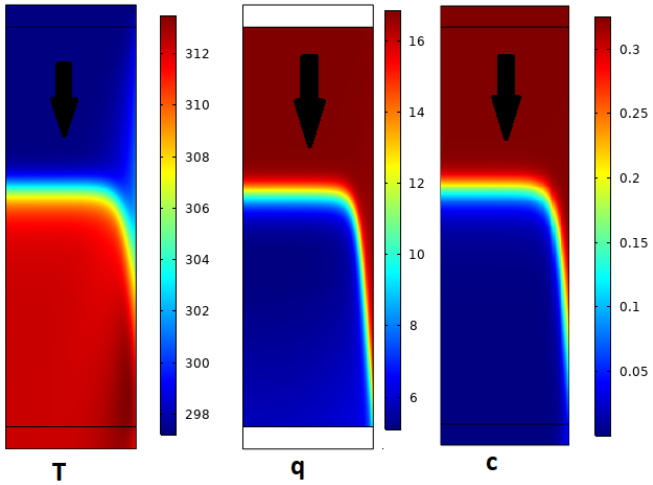

Figure 4.20: Reaction front in the reactor at t = 4 hours. On the left, the temperature front in the air (and TCM, as local thermal equillibrium is assumed) is seen. The center plot shows the water loading in [mol/kg] of the Zeolite, and the plot on the right shows the water concentration in the air [mol/m^3].

locations are also simulated. They are shown in Figure 4.21.

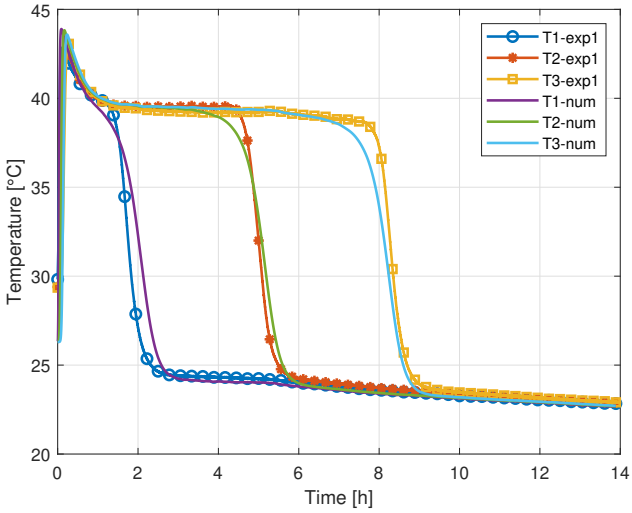

Figure 4.21: Experimental values of the three thermocouples in the center of the packed bed compared to the numerical model during a hydration experiment.

In Figure 4.21, the temperature profile of the numerical model is compared to Experiment 2. The comparison is made for the thermocouples at the center of the packed bed ($T1$, $T2$ and $T3$ in Figure 2.7). The reaction front is here seen as well. As soon as the Zeolite above a thermocouple is saturated, no energy is released any more and the temperature drops to inlet temperatures. The gradient of the steep part from high to low temperatures is dependent on the heat capacity of the Zeolite. The results show great resemblance.

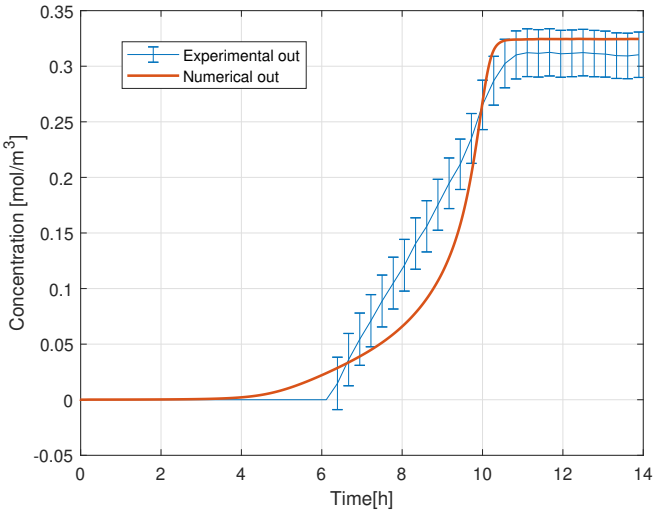

Figure 4.22: Experimental values of the outgoing concentration compared to the numerically calculated concentration at the outlet. Experimental values have errorbars according to uncertainties given by manufacturers.

Figure 4.22 shows the concentration modelling versus the measured value at the outlet using RH2. The data from RH2 is rewritten to water vapor pressure using Equation 2.13 and to concentration by using 2.17. The model starts releasing water earlier than reality shows. This is again an indication that the flow profile is not stroking with reality. As seen in Figure 4.20, the near wall region is fully saturated earlier than the center of the packed bed, while in reality this is likely not the case. However, the time at which full saturation is reached is approximately the same.

The highest outlet concentration for the numerical model is higher than the numerically found value. However, due to the uncertainty of the used equipement, the result is still within the margin of error. Therefore the numerical model is validated as a good representation of reality.

4.4.4 Influence of input temperature

The model is used to find the influence of the inlet temperature on the output power of the system. When using Zeolite 13X, the adsorption enthalpy is only depending on the water loading of the system, see Equation 3.20. Therefore, because the source term in the heat balance equation 3.10 is almost independent of temperature. This leads to the expectation that the temperature increase in the packed bed is independent of the inlet temperature. However, when looking at the maximum equilibrium loading, see Figure 2.10, the maximum equilibrium loading decreases when the temperature increases.

In order to test the hypothesis, a sensitivity analysis is performed by using the auxillary sweep function in the COMSOL model. The starting inlet temperature is 20 °C, and after each simulation is done, it is incrementally increased (+5, +10, +15 and +20 °C). The influence is seen on the output power. Because output power is dependent on the temperature difference between inlet and outlet 2.23, it is a good indicator for efficiency. The output power is determined in COMSOL using Equation 2.23.

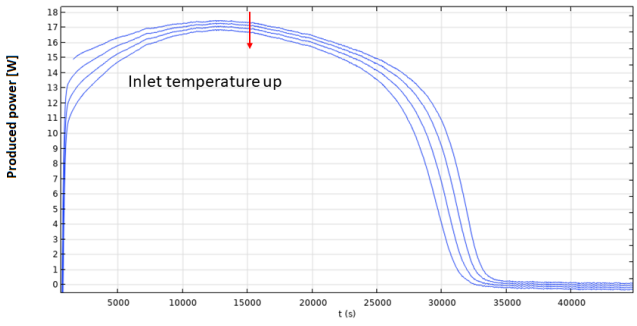

Figure 4.23: Influence of inlet temperature on the output power. The inlet temperature is incrementally increased with +5, +10, +15 and +20 °C.

In Figure 4.23, two results are immediately noticeable. The first is that the maximum power output goes down when the inlet temperature goes up. This can be explained by the fact that a higher inlet temperature means a higher temperature gradient with ambient, and therefore the losses will be higher.

The second observation that can be made from Figure 4.23 is that for hydration an increase in inlet temperature leads to a decrease in the maximum loading. This is caused by the fact that the equilibrium loading goes down as the temperature goes up, see Figure 2.18. This also results in the packed bed reaching saturated state earlier. Therefore, if one wants to release the maximum amount of energy, a low inlet temperature is recommended.

5 | Potassium carbonate theory

While Zeolite is a useful material for storage, the energy density is relatively low, and salt hydrates are more promising when it comes to energy density [56]. A promising salt hydrate in particular is potassium carbonate (K_2CO_3), due to the low cost and high energy density of 1.3 GJ/m^3 compared to an energy density of 0.92 GJ/m^3 for Zeolite [20]. The Zeolite experiments are used for testing the system. Now the reactor is filled with potassium carbonate and cyclic experiments are conducted for K_2CO_3. In this chapter, the material properties of K_2CO_3 found in literature are discussed, after which the experimental plan is shown. Lastly, the adaptations from the adsorption process of Zeolite to the chemical reaction of K_2CO_3 and H_2O in the numerical model are discussed.

5.1 Material properties of K_2CO_3

Control over the water concentration of the inflow is a necessity in order to prevent deliquescence when using K_2CO_3. Deliquescence is the process by which a substance absorbs moisture from the atmosphere until it dissolves in the absorbed water and forms a solution. According to Encyclopedia Brittanica, all soluble salts will deliquesce if the air is sufficiently humid [57]. Despite the risk of the material becoming a solution, there is another reason why deliquescent conditions needs to be prevented. Cycling of the material causes micro-pores to form. These micro pores improve the absorption process. However, if the water vapor pressure becomes too large, the material goes into deliquescence. This causes the aforementioned micro-pores to fill up with crystal water. Dehydration then causes the material to become a non-porous structure. This reduces water transport, and therefore the hydration rate of the salt hydrate [58]. Figure 5.1 shows the operating conditions of the K_2CO_3 in a phase diagram.

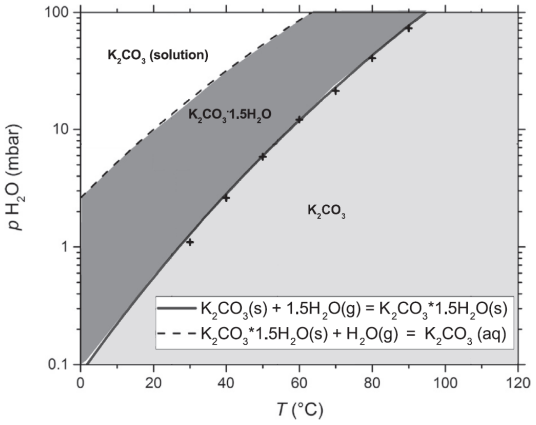

Figure 5.1: Different phases of potassium carbonate depending on the temperature and water vapor pressure. Dehydrated K_2CO_3 is found when the conditions are within the light grey area (on the right side). Hydrated K_2CO_3 is seen in the dark grey part. Deliquescence occurs in the white area [11].

The chemical reaction of water absorption by potassium carbonate is shown below:

$$K_2CO_3(s) + H_2O\,(g) \iff K_2CO_3 \cdot 1.5H_2O(s) \tag{5.1}$$

Figure 5.1 shows the state of potassium carbonate for different (p,T) conditions of the surroundings. When the conditions inside the reactor are in the dark grey area of Figure 5.1, the hydration reaction from left to right takes place. During dehydration, the reaction goes from right to left, which occurs in the most right area (light grey), in Figure 5.1. The white area in the top left corner in Figure 5.1 show the conditions at which the salt hydrate goes into deliquescence.

During hydration, water particles are absorbed by the potassium carbonate. This causes the material expand, and because water is less dense than dry potassium carbonate, the density of the sesquihydrate is lower than the density of the dry material. The mass densities of dry and hydrated potassium carbonate are shown in Table 5.1.

Table 5.1: Material values of potassium carbonate in dry and sesquihydrate state [59].

Unit	Sesquihydrate	Dry
Molar mass	M_n 165.23 [g/mol]	M_m 138.21 [g/mol]
Density	$\rho_{p,n}$ 2043 [kg/m^3]	$\rho_{p,m}$ 2290 [kg/m^3]

In Table 5.1, the subscripts m denotes the lowest hydrate (dry) state, which is with 0 mol absorbed water. n stands for the highest hydrate state (sesquihydrate), which is equal to 1.5 mol absorbed water per mol K_2CO_3.

As the potassium carbonate gets hydrated, it expands, causing the material to become less dense. During dehydration the material shrinks again, causing the material to crack (the aforementioned micro-pores). Crack formation is causing the material to become up to 30 % larger after 12 hydration-dehydration cycles [60]. Therefore in this reactor experiment the reactor is filled initially to 81 %, to give the material the option to expand. A filling percentage of 81% is equal to filling to the height of the first thermocouples ($T1$/$TI1$).

5.1.1 Bulk porosity

The assumption is made that before the experiments are started, the material is fully dry, and non porous (particle porosity is equal to zero). The weight of the dry potassium carbonate is measured before insertion in the reactor. Using this weight, the porosity of the packed bed is determined:

$$\epsilon_b = 1 - \frac{\rho_{bulk}}{\rho_{p,m}} \tag{5.2}$$

Where ρ_p is the dry particle density, and ρ_{bulk} is the bulk density, which is found by dividing the weight of all material going into the reactor through the volume it occupies. A picture of the reactor, taken from above, before the first hydration cycle is shown in Figure 5.2.

Thermocouple $T1$ can still be seen in Figure 5.2. This is the small grey piece through the wall on the left of the picture. The bulk density of the potassium carbonate is determined by substracting the total weight of material by the volume that the K_2CO_3 occupies. As can be seen in Figure 5.2, the total bed height is from the lowest glass filter to the height of thermocouple one, which is at a height of 117 mm. Therefore the total volume that the K_2CO_3 occupies is:

$$V_{K_2CO_3} = h * A = 0.117 * \pi * 0.047^2 = 8.12E-4m^3 \tag{5.3}$$

Here A is the horizontal cross sectional area of the reactor, as seen in Figure 5.2. The total weight of K_2CO_3 inside the reactor before the first cycle is 1.06 kg. Assuming a particle porosity of zero, the average bed porosity becomes:

Figure 5.2: Height of the particle bed before the first run

$$\epsilon_b = 1 - \frac{1.06/8.12E - 4}{2290} = 0.43 \tag{5.4}$$

Here the used density of the material is of fully dry potassium carbonate, see Table 5.1.

After cycle 8, the material is weighed again. This time, 1.055 kg of material was still left. The material expansion expected, based on the data of TGA experiments, is about 21% apparent area expansion after cycle 8 [60]. This results in a volumetric expansion of 33%. This is not seen in the reactor. However, after taking material out of the reactor it is seen that some particles formed large agglomerates. When these particles are (manually) separated again, the material did not fit in the reactor. In total 52 g is left out of the reactor. Therefore the porosity is determined again. When assuming 1 kg of material inside of the reactor, the porosity, as calculated with Equation 5.2 is 0.56, which is extremely high and not reasonable. When assuming the particles have a volumetric expansion of 33%, the particle density decreases with 33%. When using this value, the porosity found using Equation 5.2 is 0.43, which is more reasonable. Therefore, a porosity of 0.43 is used for modelling.

5.1.2 Reaction enthalpy and energy density

The reaction enthalpy of hydration of potassium carbonate is 65.8 kJ/mol [60]. Using this reaction enthalpy, the energy density of the system can be calculated. The energy density E/V is defined as follows [20]:

$$(E/V)_{open} = \frac{|\Delta H^0_{m \longrightarrow n}| \cdot (n-m)}{M_n} \rho_{p,n} \tag{5.5}$$

Where m and n are the molar quantities that follow from the hydration reaction, which are 0 and 1.5 respectively for the reaction. M_n is the molar mass of the highest hydrate (1.5) in [kg/mol], and $\rho_{p,n}$ is the density of the highest hydrate in [kg/m^3]. Values are seen in Table 5.1.

Using the values in Table 5.1, and m as 0 and n as 1.5, the energy density of potassium carbonate is determined to be 1.22 GJ/m^3. The material fills approximately 81.5% of the reactor at the first cycle, which is a volume of 0.812 liter. The maximum amount of energy that can be stored in the reactor using potassium carbonate, $E_{K_2CO_3}$, is:

$$E_{K_2CO_3} = (1 - 0.43) \cdot 1.22GJ/m^3 \cdot 8.12E - 4m^3 = 0.565GJ \approx 157Wh \tag{5.6}$$

The maximum amount of water absorped is 207.26 g, see Equation 5.7.

$$m_{v,max} = \frac{m_{tot,m}}{\rho_m} \cdot n \cdot M_v = \frac{1060g}{138.2g/mol} \cdot 1.5mol \cdot 18.01528g/mol = 207.26g \tag{5.7}$$

Here $m_{v,max}$ is the maximum amount of absorbed water in [g], ρ_m is the density of the dry potassium carbonate (see Table 5.1). $m_{tot,m}$ is the amount of dry potassium carbonate, equal to 1.06 kg. n is the molar value of the highest hydrate, which is 1.5, and M_v is the molar mass of water.

5.2 Potassium carbonate model

A continuum model comparable to the one used for Zeolite 13X is made for potassium carbonate. The Zeolite model uses the Linear Driving Force as a lumped parameter for modelling the sorption process. However, the chemical reaction of potassium carbonate and water can not be modelled using the LDF model. Modelling of water loading in potassium carbonate is done using a conversion dependent model. It is described as:

$$\alpha(t) = \frac{m(t) - m_0}{m_\infty - m_0} \tag{5.8}$$

Where $\alpha(t)$ is the fractional conversion as a function of time $[-]$, $m(t)$ is the weight at time t [g], and m_0 and m_∞ are the starting and final weight respectively, both in [g]. During dehydration, m_∞ is the weight of fully saturated K_2CO_3 (1.26 kg). For hydration m_0 is the weight of the fully dry TCM (1.06 kg). Equation 5.8 allows for calculating the fractional conversion based on experimental data.

In order to implement the water absorption in the model, a numerical determination of $\alpha(t)$ is introduced by means of the Arrhenius method. This is a method of calculating the conversion rate using three different parameters: a temperature dependent term $k(T)$, a pressure dependent term $h(p)$ and a shape function term $f(\alpha)$ (this depends on the value of conversion at that moment). Hydration rate according to the Arrhenius-$f(\alpha)$ method is given by [61]:

$$\frac{d\alpha}{dt} = k(T)f(\alpha)h(p) \tag{5.9}$$

Where $k(T)$ is the temperature dependence, which is described as [62].

$$k(T) = A_f exp\left(\frac{-E_a}{RT}\right) \tag{5.10}$$

Where A_f is the pre-exponential factor [1/min], E_a is the activation energy [J/mol]. T is the temperature [K] and R is the universal gas constant.

$f(\alpha)$ is the shape function, and is taken as [63]:

$$f(\alpha) = (1 - \alpha)^{2/3} \tag{5.11}$$

Lastly, the pressure dependency is described as follows:

$$h(p) = 1 - \frac{p_{eq}}{p_v} \tag{5.12}$$

Where p_v is the water vapor pressure and p_{eq} the equilibrium pressure, both in [Pa]. The equilibrium pressure is the pressure at which the hydration and dehydration would be in equilibrium. It is estimated using a fit of the Clausius-Clapeyron relation [64]:

$$p_{eq} = 4.288 \cdot 10^{12} exp\left(-\frac{7337}{T}\right) \tag{5.13}$$

Where T is the temperature of the potassium carbonate in K.

Combining these formulas gives the following formula for the conversion rate [63]:

$$\frac{d\alpha}{dt} = A_f exp\left(\frac{-E_a}{RT}\right)(1-\alpha)^{2/3}\left(1-\frac{p_{eq}}{p_v}\right) \tag{5.14}$$

The unknowns in this formula are the values for E_a and A_f. They were determined using experiments [62]. All values for modelling of the conversion rate are shown in Table 5.2.

Table 5.2: Parameters used for modelling of the conversion rate.

Parameter	Description	Value
E_a	Activation energy	3.600E4 [J/mol]
ΔH	Enthalpy of hydration	65.8 [kJ/mol]
A_f	Pre-exponential factor	2.929E5 [1/min]
D_s	Thermal diffusivity of K_2CO_3	0.37 [mm^2/s]
k_s	Thermal conductivity of K_2CO_3	0.55 [W/(m· K)]

Thermal conductivity and thermal diffusivity have been determined by Bird et al. (2020) [65].

Coupling of fractional conversion to water loading

Using Equation 5.14, the fractional conversion of each node can be calculated in COMSOL. In the concentration balance for continuum modeling (Equation 3.9) the loading gradient $\frac{dq}{dt}$ is used [mol/(kg· s)]. These two terms are coupled by using the molar mass of dry potassium carbonate and the density at every timestep:

$$\frac{dq}{dt} = \frac{n}{M_s} \cdot \frac{d\alpha}{dt} \tag{5.15}$$

Where n is the molar amount of water at the highest hydrate (1.5 mol), and M_s is the molar mass of dry potassium carbonate (0.1382 kg/mol). Using the same fraction with the conversion state α, the loading q is determined.

Initial and boundary conditions for K_2CO_3

The continuum model that is described in Chapter 3, is used for potassium carbonate as well. The kinetics are described using the fractional conversion model instead of the LDF model. In the previous section, the coupling from the Arrhenius model to water loading is made. The set of partial differential equations that describe the heat and mass transfer are the same as in the zeolite model. Heat transfer through the walls is modelled the same as well. The following boundary conditions are used:

$$t = 0 \longrightarrow T_b = T_w = T_{amb}, c = 0, \alpha = 0 \tag{5.16}$$

$$z = L \longrightarrow T_b = T_{in}, \frac{\partial T_w}{\partial z} = 0, c = c_{in}, \frac{\partial \alpha}{\partial z} = 0 \tag{5.17}$$

$$z = 0 \longrightarrow \frac{\partial T_b}{\partial z} = 0, \frac{\partial T_w}{\partial z} = 0, \frac{\partial c}{\partial z} = 0, \frac{\partial \alpha}{\partial z} = 0 \tag{5.18}$$

$$r = 0 \longrightarrow \frac{\partial T_b}{\partial r} = 0, \frac{\partial c}{\partial r} = 0, \frac{\partial \alpha}{\partial r} = 0 \tag{5.19}$$

$$r = r_1 \longrightarrow \frac{\partial c}{\partial r} = 0, \frac{\partial \alpha}{\partial r} = 0 \tag{5.20}$$

The locations of the boundary conditions are seen in Figure 3.3 The complete model is meshed using a maximum element size of 0.0016 m. This results in a mesh with a total of 20450 elements. A Figure of the mesh can be seen in the Figure below:

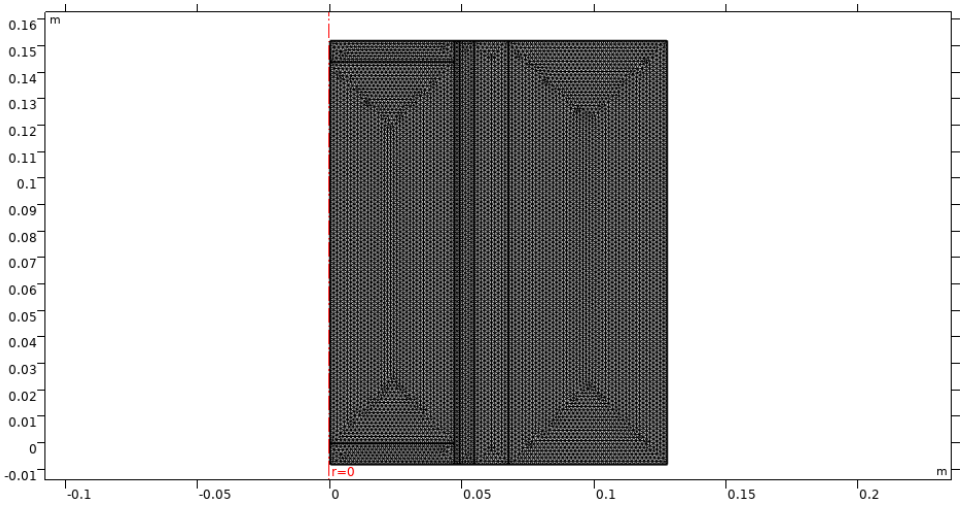

Figure 5.3: Snapshot taken from the COMSOL model of potassium carbonate. A maximum mesh size of 0.0016 m is used and the total number of elements is 20450.

5.3 Experiments

The material that is used in this research is potassium carbonate, over 99% pure, and produced by Boom [66]. A total of 10 kg is bought from this manufacturer. Sieves have been used to get a grain size between 1 and 1.4 mm. In total 1.06 kg of material is added into the reactor.

5.3.1 Cyclic experiments

According to literature the absorption rate of water is strongly dependent on a number of parameters: First and foremost, the adsorption rate depends on the ratio of the water vapor pressure over the equilibrium pressure (also known as driving force). Stanish (1984) found that the dehydration rate has an impact on the rehydration rate [67]. A low dehydration rate results in a low rehydration rate. Therefore the dehydration temperature is set to 180 °C for all experiments. Besides the dehydration rate, a large impact on the absorption rate is due to the amount of previous cycles [60, 67]. Each cycle causes the material to create more micro-pores, which allow for faster absorption. Therefore it is expected that after each cycle the absorption rate gets higher.

TGA experiments using the same material show a rapid increase in conversion state α based on the number of cycles performed [60, 67]. This can be seen in Figure 5.4.

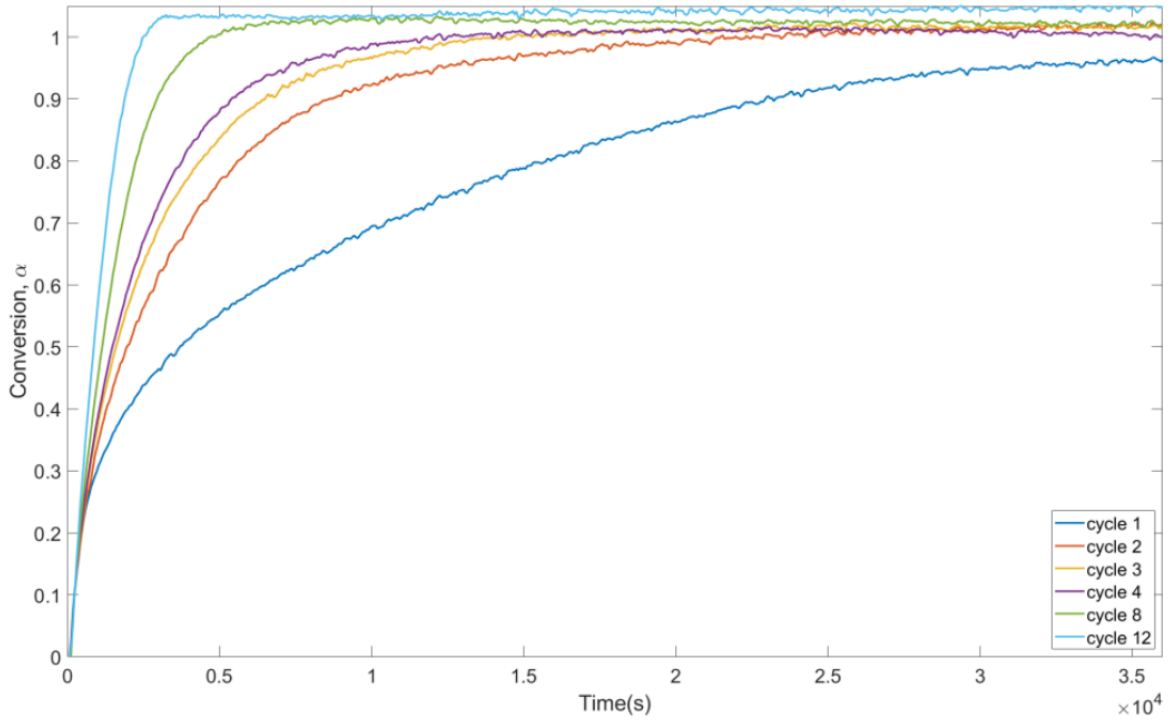

Figure 5.4: The fractional conversion of a 10 mg sample of K_2CO_3. Cyclic experiments in a climate chamber are conducted and the conversion rate is measured. For each subsequent cycle, the reaction speed increases [68].

Figure 5.4 shows the increase in reaction speed after each cycle. During these experiments, the material is placed inside a climate chamber and hydrated and dehydrated subsequently. The material did not touch any other material. A similar trend for the reaction speed is expected to be found after hydration/dehydration cycles with potassium carbonate inside the reactor. All cycle times are shown in Table 5.3.

The data in Table 5.3 can be read as follows. For the first experiment 1.06 kg of dry K_2CO_3 directly from the manufacturer is put in the reactor. The material is hydrated for 237 hours. After hydration the material is dehydrated for 24 hours. During this dehydration cycle no data was obtained due to technical issues. After dehydration the valves before and after the reactor are manually closed. The material is cooled down by natural convection for 24 hours. Temperature, RH, and weight are monitored during each experiment.

Before starting the next cycles, the dry and cooled K_2CO_3 from the previous cycle is removed from the reactor to counter agglomeration of the particles. It is noticed that the material agglomerates. However, the particles do not combine to larger particles, it is well possible to separate them. An example of agglomerated particles is seen in Figure H.3 in Appendix H. The particles are separated from each other as well as possible, before they are put back in the reactor. After filling the reactor the material is hydrated for the mentioned amount of hours, and then dehydrated for 24 hours. This process is repeated for every cycle mentioned in Table 5.3.

For all hydration experiments, Equation 5.8 is used to calculate the conversion rate. Here m_∞ is set to 207 g and m_0 is set to the experimental data at (t=1). The results for the conversion rate at the end of hydration experiments is shown in Table 5.4 It is observed that during cycle 1 the material absorption performance was very slow and after 237 hours only 13% of the maximum amount of water is absorbed. Due the low absorption rate, the RH sensors show similar values, and for longer experiments, calculating the mass using the RH sensors becomes less accurate.

Table 5.3: Hydration and dehydration times. All hydration is conducted at 25 °C at the inlet, using 25 g/h of water and 100 g/min of air, resulting in a water vapor pressure of approximately 12 mbar. Dehydration is conducted using an air flow of 100 g/min, the GFC set to 0 g/h and an inlet temperature of 120 °C.

Cycle number	Hydration time [h]	Dehydration time [h]	Comments
1	237	24	Dehydration data not available, 24 hours approximately
2	185	24	Material gets out of reactor relatively difficult. Agglomeration is seen.
3	103	24	Hydration stopped earlier than planned due to unknown closure of exit valve.
4	46	24	After dehydration, for one and a half hour, air of 40 °C is ran through the reactor to see if faster cooling is possible. Besides this cycle, natural convection is used for cooling down.
5	24	24	Material got out of reactor fairly well. Agglomeration is not observed as severely as the previous 4 cycles. Expected is that this is caused by the shorter hydration time, causing less water to absorb towards the center of the particles.
6	71	24	After cycle 5, the reaction speed of conversion got worse. Expected is that that is caused by the shorter hydration times. Therefore longer hydration is used in cycle 6 when comparing to cycle 5. Thermocouple 3 at the inside turned out to be bend during this cycle (see Appendix H).
7	240	48	Longer hydration due to limited access to the lab and the absorption performance not improving after cycle 4. Heavy agglomeration observed, see Figure H.3.
8	92	48	There is not RH2 data from this cycle.
9	125	-	52 gram less material inside reactor compared to cycle 8 due to expansion. Dehydration needs to be performed

Table 5.4: Conversion rate at the end of each hydration experiment. A conversion rate of 100% is equal to fully saturated material, while a conversion rate of 0% equals dry K_2CO_3.

Cycle number	Conversion rate using RH [%]	Conversion rate using Load cell [%]
1	0.63 %	13 %
2	23.7 %	29.6 % (note: Load cell not reliable due to bumping to setup)
3	33.3 %	20.9 %
4	32.6 %	25.6 %
5	25.2 %	18.6 %
6	37.8 %	29.9 %
7	63.4 %	50 %
8	Na	43.2 %

6 | Potassium carbonate results

In this chapter, the results of the potassium carbonate experiments are discussed. First, the results of the humidity control at the reactor inlet are shown. Next, the influence of cycling on the absorption rate is explained. Finally the performance of the material is compared to the performance of Zeolite 13X.

6.1 Humidity control

As mentioned in Chapter 5, controlling humidity at the inlet of the reactor is of great importance due to the risk of deliquescence. Besides preventing deliquescence, the water vapor pressure is the driving force of the chemical reaction. The inlet humidity is determined as the water vapor pressure by using 4.3. Data from cycle 2 (Figure 6.1) and cycle 3 (Figure 6.2) are plotted in the phase diagram as an example. The phase diagram is constructed by fitting p_{eq} (Equation 5.13) and the equilibrium humidity as describe in the work of Gaeini et al. (2019) [63].

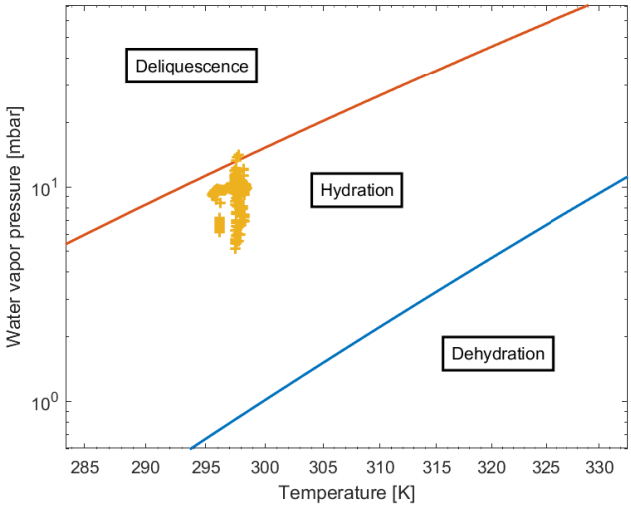

Figure 6.1: Data points of the complete hydration period plotted in the phase diagram for the second hydration cycle.

In Figure 6.1, the three different states are described. They are separated by equilibrium lines. The orange line represents the equilibrium between deliquescence and hydration of the material. The blue line represents the equilibrium conditions for the chemical reaction of water and potassium carbonate (Equation 5.1). Around 16 seconds of deliquescence are observed due to little fluctuations in the water flow controller. However, the reaction from sesquihydrate to deliquescence is a slow. After each cycle, dry particles are found.

Figure 6.2 shows the results of the third hydration cycle. Here it is observed that the inlet conditions are within the hydration area for the entire duration of the experiment. A similar spread is seen as in Figure

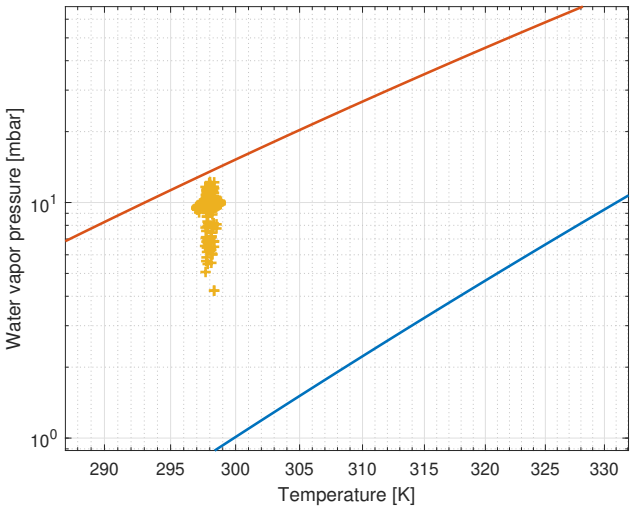

Figure 6.2: Reactor inlet conditions during the third hydration cycle.

6.1. This spread is likely caused by small differences in humidity. Thee gap between deliquescence and hydration is enough to prevent deliquescence from occurring. Data from all other experiments is seen in Appendix I

In conclusion, the humidity at the inlet is controlled. There is a small deviation in water vapor pressure observed. This deviation does not cause deliquescence to occur for extended period of time.

6.2 Experiments of K_2CO_3

In this section, the experimental results are discussed. First the experimental results of the absorped weight are shown. Then they are compared to the measured desorped weight. Next, the temperature over time is shown for each cycle. Then for each hydration cycle the stored energy is calculated and compared.

6.2.1 Experimental results

Hydration

As mentioned in section 5.3, the performance of the material in terms of absorption rate should become better over time. One of the first parameters to look into is the amount of absorbed water. For all the experiments, the absorped weight corresponding to a conversion rate α of 1 is 207 g. Expected is that water absorption over time follows a trend that is similar to the trend in Figure 5.4. At first, the results are created using the RH sensors, shown in Figure 6.3. For both sensors, the water vapor pressure is calculated using RH and temperature data following Equation 2.13. Then the mixing ratio is calculated using Equation 2.16. The mixing ratio is multiplied by the measured GFC values to get a water flow.

$$p_v = RH \cdot p_{sat}(T) \longrightarrow \zeta = \frac{p_v \frac{M_v}{M_a}}{p_{tot} - p_v} \longrightarrow \dot{m}_w = \dot{m}_a \cdot \zeta \tag{6.1}$$

By integrating the water flow over time, a total amount of absorbed water is determined. The results are shown in Figure 6.3.

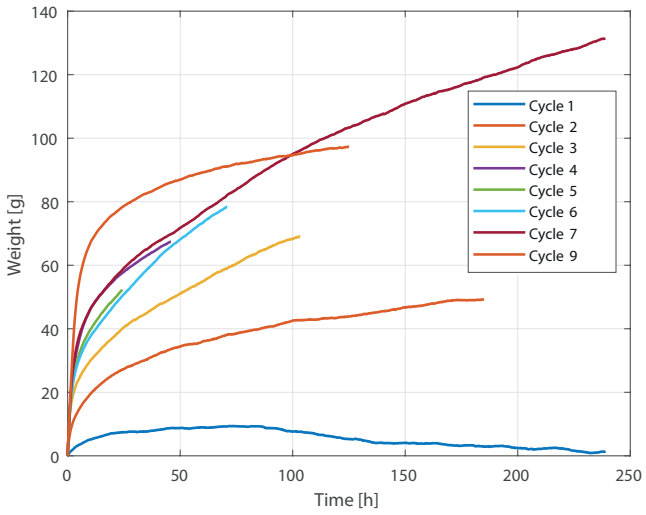

Figure 6.3: Amount of absorbed water during hydration measured using the RH sensors. Due to a technical failure of the RH sensors, no results were obtained fro cycle 8.

During cycle 8, the RH sensors were defect, therefore this cycle is not shown in Figure 6.3.The first thing that stands out in Figure 6.3 is that according to the relative humidity sensors, the first cycle stopped absorbing water after 75 hours of hydration and started desorping water. The result of cycle 1 shows a shortcoming of using RH sensors. When the adsorption rate is very low, the RH values at the inlet and outlet almost become equal, and errors determine if the trend is up or down . As the results created using RH sensors use integration, the error at the end of experiments is larger than at the beginning. Longer experiments have a larger error on the last value than shorter experiments.

During cycle one until four, the absorption rate gets higher every next cycle. However, for cycle four to seven, the conversion rate is equal or worse than the previous cycle. Expected is that it is caused by the fact that the cycles were becoming short compared to the first, second and seventh cycle, see Table 5.3.

Absorption of each cycle starts of fast. Here the limiting step of conversion is likely the rate of the chemical reaction. For each cycle, the absorption rate goes down. It is likely caused by the fact that the surface area of the material has reacted, and then diffusion through the material becomes the limiting step. Since the individual particles have likely a low porosity, water vapor cannot diffuse in the material easily. During each cycle, the material likely expands and shrinks, forming cracks to form in the process [60]. This creates a greater surface area of the particles with air, which in term causes the early absorption to go faster.

Data from the load cell is also used to investigate the influence of the amount of cycles on the absorption rate. The results are shown in Figure 6.4. Figure 6.4 shows the load cell data for each experiment. When

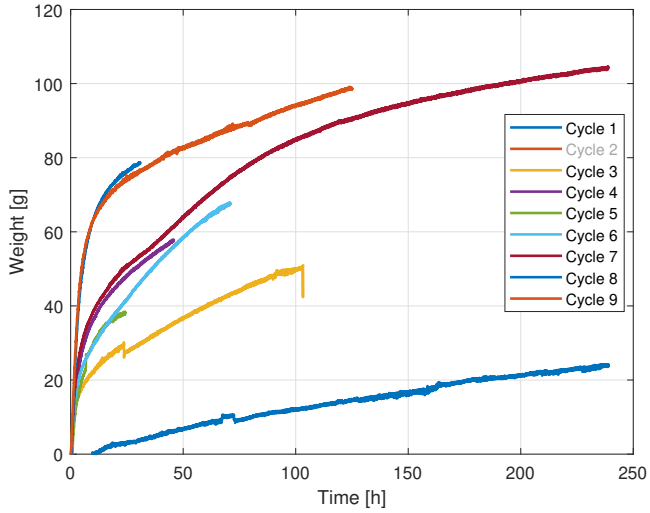

Figure 6.4: Amount of absorbed water during hydration measured using the load cell.

comparing Figure 6.4 to Figure 6.3, a difference is seen for cycle 1. As expected, after 75 hours the material is still absorbing water during cycle 1.

Furthermore, between Figure 6.3 and 6.4, similar patterns are observed for cycles 2 to 8. However, large deviations between the load cell data and RH sensors are seen near the end of the experiments, see Table 5.4. Again, this is likely caused by the error getting larger over time when using cumulative values (as done for the RH conversion to water absorption). Figure 6.4 shows some real steep increases for cycle 3. These are caused by environmental influences like bumps . Cycle 2 is not shown because the insulation fell of the reactor, causing inaccuracy in the load cell data . It is recommended to use the data from the load cell for calculating the conversion rate for experiments that take longer than 24 hours.

As can be seen in Figure 6.4, the long hydration period of cycle 7 causes the absorption performance to show large improvement from cycle 7 to 8. From cycle 1 to 8, the material is expanded in such a way that the height of the packed bed is raised from 117 mm to 134 mm (**see Figure 6.5**). Expansion of the particles is observed after the material is taken out of the reactor and the reactor is filled again. This is done before hydration of a new cycle.

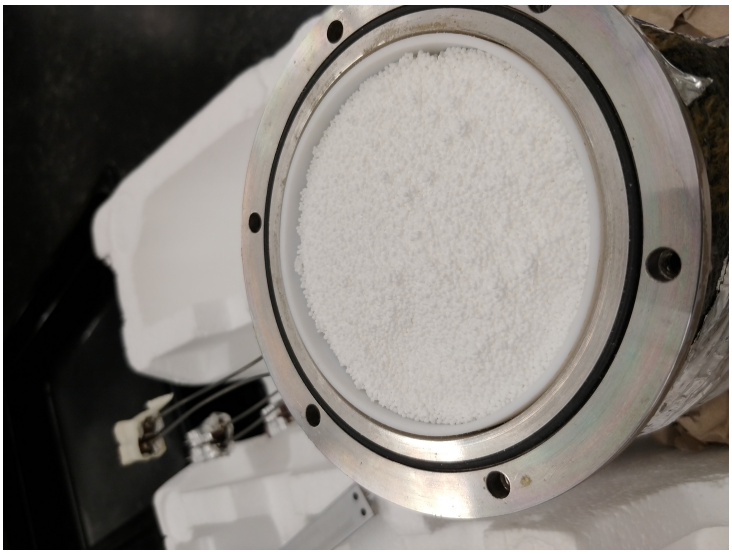

Figure 6.5: Height of the packed bed of potassium carbonate before cycle 8.

Dehydration

For dehydration of the cycles the amount of water is measured at the outlet as well. Using the methodology in Equation 6.1, the amount of desorbed water is visualized over time using the RH sensors. This is seen in Figure 6.6.

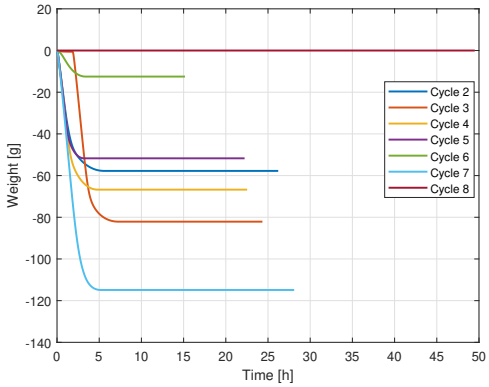

Figure 6.6: Amount of desorbed water during dehydration measured using the RH sensors.

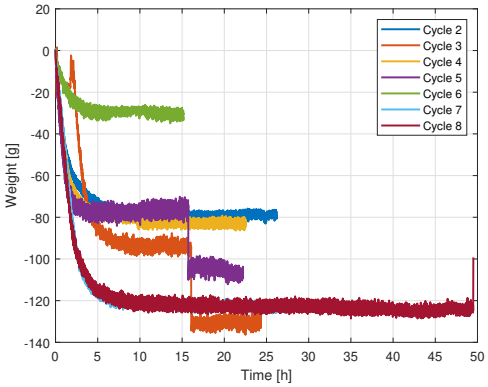

Figure 6.7: Amount of desorbed water during dehydration measured using the load cell.

All dehydration experiments are conducted with an air flow of 100 g/h and an inlet temperature of 120 °C. What can be seen in Figures 6.6 and 6.7 is that the time until total desorption is not dependent of the cycle. For example in Figure 6.6, the light blue line (cycle 7) had a hydration period which lead to a mass increase of 103.5 g. Despite the desorped mass being higher than for cycle 3, which had an absorbed water content of 41 g, it reaches full desorption earlier. The weight difference that is measured at full desorption are shown for the load cell and RH sensors in Table 6.1.

The end results are not very consistent. There is again some interference from environmental influences in the load cell data (for cycle 3 and 5). The conclusion can be drawn that total dehydration is reached after 10 hours or less.

Table 6.1: Measured desorption weight at the end of dehydration experiments using the RH-sensors or the load cell (LC). Due to technical problems the desorpted weight cold not be detected by the RH-sensors for cycles 6 and 8

Cycle number	Desorped weight RH [g]	Desorped weight LC [g]
2	58	78
3	82	131
4	67	84
5	52	109
6	-	-
7	115	125
8	-	125

6.2.2 Temperature increase

The second parameter that is interesting to measure during hydration is the temperature increase. During water absorption, energy is released, and this energy is measured in the form of temperature increase using the thermocouples inside the reactor (see Figure 2.7). The temperature increase between inlet and outlet is compared and plotted for each cycle. This means the thermocouple at the outlet is subtracted from the data of the thermocouple at the inlet, see T_{in} and T_{out} in Figure 2.7.

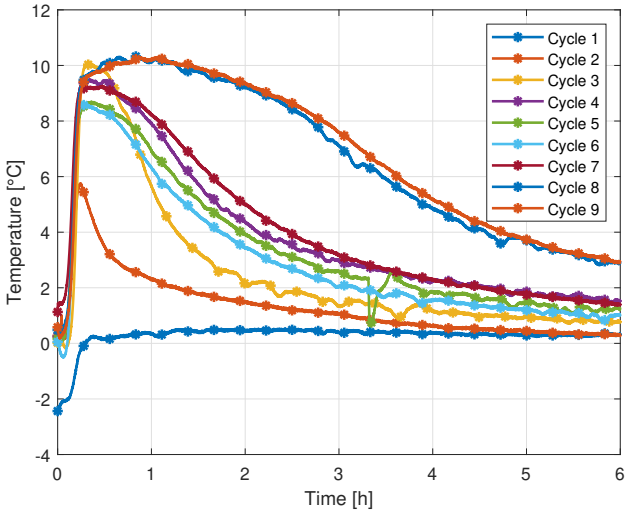

Figure 6.8: Temperature increase in the reactor during hydration for each cycle.

As seen in Figure 6.8, the material is able to release the heat faster after each cycle. From cycle four to six, the temperature increase is not getting better each cycle. This is likely due to the short hydration periods. This short hydration time does not allow water to diffuse to the nucleus of the particles. Therefore crack formation is likely not seen during these cycles.

Another observation that can be made, is that an increase in mass absorption rate, seen in Figures 6.3 and 6.4, correlates to a temperature increase that is prolonged for an extended period of time. In general, the temperature increase of each subsequent cycle is prolonged longer, and therefore the material performs better.

6.2.3 Storage capacity

The total amount of energy storage is determined for each cycle and plotted in Figure 6.9. The power that is produced by the packed bed is determined using Equation 2.23. The total energy storage is the sum of all outgoing power over time.

$$E_{K_2CO_3} = \int_0^{t_{end}} P dt \tag{6.2}$$

Where $E_{K_2CO_3}$ is the energy that is released during hydration as measured in the experiments. The theoretical value is calculated in Equation 5.6, and is equal to 157 Wh. The experimental results of the total energy are shown in Figure 6.9.

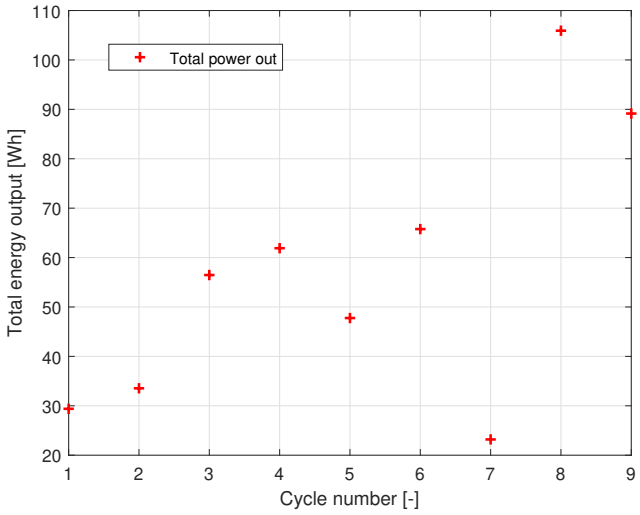

Figure 6.9: Total energy extracted during hydration as function of the number of hydration cycles.

Two notes should be made about Figure 6.9. Cycle 7 appears to be an outlier, which is caused by the fact that the ambient temperature was 5 °C lower than for all other experiments (17 °C versus 22 °C). For cycle 8, the RH sensors were not available for use, and therefore the mass outflow is calculated using the load cell data. The temperature profiles of cycle 8 and 9 were almost identical, and the power output for cycle 9 is similar. In general, an upward trend is seen when it comes to the total energy extracted for each subsequent cycle.

6.3 Numerical model of K_2CO_3

In this section the results of the numerical model are shown and compared to experiments based on the weight and temperature data. Lastly a parametric sweep is performed to see the influence of the pre-exponential factor on the weight and temperature profiles.

As mentioned in the previous subsection, the last cycle has the best thermal performance. As shown in Figure 6.8, the temperature increase is the highest and is prolonged longer than any other cycle. As the model uses fitted data from TGA experiments that have been cycled 12 times to determine the pre-exponential factor A_f and the activation energy E_a, the latest experiment is used to compare the model to.

Comparisons between the measurements of $T1$, $T2$ and $T3$ are made to the numerically calculated values. The results are shown in Figure 6.10. As seen in Figure 6.10, the model predicts a longer

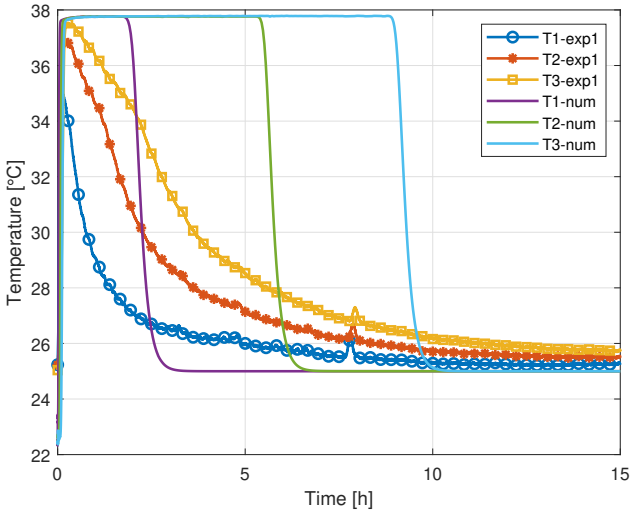

Figure 6.10: Thermocouples T1, T2 and T3 in the center of the packed bed. Comparison of the hydration of cycle 8 to the numerical model.

maximum temperature than the experimental data shows. This is likely due to the fact that the fitting values (A_f and E_a in Table 5.2) are found after 12 cycles in an experimental setup with only a couple of particles, that were not touching each other [62]. In a reactor, agglomeration is observed. Due to this agglomeration, the particles can not expand in the directions where they are in contact other particles. This causes the cracks that would otherwise form to be filled, which in turn slows the absorption process.

Outgoing mass flow of the model is compared to the weight measured using the load cell. These results are shown in Figure 6.11.

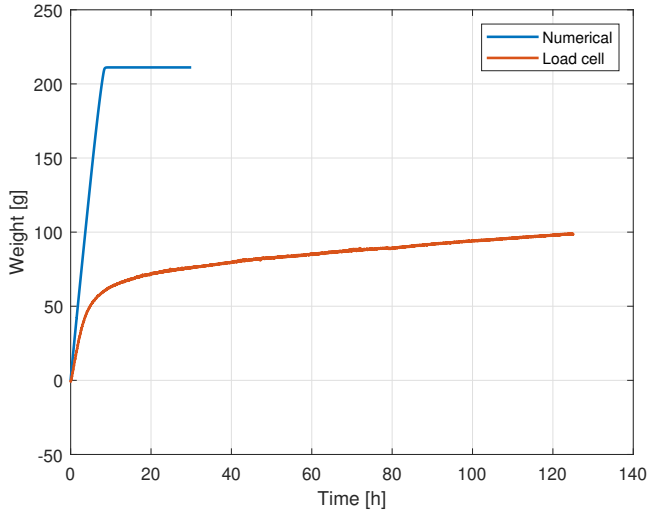

Figure 6.11: Amount of absorbed water measured using the load cell compared to the calculated amount using numerical model. Hydration experiment of cycle 8.

As seen in Figure 6.11, the absorption of water is estimated to happen way faster than that is happening in reality. This might be found in two reasons. The first cause might be that the reaction rate is not as fast as is modelled using the $\alpha(t)$ model. The second cause is likely caused by the packed bed type of reactor. The contact area between the particles and air is smaller per particle in a packed bed compared to TGA experiments.

The numerical model has a saturation weight of 211 g, compared to the 207 g expected. This result is close, however for a model an exact value of 207 g is expected. It might be caused by the particle density $\rho_{p,m}$ from Table 5.1. This value is correct for material with a porosity of 0. However, the potassium carbonate might have been slightly porous when bought. The particle density has not been experimentally measured, and might be slightly too high.

6.3.1 Parametric sweep pre-exponential factor

As the model does not describe cycle 8 properly, the fitting parameter A_f has been altered. This is done by means of a parametric sweep that uses the original value of A_f, 10%, 6% and 2% of the original value. The results are compared against experimental values from cycle 8. For the amount of absorbed water, the results of the parametric sweep are shown in Figure 6.12.

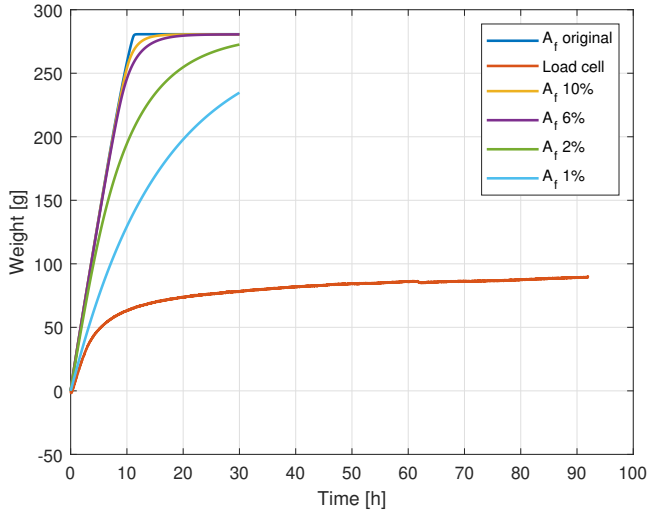

Figure 6.12: Results of the absorbed weight for parametric sweep of the pre-exponential factor. Swept for 100%, 10%, 6%, 2% and 1% of the original value. Compared to hydration load cell data of cycle 8.

A decrease in the pre-exponential factor causes a decrease in the absorption rate. However, for the used values it was not possible to get resemblance with the experiment. When comparing the absorption rate of $A_f 1\%$ to the experiment, it still models absorption too fast. However when looking at temperature plots a different trend is seen. Then, the temperature profile of $A_f 1\%$ does not reach the peak temperature that is seen in the experiment. This is seen in Figure 6.13.

Figure 6.13 shows the results of the numerical sweep when looking at the temperature. For the sake of readability only thermocouple T3 is shown in Figure 6.13. A decrease in the pre-exponential factor leads to a shift in shape of the figure. Physically a lower A_f means a lower rate of absorption. This causes the material to dehydrate over an extended period of time. At an A_f of 2% of the original value, a critical point is reached. Here the absorption reaction is modelled to be so slow that the heat release is not enough to reach the maximum of 38 °C.

The model represents the experimental data of measured using T3 the best using 2% of the original A_f value. An experimental sweep for the activation energy could not be ran due to convergence problems for any other value than the original.

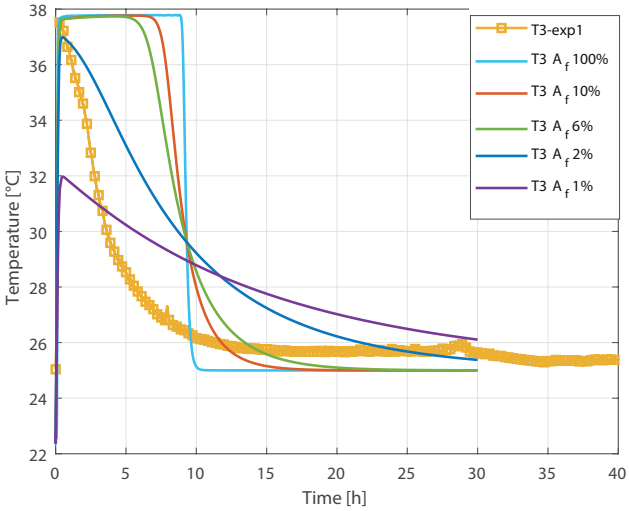

Figure 6.13: Results of the temperature at T3 for parametrics sweep of the pre-exponential factor. Swept for 100%, 10%, 6%, 2% and 1% of the original value. Compared to hydration of cycle 8.

6.4 Comparison to Zeolite 13X

An important part of the reactor setup is to be able to fairly compare different TCMs. As the system is the same for both tested TCMs so far, a comparison can be made. The hydration of K_2CO_3, cycle 9 is compared to Zeolite experiment 6 from Table 2.7, as the conditions of water and air flow are set to the same values. The resulting output power is compared and shown in Figure 6.14.

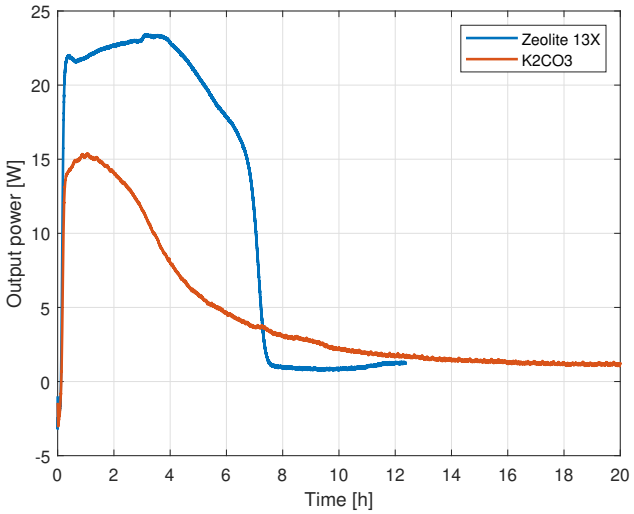

Figure 6.14: Comparison of output power using Eq. (2.23) between Zeolite 13X and potassium carbonate.

It is observed from Figure 6.14 that the the maximum power output of Zeolite 13X is higher than the maximum output power of K_2CO_3. After 7 hours the output power of potassium carbonate becomes slightly higher, however the output power is very minimal (3 to 2 W). The power drops to 1 W after 20 hours, and is therefore not taken into account. The energy extracted in 20 hours is 89 Wh for K_2CO_3 and 150 Wh for Zeolite 13X (area under the graph in Figure 6.14. Following the trend in Figure 6.9, it is expected that for K_2CO_3, the total energy stored is going to get higher after more cycles.

As Zeolite uses an adsorption process, K_2CO_3 works via a chemical reaction, and therefore absorption. It is interesting to see if the absorption process is slower than the adsorption process. This is compared using the temperature increase over the reactor (T_{out} compared to T_{in}, Figure 2.7). This is shown in Figure 6.15.

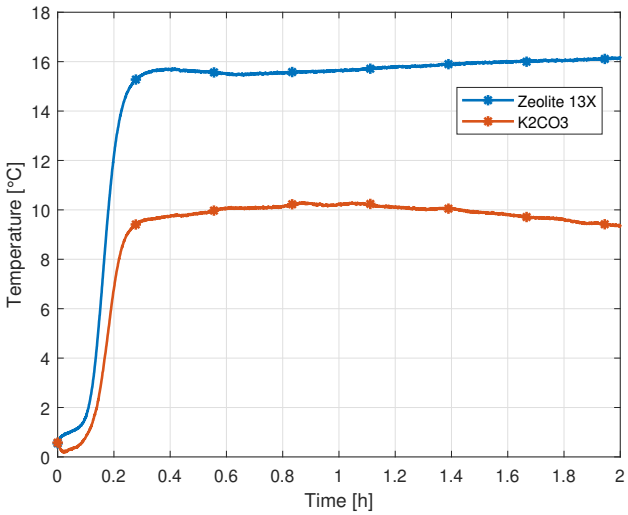

Figure 6.15: Thermal response of potassium carbonate cycle 9 compared to Zeolite 13X.

As seen in Figure 6.15, the thermal response of potassium carbonate is similar to Zeolite 13X, even though the processes are different (absorption for potassium carbonate and adsorption for Zeolite 13X). To make a comparison, the time it takes to reach a temperature increase of 8 °C, the reactor filled with Zeolite takes 10 min, while it takes the reactor filled with K_2CO_3 13 min. This is remarkable as one can argue that absorption processes take longer. The maximum temperature increase of Zeolite adsorption lies around 16 °C while the maximum temperature increase of K_2CO_3 is 10 °C.

The difference in weight of the reactor during hydration is also compared for Zeolite and K_2CO_3.. This is shown in Figure 6.16.

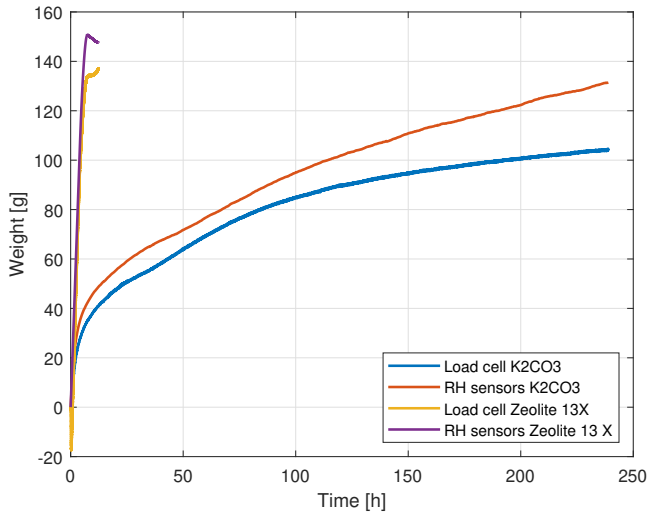

Figure 6.16: Measurements of the weight increase of the reactor by using both the load cell and the RH sensors for experiments with potassium carbonate as well as Zeolite 13X.

As expected, the adsorption process of Zeolite 13X is much faster than the absorption process of K_2CO_3. The total amount of water that Zeolite can adsorp is less than the potassium carbonate can. However, this is not yet seen in experiments.

In conclusion, the influence of subsequent cycling on K_2CO_3 is shown in this Chapter. If one wants to see an improvement in every cycle, it is advised to hydrate the material to a higher maximum weight than the cycle before. After 9 cycles, the performance in water absorption and temperature release are not on par with Zeolite. Theoretically, the performance should become similar, as they both have a similar energy storage capacity (158.4 Wh for Zeolite vs 157 Wh for K_2CO_3.)

7 | Conclusion and recommendations

The goal of this research was to get insight in the performance of Zeolite 13X and K_2CO_3 on reactor scale. The idea behind the used reactor system is that multiple TCMs can be investigated, using one single reactor system. This allows for fair comparison between materials and their performance.

7.1 Zeolite

First, a set of different inlet conditions is tested using Zeolite 13XBF with an average particle size of 3 mm (spread between 2.5 and 3.5 mm) as TCM. This material showed to be very stable, and therefore proved to be a good testing material. The assumption that the carrier gas contains no water is found to be incorrect. A water content of 0.0004 [kg water/kg air] in the carrier gas flow is found, and by taking this value into account, the humidity can be determined at the reactor inlet.

Influence air flow rate

Experiments are conducted to show the influence of air flow on the hydration time and maximum temperature for the hydration process of Zeolite 13X. When looking at the influence of flow speed (the total air flow), the conclusion can be drawn that the Zeolite is discharged in a faster manner with increasing flow speed. Also, the outlet temperature increases towards its maximum faster when the flow rate is higher (thermal response). The maximum temperature increase over the reactor is found to be 15 °C for the used set of conditions. A clear correlation between the maximum temperature output and flow speed is not found. The smallest tested flowspeed of 31 g/min did not reach the same temperature as the experiments that used flowspeeds of 53, 75 and 97 g/min. The exact reason behind this is not found. It might be caused by the long time the experiment of 31 g/min needed to reach full discharge compared to 53,75 and 97 g/min. This means there is a longer time period that heat is lost to ambient.

Influence of humidity

The experiments that are conducted show that the influence of humidity on the thermal response is minimal. However, a correlation between humidity and maximum temperature output is seen. An increase in water content relates to a higher temperature increase in the reactor.

A model in COMSOL is made that is validated using experiments. Using this model, theoretical situations are tested, of which the most prominent is the increase in temperature. This model showed that an increase in inlet temperature converts into a slightly lower temperature jump in the reactor. This is likely caused by the fact that a higher inlet temperature directly correlates to a higher temperature difference between the wall and ambient, and therefore more energy leaks away. Also, a higher inlet temperature causes the total time of discharge to go down, because the maximum loading goes down when the temperature goes up (following from Langmuir-Freundlich adsorption equilibrium, Eq. 2.18).

Ideal conditions

Depending on the scenario, different ideal working conditions can be proposed. If the goal is to reach a high temperature, it is best to use a high inlet humidity. If the goal is maximum power output, the humidity has to be as high as possible, as well as the air flow. Given the used reactor setup, an experiment has been conducted with an air flow of 100 g/min (maximum air flow of the given setup, using a water flow of 25 g/h (maximum water flow that did not reach condensation state).

No clear correlation between inlet conditions and total extracted power (efficiency) is found. The results show a spread that is likely caused due to uncertainties of the begin water loading. Further investigation is needed to find out if there is a correlation between the efficiency and inlet conditions.

7.2 Potassium carbonate

Pure potassium carbonate beads with a size of 1-1.4 mm have been used to test as TCM. The material is likely to show an increased performance when it comes to the rate of conversion when the number of charge and discharge cycles is increased [60]. In this research, a similar result is clearly seen in cycles 1 to 4. However, cycle 5, 6 and 7 show barely any improvement when it comes to conversion rate, likely caused by the duration of hydration being to short. When more water is absorbed than in the previous cycle, the temperature increase is prolonged over a longer time.

During the first experiment, the reactor was filled with potassium carbonate until the height of the first thermocouple (T1), which is 117 mm. After every dehydration experiment the material is investigated. Material expansion is not seen after opening up the reactor. However, the material does expand, it shows when material is taken out of the reactor and put back in. After 8 cycles, the material has expanded above the reactor height of 144 mm. For cycle 9, 52 g of material is not put back in the reactor again.

The performance of potassium carbonate is is investigated by hydrating the material in the reactor and evaluating the outlet temperature. The inlet conditions are set to 25 °C and 38% RH as well as possible. This results in a maximum temperature increase of 38 °C.

Numerical model

A numerical model is created, where the fractional conversion from dry to sesquihydrate is modelled using the $\alpha(t)$ model. The fractional conversion rate is based on fitting parameters. Compared to the experiments, the maximum temperature reached in the reactor is 38 °C, the same as for experiments. However, in the model this temperature is held on the maximum for a longer period of time. Expected is that as more experimental cycles are conducted, the temperature and absorption profile come closer to the model.

A parametric sweep on the pre-exponential factor showed that a perfect fit of hydration temperatures and weight during cycle 9 are not found. The value that comes closest to reality at the moment is found by using a value that is 2% of the originally used pre-exponential factor.

Comparison Zeolite and K_2CO_3

The results of temperature increase, power output and weight increase are compared for Zeolite and K_2CO_3 experiments. Both experiments are compared using the GFC set to 100 g/min and the LFC set to 25 g/h. The maximum power output of Zeolite 13X is equal to 23.2 W, where the maximum output power of K_2CO_3 cycle 9 was 15.2W. The thermal response of K_2CO_3 is on par with the thermal response of Zeolite 13X. The time it takes to reach a temperature increase of 8 °C is 10 minutes for Zeolite 13X,

compared to 13 minutes for K_2CO_3. The energy extracted in 20 hours is 89 Wh for K_2CO_3 and 150 Wh for Zeolite 13X.

7.3 Recommendations

In future work it is recommended to place the thermocouples that are meant to determine the heat flux through the wall (the losses) on the outside of the insulation instead of placing them on the outside of the stainless steel. Due to the high thermal resistance of the insulation, the temperature difference between the thermocouples TI and TW was most of the time within 1 °C, which is within margin of error of the thermocouples. Therefore no notes have been made on the losses through the wall.

Another recommendation is to insulate the piping between the heater and the reactor. It was seen that the ambient temperature had a significant impact on the results. Lastly, a recommendation is made to replace the glass filters of porosity 2 with ones that have a larger porosity. These glass filters account for the largest part of the pressure drop that is measured, and therefore the velocity profile had to be estimated using other work, instead of being able to use the measured value.

As shown in other research, the material performance of potassium carbonate is likely to perform better after more cycles. Some of the conducted hydration experiments have been shortened due to external factors. Conducting several more experiments where the full sesquihydrate state can be reached for the entire packed bed would be ideal. It is interesting to see if expansion of the particles stops at a certain cycle.

A | Reactor schematics and pictures

A detailed schematic of the 1 liter reactor setup is given below:

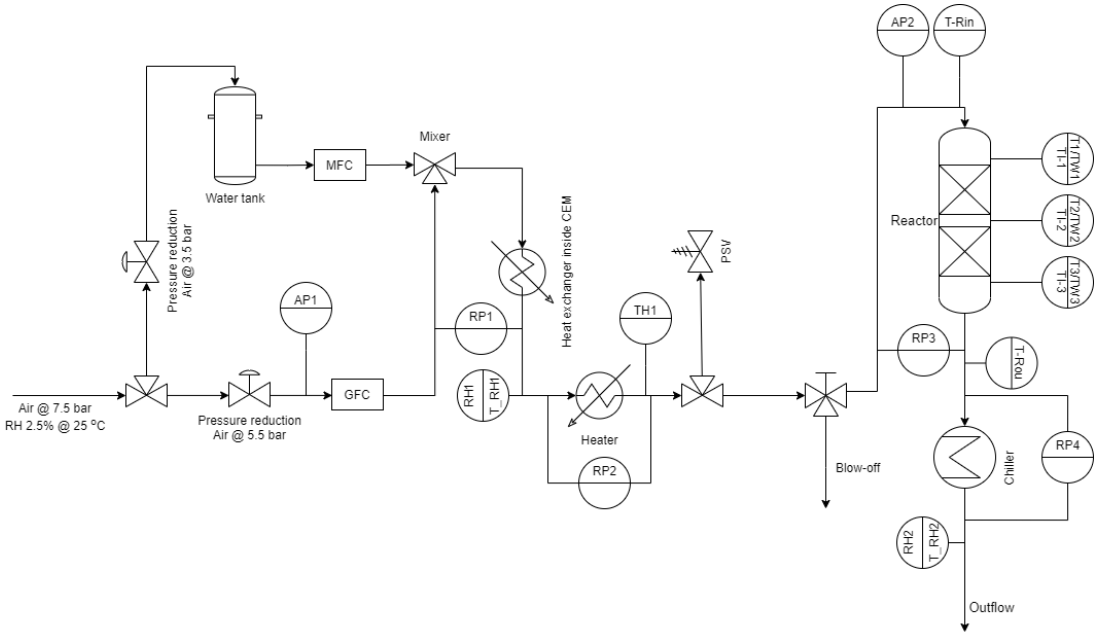

Figure A.1: Flowchart of the setup, including most sensors (at the reactor, 3 sensors are shown as one in the figure). Air coming in is going through two reduction valves. The air flow pressure is measured by an Absolute Pressure sensor (AP), before going through a Gas Flow Controller (GFC). Then it is being measured by a Relative Pressure sensor (RP). In the mixer, the air flow is mixed with a water flow that is controlled by the Mass Flow Controller (MFC). The flow after the mixer is measured on Relative Humidity (RH) and Temperature (T), and then goes through the reactor.

Air comes in at the inflow, and using a three-way valve split up in two different flows, one as air flow, and one as back pressure for a water tank. The pressure for the air flow always has to be higher than the back pressure of the water tank, otherwise, liquid could flow into the system. After running through a Gas Flow Controller, and water that runs through a Mass Flow Controller, both flows are recombined at the mixer, and then being heated up. Together, the mixer and first heater form the CEM. After the CEM, the flow goes through the heater, before going either through the blow-off or running through the reactor. The reactor contains a total of 11 thermocouples, one at the inlet, one at the outlet and at three different heights the reactor has thermocouples at the center (T-#), at the inside of the wall (TI-#) and at the outside of the wall (TW-#).

The reactor without insulation is seen in Figure A.2. After wrapping the reactor with exhaust wrap, it looks like seen in Figure A.3.

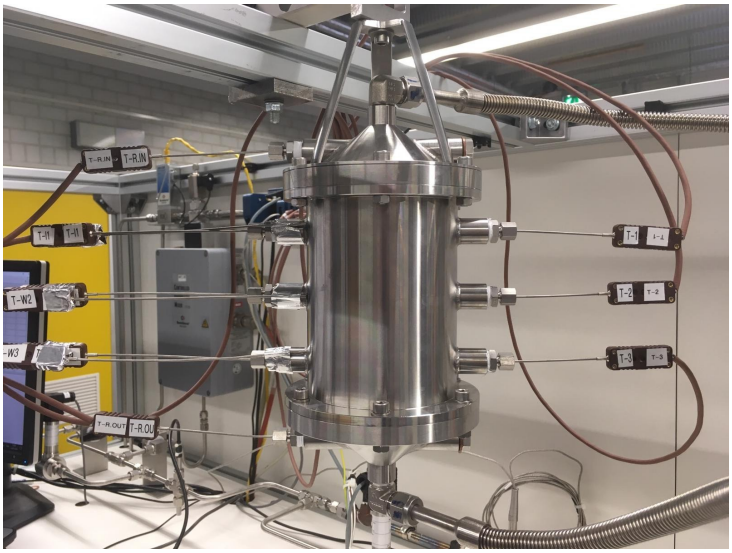

Figure A.2: The bare reactor, consisting of the teflon and steel layer

Figure A.3: Picture taken from the reactor after wrapping exhaust wrap around the steel layer. The exhaust wrap is held in place by means of metallic tape

B Temperature data to determine conductivity exhaust wrap

Here the temperature data from a steady state conduction experiment is shown.

Table B.1: Temperature values measured at steady state during dehydration with heater temperature set at 180 °C.

Temperature sensor	Meaured value
$TI1$	110 °C
$TI2$	108.3 °C
$TI3$	105.6 °C
$TW1$	107.6 °C
$TW2$	105.4 °C
$TW3$	102.8 °C
$Tamb$	28.0 °C
$Textra$	35.3 °C

Where $Textra$ is a thermocouple that is placed just inside the insulation at a height of 72 mm (height of $T2$). The location of this thermocouple is seen in Figure B.1

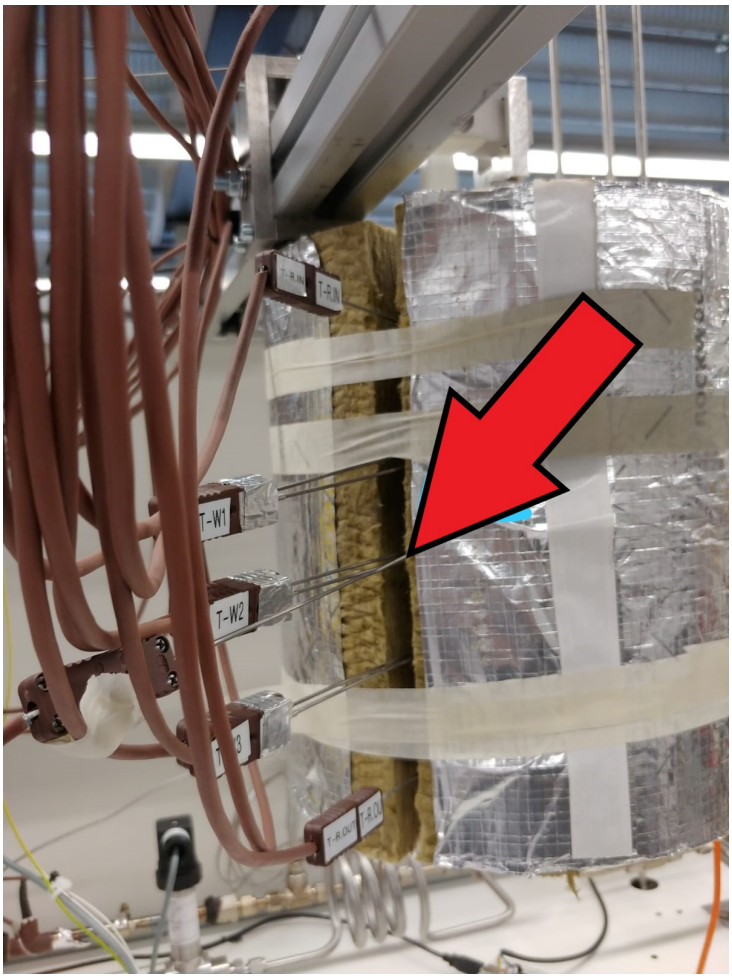

Figure B.1: Extra thermocouple placed at a height of 72 mm. Tip of the thermocouple is just inside the insulation layer.

C Temperature drop between heater and reactor inlet

The temperature losses in the tubing is determined experimentally for different settings of T_{heater}, which can be seen in the table below:

Table C.1: Steady state temperature drop between the heater ($TH3$) and the reactor inlet (Tin) with an ambient temperature of 25°C and an air inlfow of 100 g/min

Heater temperature [°C]	Temperature drop [°C]
40	4.6
60	11.2
80	18.2
100	25.4
120	33.3
140	41.9
160	50.4
180	58.9

D | Mixing ratio inlet vs outlet

In this Appendix, the mixingratio at the inlet(RH1) is compared to the outlet (RH2) for different hydration experiments using Zeolite 13X. After complete saturation of the material these mixing ratio's should become equal.

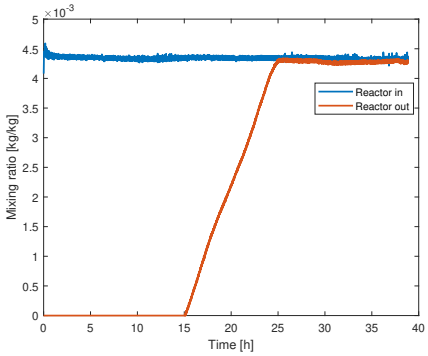

(a) Mixingratio in vs out for 31 gr/min air

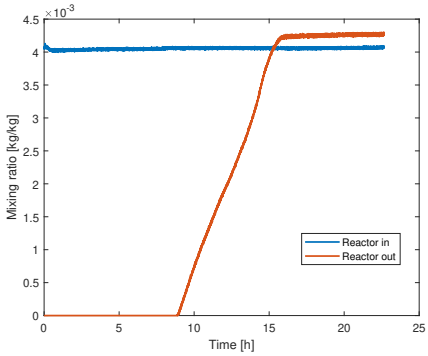

(b) Mixingratio in vs out for 53 gr/min air

Figure D.1a shows a result as expected, namely the mixing ratio at the outlet being equalt to inlet. However, for Figure D.1b, the measured mixing ratio at the outlet is higher than inlet. This is of course not possible, and likely caused by the way the pressure is calculated for the outlet. This is done by subtracting the relative pressure drop over the reactor $RP3$ and over the thermal bath $RP4$ from the absolute pressure measured at the reactor inlet $AP2$. Due to tubing in between the relative pressure sensors, this measured value is likely not very exact.

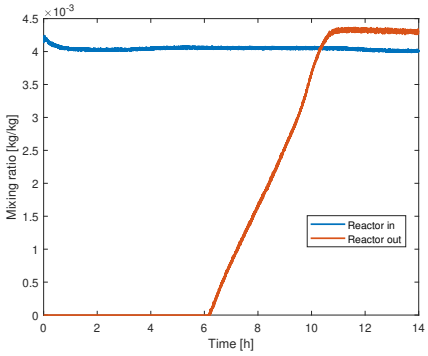

(a) Mixingratio in vs out for 75 gr/min air

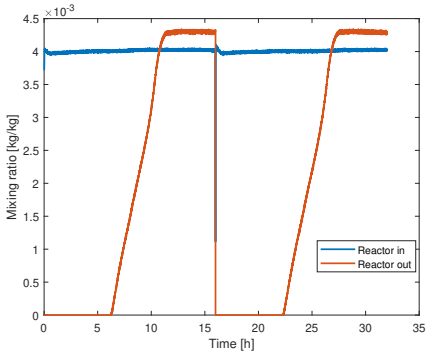

(b) Mixingratio in vs out for 75 gr/min air

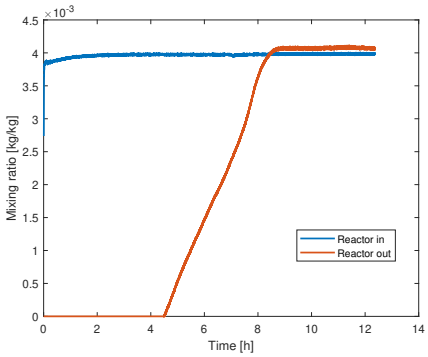

(a) Mixingratio in vs out for 97 gr/min air

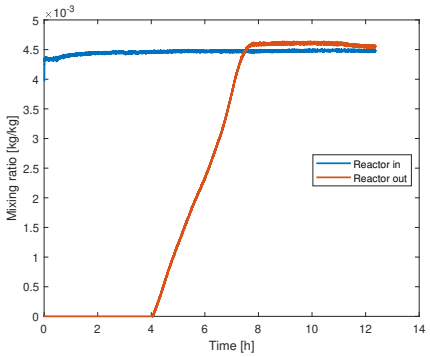

(b) Mixingratio in vs out for 97 gr/min air

E | Mesh convergence

Convergence of the mesh is determined by doing a simulation with a maximum mesh size of 0.0008 m, 0.0016 m and 0.0032 m. The results of size 0.0008 m are taken as baseline, and the other two simulations are compared against it by means of mean and maximum error for T2.

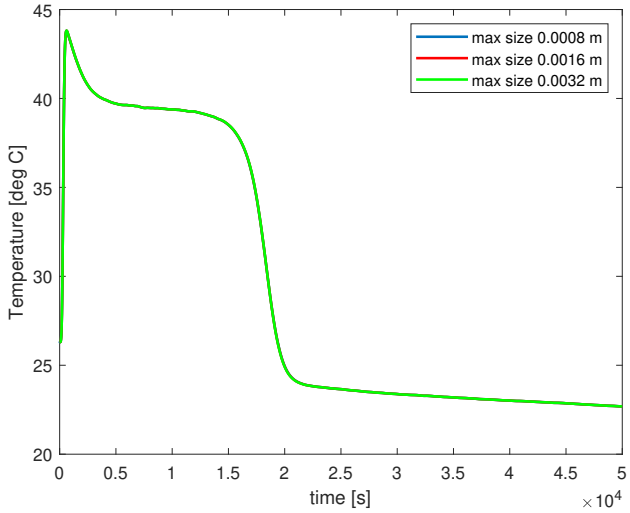

Figure E.1: Results of plots with a mesh size of max 0.0008 m, 0.0016 m and 0.0032 m

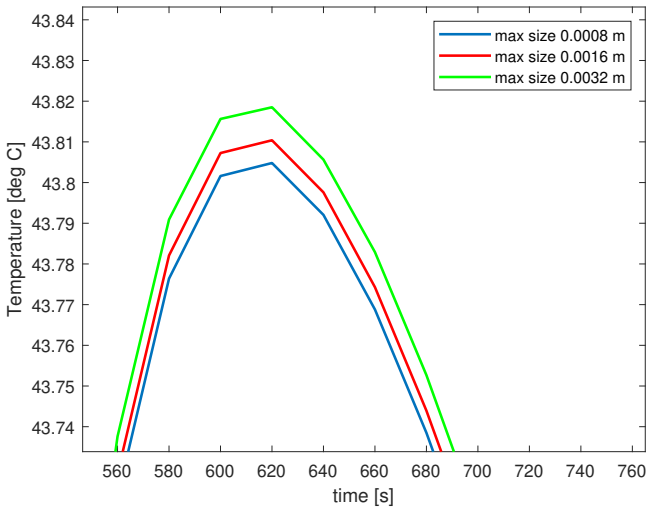

Figure E.2: Results of plots with a mesh size of max 0.0008 m, 0.0016 m and 0.0032 m at the peak temperature.

As shown in Figure E.1, the finest mesh and the coarsest mesh both follow the same trend. No fluctuations have been seen. In order to be sure, the point where fluctuations in modelling could have happened is shown in Figure E.2. The peak temperature in the beginning of the simulation could be sensitive to fluctuations, however the difference between the red line and blue line is 0.0238 °C and the difference between the green and blue line is 0.0405 °C. The computational time of 0.0008 m size mesh is 42 minutes, while the computational of 0.0016 m was only 11 minutes. Due to the small difference in results, the mesh size of 0.0016 m is used as it is the best balance between results and computational time.

F | Influence q_0

It is briefly mentioned in Chapter 4 that the initial loading before hydration can also be modelled using the COMSOL model. Here, the results of modelling hydration with the modelled initial loading are shown.

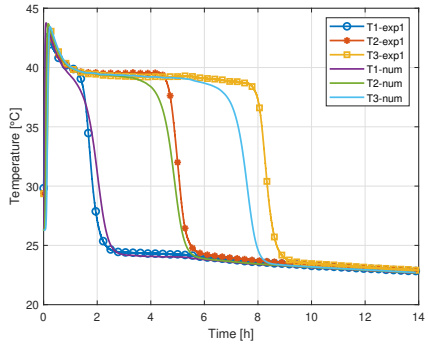

(a) Temperature profile using modelled q_0

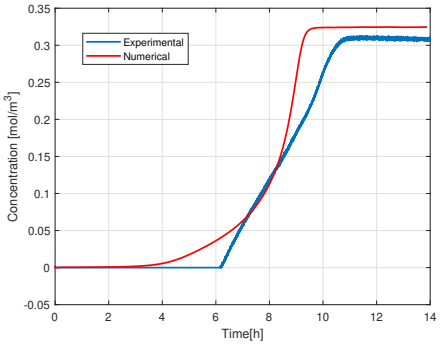

(b) Concentration at the outlet using modelled q_0

It is seen in Figures F.1a and F.1b that the modelled initial loading does not fit the hydration experiments. Therefore the method of using experiments to determine the water loading are used.

G | Natural convection coefficient

The natural convection coefficient is determined using the Grashof and Prandtl number. This is done for a dehydration experiment, as the temperature difference between the outside of the insulation and ambient is the largest. The parameters that are used are shown in Table G.1

Unit	Meaning	Value	Source
ΔT	Temperature difference between ambient and outside of insulation	7.3 K	measurement
T_f	Film temperature	304.8 K	measurement
g	Gravitational constant	9.81 m/s^2	-
ν	Kinematic viscosity of air	16.14E-6 m^2/s	[69]
L	Height of the reactor	0.144 m	measurement
D	Outside diameter of insulation	0.255 m	measurement
C_p @ T_f and 1 bar	Specific heat of air at film conditions	1006 J/(kg·K)	[69]
μ @ T_f	Dynamic viscosity of air at film conditions	18.68 E^{-6} Pa·s	[69]
k	Conductivity of insulation	0.036 W/(m·K)	[69]

Table G.1: Parameters used for calculation of natural convection coefficient

This gives a Grashof number of

$$Gr = \frac{9.81 \cdot 0.144^3 \cdot 7.3}{(16.14E^{-6})^2 \cdot 304.8} = 2.69E^6 \tag{G.1}$$

When using the assumption that natural convection of a cylinder can be determined as if it is a vertical plate the following condition must be met [29]:

$$\frac{D}{L} \geq \frac{35}{Gr^{1/4}} = \frac{0.255}{0.144} \geq \frac{35}{40.5} \tag{G.2}$$

Therefore, this statement holds. The Prandtl number is given as

$$Pr = \frac{\mu c_p}{k} = 0.522 \tag{G.3}$$

Using Welty [29], the function parameter lies between 0.505 (Pr = 0.072) and 0.567 (Pr = 1). Using linear interpolation, the function parameter is assumed to be 0.536.

This leaves the determination of the natural convection coefficient h_c to be:

$$h_c = \frac{4}{3}\frac{0.036}{0.144}0.536\frac{2.69E^{6\,1/4}}{4} = 5.12W/(m^2 \cdot K) \tag{G.4}$$

H | Expansion of potassium carbonate

Here two figures are shown of the height of the packed bed. Figure H.2 shows the height just before cycle 8. Figure H.2 shows the height before cycle 1. The difference in height is approximately 26 mm.

Figure H.1: Height of the particle bed before the first run

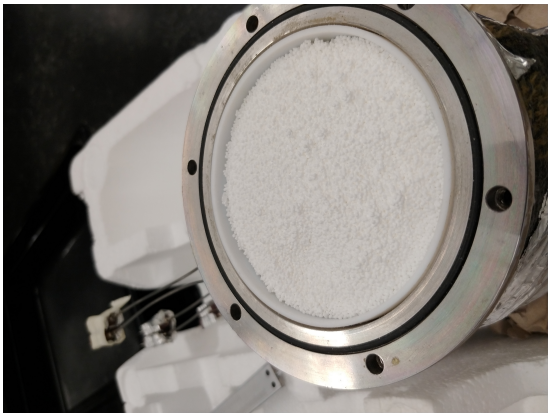

Figure H.2: Height of the packed bed of potassium carbonate before cycle 8

Figure H.3: Agglomeration of the particles in between two cycles.

I | Inlet conditions K_2CO_3

In this Appendix, the reactor inlet conditions (p,T) for hydration experiments 4 to 9 are shown inside the phase diagram.

Figures I.1,I.4, I.2, I.5, I.3 and I.6 show that the humidity control at the inlet of the reactor is accurate enough to prevent deliquescence.

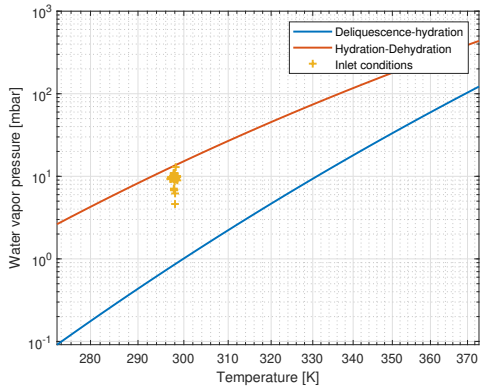

Figure I.1: Inlet conditions during hydration cycle 4.

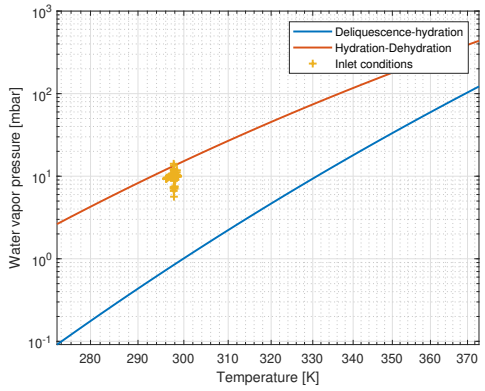

Figure I.2: Inlet conditions during hydration cycle 6.

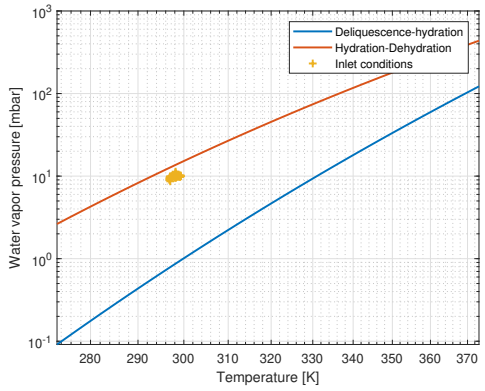

Figure I.3: Inlet conditions during hydration cycle 8.

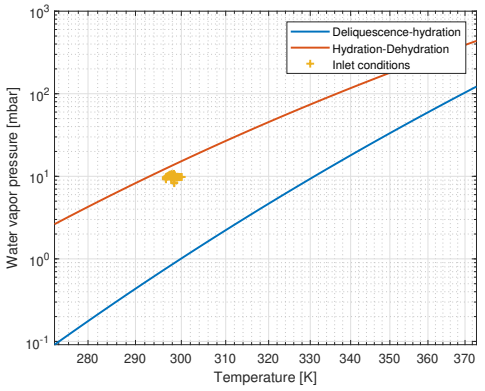

Figure I.4: Inlet conditions during hydration cycle 5.

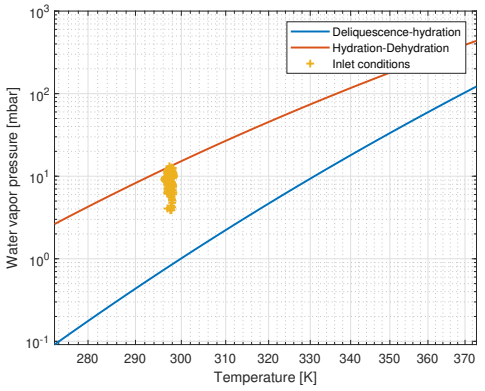

Figure I.5: Inlet conditions during hydration cycle 7

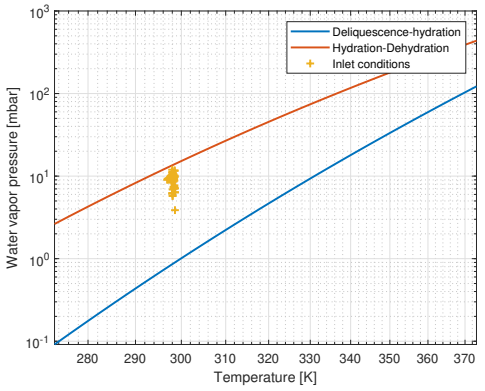

Figure I.6: Inlet conditions during hydration cycle 9

Bibliography

[1] NASA, "POWER Data Access Viewer." [Online]. Available: https://power.larc.nasa.gov/data-access-viewer/

[2] C. StatLine, "Aardgasbalans; aanbod en verbruik," 2020. [Online]. Available: https://opendata.cbs.nl/statline/{#}/CBS/nl/dataset/00372/table?ts=1583163013592

[3] Deloitte, "Zonnepanelen kunnen de helft van de Nederlandse elektriciteitsbehoefte opwekken," 2018. [Online]. Available: https://www2.deloitte.com/nl/nl/pages/data-analytics/articles/zonnepanelen.html

[4] "Should I use a solar PV or solar thermal system?" 2014. [Online]. Available: https://www.lightsourcebp.com/uk/2014/09/should-i-use-a-solar-pv-or-solar-thermal-system/

[5] N.V. Nederlandse Gasunie, "Physical properties of Natural gases," p. 255, 1980.

[6] European Environment Agency, "Final energy consumption by sector and fuel in Europe." [Online]. Available: https://www.eea.europa.eu/data-and-maps/indicators/final-energy-consumption-by-sector-10/assessment

[7] M. Boelhouwer, J. Gerdes, and S. Marbus, "Energietrends 2016," ECN, Tech. Rep., 2016.

[8] M. Ebrahimi and A. Keshavarz, "8 - CCHP Thermal Energy Storage," in *Combined Cooling, Heating and Power*, M. Ebrahimi and A. Keshavarz, Eds. Boston: Elsevier, 2015, pp. 183–188. [Online]. Available: http://www.sciencedirect.com/science/article/pii/B9780080999852000081

[9] A. Sharma, V. V. Tyagi, C. R. Chen, and D. Buddhi, "Review on thermal energy storage with phase change materials and applications," *Renewable and Sustainable Energy Reviews*, vol. 13, no. 2, pp. 318–345, 2009.

[10] H. Kerskes, *Thermochemical Energy Storage*. Elsevier Inc., 2016. [Online]. Available: http://dx.doi.org/10.1016/B978-0-12-803440-8/00017-8

[11] L. Sögütoglu, P. Donkers, H. Fischer, H. Huinink, and O. Adan, "In-depth investigation of thermochemical performance in a heat battery: Cyclic analysis of k2co3, mgcl2 and na2s," *Applied Energy*, vol. 215, pp. 159–173, 4 2018.

[12] H. Abedin and M. A. Rosen, "A critical review of thermochemical energy storage systems," *The Open Renewable Energy Journal*, vol. 4, pp. 42–46, 2011.

[13] B. Michel, P. Neveu, and N. Mazet, "Comparison of closed and open thermochemical processes, for long-term thermal energy storage applications," *Energy*, 2014.

[14] A. H. Abedin and M. A. Rosen, "Closed and open thermochemical energy storage: Energy- and exergy-based comparisons," *Energy*, vol. 41, no. 1, pp. 83–92, 2012. [Online]. Available: http://dx.doi.org/10.1016/j.energy.2011.06.034

[15] N. Yu, R. Z. Wang, and L. W. Wang, "Sorption thermal storage for solar energy," *Progress in Energy and Combustion Science*, vol. 39, no. 5, pp. 489–514, 2013.

[16] F. Fischer, W. Lutz, J. C. Buhl, and E. Laevemann, "Insights into the hydrothermal stability of zeolite 13X," *Microporous and Mesoporous Materials*, vol. 262, no. April 2017, pp. 258–268, 2018. [Online]. Available: https://doi.org/10.1016/j.micromeso.2017.11.053

[17] M. Gaeini, H. A. Zondag, and C. C. Rindt, "Effect of kinetics on the thermal performance of a sorption heat storage reactor," *Applied Thermal Engineering*, vol. 102, pp. 520–531, 2016. [Online]. Available: http://dx.doi.org/10.1016/j.applthermaleng.2016.03.055

[18] F. Kuznik, D. Gondre, K. Johannes, C. Obrecht, and D. David, "Numerical modelling and investigations on a full-scale zeolite 13X open heat storage for buildings," *Renewable Energy*, vol. 132, pp. 761–772, 2019.

[19] B. Mette, H. Kerskes, H. Drück, and H. Müller-Steinhagen, "Experimental and numerical investigations on the water vapor adsorption isotherms and kinetics of binderless zeolite 13X," *International Journal of Heat and Mass Transfer*, 2014.

[20] P. A. Donkers, L. C. Sögütoglu, H. P. Huinink, H. R. Fischer, and O. C. Adan, "A review of salt hydrates for seasonal heat storage in domestic applications," *Applied Energy*, vol. 199, pp. 45–68, 2017. [Online]. Available: http://dx.doi.org/10.1016/j.apenergy.2017.04.080

[21] J. . Buhl, M. Gerstmann, W. Lutz, and A. Ritzmann, "Hydrothermal stability of the novel zeolite type lsx in comparison to the traditional 13x modification," *Zeitschrift fur Anorganische und Allgemeine Chemie*, vol. 630, no. 4, pp. 604–608, 2004, cited By :22. [Online]. Available: www.scopus.com

[22] A. M. Norouzi, M. Siavashi, A. R. Soheili, and M. H. Khaliji Oskouei, "Experimental investigation of effects of grain size, inlet pressure and flow rate of air and argon on pressure drop through a packed bed of granular activated carbon," *International Communications in Heat and Mass Transfer*, 2018.

[23] Heraeus, *Porous Quartz Filter Discs*, 2018. [Online]. Available: https://www.heraeus.com/en/hca/products{_}hca/plates{_}quartz{_}1/filter{_}discs{_}1/filter{_}discs{_}hca.html

[24] Bronkhorst, *EL-FLOW Select*, 2020. [Online]. Available: https://www.bronkhorst.com/nl-nl/producten/gas-flow/el-flow-select/#p_lt_ctl08_pageplaceholder_p_lt_ctl01_FRDividerWebPart4_colDivision

[25] ——, *CEM: Liquid Delivery System with Vapour Control*, 2020. [Online]. Available: https://www.bronkhorst.com/nl-nl/producten/damp-flow/w-303b/

[26] Keller, "Piezoresistive Pressure Transmitters Series 23 / 25," 2020. [Online]. Available: http://www.keller-druck.com/picts/pdf/engl/23e.pdf

[27] REOTEMP, "Thermocouple Accuracies." [Online]. Available: https://www.thermocoupleinfo.com/thermocouple-accuracies.htm

[28] Sensirion, "Datasheet SHT85," 2018. [Online]. Available: https://www.sensirion.com/en/environmental-sensors/humidity-sensors/sht85-pin-type-humidity-sensor-enabling-easy-replaceability/

[29] J. R. Welty, C. E. Wicks, and R. E. Wilson, *Fundamentals of momentum, heat and mass transfer*. Wiley, 2015.

[30] D. Sonntag, "Important new values of the physical constants of 1986, vapour pressure formulations based on the ITS-90, and psychrometer formulae," in *Zeitschrift für Meteorologie*, 40th ed., 1990, pp. 340–344.

[31] B. S. Institution, *BS 1339-1: 2002*. BSI, 2008, no. January.

[32] B. P. Bering, M. M. Dubinin, and V. V. Serpinsky, "Theory of volume filling for vapor adsorption," *Journal of Colloid and Interface Science*, vol. 21, no. 4, pp. 378–393, 1966. [Online]. Available: http://www.sciencedirect.com/science/article/pii/0095852266900043

[33] M. Gaeini, "Thermochemical seasonal heat storage for the built environment," PhD Thesis, Eindhoven, 2017.

[34] D. D. Do, *Adsorption Analysis: Equilibria and Kinetics*. PUBLISHED BY IMPERIAL COLLEGE PRESS AND DISTRIBUTED BY WORLD SCIENTIFIC PUBLISHING CO., 1998. [Online]. Available: https://www.worldscientific.com/doi/abs/10.1142/p111

[35] M. Punčochář and J. Drahoš, "Limits of applicability of capillary model for pressure drop correlation," *Chemical Engineering Science*, vol. 55, no. 18, pp. 3951–3954, 2000.

[36] G. W. Johnson and R. S. Kapner, "The dependence of axial dispersion on non-uniform flows in beds of uniform packing," *Chemical Engineering Science*, vol. 45, no. 11, pp. 3329–3339, 1990.

[37] M. Giese, K. Rottschäfer, and D. Vortmeyer, "Measured and Modeled Superficial Flow Profiles in Packed Beds with Liquid Flow," *AIChE Journal*, vol. 44, no. 2, pp. 484–490, 1998.

[38] W. Kwapinski, K. Salem, D. Mewes, and E. Tsotsas, "Thermal and flow effects during adsorption in conventional, diluted and annular packed beds," *Chemical Engineering Science*, 2010.

[39] D. Vortmeyer and J. Schuster, "Evaluation of steady flow profiles in rectangular and circular packed beds by a variational method," *Chemical Engineering Science*, vol. 38, pp. 1691–1699, 1983.

[40] O. Bey and G. Eigenberger, "Fluid flow through catalyst filled tubes," *Chemical Engineering Science*, vol. 52, no. 8, pp. 1365–1376, 1997.

[41] G. Koning, "Heat and Mass Transport in Tubular Packed Bed Reactors at Reacting and Non-Reacting Conditions," *Measurement*, p. 272, 2002.

[42] H. Martin and M. Nilles, "Radiale Warmeleitung in durchstromten Schuttungsrohren," *Chemie Ingenieur Technik*, vol. 65, no. 12, pp. 1468–1477, 1993.

[43] P. Zehner and E. U. Schlünder, "Warmeleitfahigkeit von Schuttungen bei mässigen Temperaturen," *Chemie Ingenieur Technik*, vol. 42, pp. 933–941, 1970.

[44] M. Kandula, "On the effective thermal conductivity of porous packed beds with uniform spherical particles," *Journal of Porous Media*, vol. 14, pp. 919–926, 2011.

[45] M. Winterberg, E. Tsotsas, A. Krischke, and D. Vortmeyer, "A simple and coherent set of coefficients for modelling of heat and mass transport with and without chemical reaction in tubes filled with spheres," *Chemical Engineering Science*, vol. 55, no. 5, pp. 967–979, 2000.

[46] E. Tsotsas, *Wärmeleitung und Dispersion in durchströmten Schüttungen*. Berlin, Heidelberg: Springer Berlin Heidelberg, 1997.

[47] R. Aris and N. R. Amundson, "Some remarks on longitudinal mixing or diffusion in fixed beds," *AIChE Journal*, vol. 3, no. 2, pp. 280–282, 1957.

[48] S. Chapman and T. Cowling, *The mathematical theory of non-uniform gases: an account of the kinetic theory of viscosity, thermal conduction and diffusion in gases.* Cambridge university press, 1970.

[49] P. Cheng and D. Vortmeyer, "Transverse thermal dispersion and wall channelling in a packed bed with forced convective flow," *Chemical Engineering Science*, vol. 43, no. 9, pp. 2523–2532, 1988.

[50] S. Sircar and J. R. Hufton, "Why Does the Linear Driving Force Model for Adsorption Kinetics Work?" *Adsorption*, vol. 6, no. 2, pp. 137–147, 2000. [Online]. Available: https://doi.org/10.1023/A:1008965317983

[51] D. M. Ruthven, *Principles of adsorption and adsorption processes.* New York (USA): John Wiley and Sons, Inc., 1984.

[52] N. Wakao and T. Funazkri, "Effect of fluid dispersion coefficients on particle-to-fluid mass transfer coefficients in packed beds. Correlation of sherwood numbers," *Chemical Engineering Science*, vol. 33, no. 10, pp. 1375–1384, 1978.

[53] B. Crittenden and W. J. Thomas, *Adsorption technology and design*. Elsevier, 1998.

[54] J. Comiti and M. Renaud, "A new model for determining mean structure parameters of fixed beds from pressure drop measurements: application to beds packed with parallelepipedal particles," *Chemical Engineering Science*, vol. 44, no. 7, pp. 1539–1545, 1989.

[55] C. C. Rindt and S. V. Gaastra-Nedea, *Modeling thermochemical reactions in thermal energy storage systems*. Woodhead Publishing Limited, 2015. [Online]. Available: http://dx.doi.org/10.1533/9781782420965.3.375

[56] C. Barreneche, A. I. Fernández, L. F. Cabeza, and R. Cuypers, "Thermophysical characterization and thermal cycling stability of two TCM: CaCl2 and zeolite," *Applied Energy*, vol. 137, pp. 726–730, 2015. [Online]. Available: http://dx.doi.org/10.1016/j.apenergy.2014.09.025

[57] "Deliquescence." [Online]. Available: https://www.britannica.com/science/deliquescence

[58] C. Ferchaud, "Experimental study of salt hydrates for thermochemical seasonal heat storage," PhD Thesis, Technische Universiteit Eindhoven, 2016.

[59] Knovel. Knovel, 2020. [Online]. Available: https://app.knovel.com/hotlink/itble/id:kt00BKAOL1/table-20-density-solid/table-20-density-solid

[60] M. A. Beving, A. J. Frijns, C. C. Rindt, and D. M. Smeulders, "Effect of cycle-induced crack formation on the hydration behaviour of K2CO3 particles: Experiments and modelling," *Thermochimica Acta*, vol. 692, no. March, p. 178752, 2020. [Online]. Available: https://doi.org/10.1016/j.tca.2020.178752

[61] A. Fopah Lele, F. Kuznik, H. U. Rammelberg, T. Osterland, and W. Ruck, "Thermal decomposition kinetic of salt hydrates for heat storage systems," *Applied Energy*, vol. 154, pp. 447–458, 09 2015.

[62] W. van den Dobbelsteen, "A Developed DNS Model for Hydration of a K2CO3 Particle Bed," MSc Thesis, TU Eindhoven, 2020.

[63] M. Gaeini, S. A. Shaik, and C. C. Rindt, "Characterization of potassium carbonate salt hydrate for thermochemical energy storage in buildings," *Energy and Buildings*, vol. 196, pp. 178–193, 2019. [Online]. Available: https://doi.org/10.1016/j.enbuild.2019.05.029

[64] L. C. Sögütoglu, P. A. Donkers, H. R. Fischer, H. P. Huinink, and O. C. Adan, "In-depth investigation of thermochemical performance in a heat battery: Cyclic analysis of K2CO3, MgCl2 and Na2S," *Applied Energy*, vol. 215, no. February, pp. 159–173, 2018.

[65] J. E. Bird, T. D. Humphries, M. Paskevicius, L. Poupin, and C. E. Buckley, "Thermal properties of thermochemical heat storage materials," *Physical Chemistry Chemical Physics*, vol. 22, no. 8, pp. 4617–4625, 2020.

[66] "Kaliumcarbonaat, z.z. (76050932.9025)." [Online]. Available: https://www.boomlab.nl/product/76050932-9025+boom-kaliumcarbonaat-z-z-76050932-9025

[67] M. A. Stanish and D. D. Perlmutter, "Rate processes in cycling a reversible gas solid reaction," *AIChE Journal*, vol. 30, no. 1, pp. 56–62, 1984.

[68] M. A. J. M. Beving, A. J. H. Frijns, C. C. Rindt, and D. M. J. Smeulders, "Characterization and modelling of K2CO3 cycles for thermochemical energy storage applications," *Proceedings of Eurotherm Seminar 112*, no. 2019, pp. 1–10, 2019.

[69] "Engineering Toolbox - Air Thermophysical Properties ." [Online]. Available: https://www.engineeringtoolbox.com/air-properties-d_156.html